Doctoral thesis

Application of Optical Sound Measurement in Microphone Calibration Method

February 2021

Denny HERMAWANTO

Doctoral thesis

Application of Optical Sound Measurement in Microphone Calibration Method

February 2021

Waseda University

Graduate School of Fundamental Science and Engineering

Department of Intermedia Studies

Research on Communication Acoustics

Denny HERMAWANTO

Contents

List of Figures

List of Tables

Acknowledgements

First of all, I would like to express my sincere gratitude to Research and Innovation in Science and Technology Project (RISET-Pro) scholarship program, Kemenristek/BRIN, Indonesia, which provides financial support for my research.

I would like to express my sincere thanks to my supervisor, Professor Yasuhiro Oikawa. Without his advice and guidance, I would not have made it. He taught me a lot of things about research, ethics, and leadership. It is a great honor to be his student.

I am grateful to Professor Tetsuya Ogata and Professor Takashi Kawai, the referee of my thesis, for the insightful comments and encouragement to sharpen my research from various perspectives.

My sincere thanks also go to Dr. Kohei Yatabe and Dr. Ishikawa Kenji for their availability and patience to teach me the optical sound measurement method. Without their support, it would not be possible to conduct this research. I would also like to thank all Oikawa lab members for the great time I have had in Japan.

Finally, to my wife, Rika Agustin, my sons, Faizan and Akio, and my family: thank you for continuous support and patience along the way on this journey.

Chapter 1

Introduction

1.1 Calibration system

Measurement is the process of determining the value of a quantity. The measurement result is expressed as the measurement unit [1,2]. The International System of Quantities (ISQ) defines seven base quantities: length, mass, time, electric current, thermodynamic temperature, amount of substance, and luminous intensity. The base units for the corresponding quantities are meter (m), kilogram (kg), second (s), ampere (A), kelvin (K), mol (mol), candela (cd). These seven base units have been adopted as the International System of Units (SI) in the General Conference on Weights and Measures International System of Units (Conférence Générale des poids et mesures) [3, 4].

Calibration is an act of comparing the measurement result of a device under test (UUT) to the reference unit. Generally, the reference unit has higher accuracy and precision level than the UUT. The calibration is essential to ensure that every instrument or transducer for the same measurement unit produces a comparable result. In the global trade system, this equality is necessary to create fair trade. Another importance of the calibration is to determine the instrument's accuracy and reliability for the measurement [2].

In the calibration chain hierarchy, the country's National Metrology Institute (NMI) is positioned at the top level. The NMI provides the country's reference unit and is used by the secondary calibration labs to calibrate their reference unit. This calibration chain system creates a link between the end-user instrument's measurement result and the unit's definition in the SI.

The development of transducer is going vast, nowadays. More physical quantities can be sensed by the invention of a new type of transducer. The new type of transducer improves the current transducer capability, thus broaden its applicability. There are many new types of instruments available. Calibration is required to assure the correctness of these instruments measurement results. However, occasionally, the existing calibration methods can not be implemented directly for a new transducer type due to some differences in the specification or geometry. Therefore, sustainable development of the calibration method is required to balance the transducer technology.

1.2 Microphone calibration

1.2.1 Microphone

Sound occurs as a result of pressure variation in the medium. The physical quantity of the sound is the pressure with the measurement unit of Pascal (Pa). A microphone is a transducer that converts sound pressure into electrical voltage. A microphone's construction comprises a diaphragm and backplate separated by an air gap, forming a capacitive configuration. When exposed to a sound, the air pressure moves the diaphragm, changing the microphone's capacitance and producing an electrical voltage. The microphone's transduction property is represented by the microphone's sensitivity and has a measurement unit of millivolts per pascal (mV/Pa). The sensitivity and its frequency response are determined by the material and construction design of the microphone.

The sensitivity is an essential parameter of a microphone for the development of the instrument. An instrument used to capture the far-field sound, such as a smart-speaker, hearing aid, and noise-canceling headphones requires a high-sensitivity type of microphone to capture the sound from a distance. Meanwhile, a high-sensitivity microphone is not suitable for an instrument designed to capture sound from the near-field, such as telecommunication devices, because the signal will be clipped and distorted. The microphone sensitivity and its frequency response are determined by the material and construction design.

Conventional measurement microphone diaphragm has a general shape of circular. Common available size is 1 inch, 1/2 inch, 1/4, and 1/8 inch. For the standardization, the specification of the measurement microphone has been documented in the IEC standard. For example, IEC 61094-1 and IEC 61094-4 describe laboratory standard and working standard microphone, respectively.

1.2.2 Calibration methods

The microphone calibration methods are also documented in the IEC 61094 standards series. The most accurate is the reciprocity method. The realization of the reciprocity method in the pressure field and free field environment is explained in the IEC 61094-2 and IEC 61094-3. The process applies to a reciprocal type of microphone. In this method, the microphone's sensitivity is calculated from the electrical transfer function and acoustical transfer impedance calculation. A precise measurement of the microphone's acoustic center is required for the calculation of acoustical transfer impedance.

For the secondary method, the microphone comparison or substitution calibration method is available in the standard. This calibration procedure is explained in the IEC 61094-5 for pressure field calibration and IEC 61094-8 for calibration in the free field environment. The configuration and calibration procedure is more simple than the reciprocity method. A sound pressure applied to the reference microphone is used to determine the sensitivity of the UUT. The process assumes that both reference microphone and UUT experience the same sound field. This method is less precise than the reciprocity method and has higher uncertainty. Nevertheless,

the technique is easy to implement and applicable to any microphone.

1.2.3 Current limitation

Microphone technology has experienced considerable advancement. New microphone technology has applied a micro-electro-mechanical system (MEMS) in the manufacturing process. So, there is a microphone called a MEMS microphone. Thanks to the development of micromachining technology. The device comprises a transducer and an application-specific integrated circuit (ASIC). The microphone integrates a transducer and a conditioning amplifier application-specific integrated circuit (ASIC) module for the analog type of MEMS microphone. Meanwhile, for digital MEMS, the ASIC module also includes an analog-to-digital (ADC) converter circuit. All components are packed inside a microphone housing. In the construction of the MEMS microphone, the diaphragm is located inside the housing and is not exposed directly to the surrounding air. But, the sound pressure from outside flows into the diaphragm through a porthole in the housing.

The MEMS microphone product is available in various sizes. By the MEMS technology, the diaphragm and backplate size can be scaled down to 1/25 times of the conventional microphone diaphragm's size. A new material and shape design of the microphone's diaphragm and backplate design is introduced. For example, Martin *et al.* and Scheeper *et al.* developed an octagonal-shape diaphragm and backplate [5, 6]. Wood *et al.* developed a graphene-based diaphragm [7]. Some authors have proposed a perforated diaphragm and backplate [8, 9]. Despite its small size, the sensitivity and frequency response is comparable to a conventional condenser microphone.

However, the current microphone calibration methods do not apply to MEMS microphone. In the current calibration methods, the sensitivity is calculated based on the estimation of the sound field that applies to the diaphragm. The applied sound-field is estimated using a mathematical equation derived from the geometry of a conventional condenser microphone. The calibration principle can not be implemented for MEMS microphones because the MEMS microphone has a different size from the traditional microphone. The estimation of the sound field will not produce an accurate result in this case. Moreover, the inlet port size is tiny, so the analysis of the sound field on the MEMS microphone's inlet port is challenging in practice. Therefore, a new calibration method that can accommodate the MEMS microphone's size needs to be developed.

1.3 Optical method for sound measurement

Optical sound measurement utilizes light as a sensor to measure sound pressure. The method can measure sound without disturbing the sound field, which is the optical method's advantage over the microphone method, where the microphone's body disturbs the measured sound field. This condition results in decreased measurement result accuracy. The optical method can also take sound measurements in places that cannot be reached by the microphone, such as measuring sound in a

narrow gap or measuring sound in a closed cylinder.

There are two methods available for realizing sound measurement using the optical method. The first method is based on the relationship between sound pressure and particle velocity. A laser Doppler shift technique [10, 11] and photon correlation spectroscopy technique have been proposed for the measurement of the particle velocity [12,13]. In the implementation, the seeding particle is used to obtain a sufficient photon count [14]. The second method is based on the acousto-optic effect principle that describes the relationship between sound pressure and phase of the light [15, 16]. The phase shift of the light propagating through a sound field corresponds to the line integral of sound pressure along the optical path. A laser Doppler vibrometer [17,18] or polarization interferometry technique [19] can be implemented for the measurement of the phase shift. The implementation is simpler than the first method because it does not require seeding particles in the measurement process. By applying the tomography technique in the measurement process, it is also possible to obtain the sound field's projection. A reconstruction technique such as the filtered back-projection technique can reconstruct the sound field from its projection [20]. This sound field measurement method has been realized to measure sound field inside a closed tube [21].

1.4 Research objective

This research aims to apply the optical sound measurement method to address current limitations in microphone calibration methods. In the first application, the optical method is proposed for MEMS microphone calibration. A non-invasive sound measurement using the optical method is proposed to obtain the sound field applied to the microphone. The measured sound field is used to determine the sensitivity of the UUT microphone.

The sound field measurement is realized using an optical method based on the acousto-optic effect principle. A parallel phase-shifting interferometry (PPSI) instrument is used to measure the light's phase shift to the sound. The applied sound field projection is obtained by implementing scanning tomography using PPSI and reconstructed by using the filtered back-projection technique.

An experimental calibration using the optical method was carried out to determine the sensitivity of a MEMS microphone under test. The calibration was conducted for several frequency points to obtain the frequency response of the microphone. These sensitivity values were validated by the realization of the substitution calibration method. Validation of the sensitivity results was performed by calibrating the MEMS microphone under test using the substitution calibration method.

In the second application, I proposed the optical method for the determination of the microphone's acoustic center. The acoustic center's value represents the position of an equivalent point source of a microphone acting as a transmitter unit. It is used in the reciprocity method for the calculation of acoustical transfer impedance. The conventional method determines the microphone's acoustic center using the transfer function method.

I propose a new approach in the acoustic center determination by introducing the optical method approach. The acoustic center is determined from the optical projection of the sound field generated by a microphone's optical projection's sound field.

A PPSI instrument is used to obtain a projection of sound field generated by a laboratory standard microphone type B&K 4180. The microphone is configured as the transmitter unit where the generated sound pressure level is adjusted from the input voltage that drives the microphone. The microphone is positioned in the measurement area of the PPSI instrument. Projection is obtained by positioning the microphone inside the PPSI's measurement area. The PPSI instrument can record the spatio-temporal sound pressure generated by the microphone for further processing by this configuration.

The propagation of sound from the microphone is assumed to follow a point source model. Therefore, I developed a point source model and applied the least square fitting method to the measurement data. The resulting model's parameter is used to determine the origin of the measurement data's point source. This origin corresponds to the position of the acoustic center of the microphone under test.

The proposed method was implemented in the experiment to determine the acoustic center of laboratory standard microphone type B&K 4180. Experiments were performed to determine the acoustic center of the microphone at several frequencies. Comparison of the result with the nominal acoustic center values described in the standard IEC 61094-3 was performed to evaluate the proposed method's performance.

1.5 Thesis organization

The organization of this thesis is illustrated in Fig. 1.1. The introduction of the research and objective are discussed in Chapter 1.

In Chapter 2, I present the literature review corresponding to the research. I explain the methods of microphone calibration and the theory of optical sound measurement. The reciprocity and substitution microphone calibration methods are presented. I also describe the fundamental principle of optical sound measurement, including the acousto-optic effect, interferometry system, and tomography technique for the sound field reconstruction.

Chapter 3 presents the realization of optical sound measurement using a laser interferometer system. Firstly, I explain the numerical simulation of the optical sound measurement method. I continue explaining the experimental measurement of sound generated by a loudspeaker in a free field environment and the sound inside a cylindrical tube using a laser Doppler vibrometer. I confirmed the actual sound pressure level using a microphone and show that the optical method produces a good agreement. In Chapter 4, I introduce the parallel phase-shifting interferometry instrument for sound field measurement. An experiment was conducted to characterize the acoustic background noise, and optical distortion of the PPSI instrument are presented. I found PPSI's fan contribution to the sound measurement and the type of optical distortion in the PPSI system.

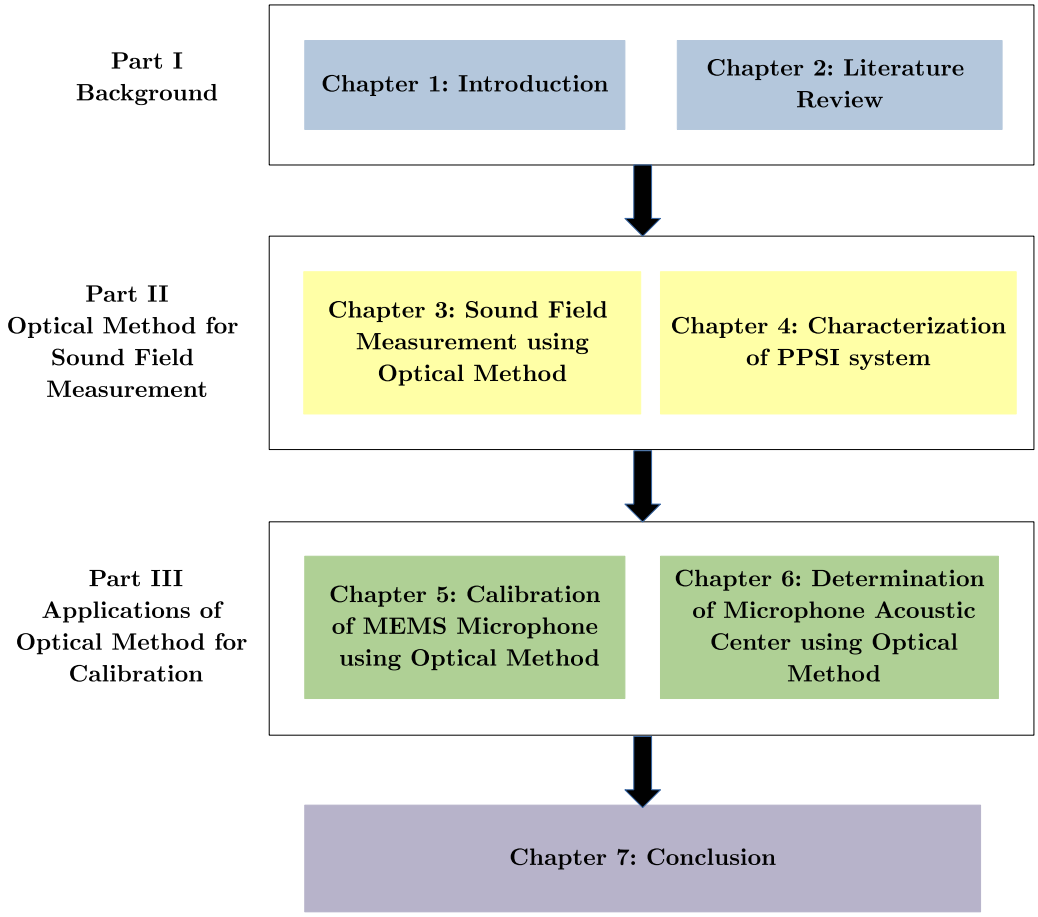

Figure 1.1: The organization of the thesis.

The main contribution of this research is described in Chapter 5. I propose applying the optical sound measurement method to measure the sound field applied to MEMS microphone surface and is used to determine the microphone sensitivity. Experimental calibration of MEMS microphone was carried out in the frequency range of 1000 Hz to 12000 Hz. I implemented the substitution calibration method to calibrate the MEMS microphone by developing an adapter to validate the sensitivity result. The result shows that both methods have a good agreement with small discrepancies. Chapter 6 presents the optical method's application to determine the microphone's acoustic center used in the reciprocity calibration method. The acoustic center is calculated from the sound field projection obtained using the PPSI instrument. A simulation was created to review the performance of the estimation method. An implementation of the proposed approach to determine the acoustic center of laboratory standard microphone type B&K 4180 was presented in this chapter. The validation of the proposed method was performed by comparing the result with the nominal acoustic center values described in the IEC 61094-2 standard. The highlights of the research and recommendations for future work are summarized in Chapter 7 of this thesis.

Chapter 2

General knowledge

2.1 Microphone

2.1.1 Condenser microphone

The microphone is a transducer that converts sound into an electrical signal. According to the basic principle, the microphone can be classified into three types: dynamic, condenser and ribbon microphone [22]. The differences between each of microphone are described as follows:

- Dynamic microphone: works based on electromagnetism principle. The construction is similar to a loudspeaker that comprises a membrane, moving coil, and a permanent magnet. The working principle is the opposite of the loudspeaker principle. When the sound vibrates the membrane, the moving coil cuts the magnetic flux and creates a current flows through the coil.

- Condenser microphone: works based on the capacitor principle. The construction of the microphone comprises a diaphragm and a fixed plate separated by an air gap. Variation of the pressure applied onto the diaphragm changes the microphone's capacitance and produces an output voltage.

- Ribbon microphone: The microphone's construction consists of a permanent magnet and a ribbon plate placed between the magnet poles. The variation of air particle velocity caused by the sound moves the ribbon plate. The interaction between the plate and the magnetic flux creates a current flow on the plate.

Among those types of microphones, the condenser microphone is commonly used in applications because it offers better acoustic performance and a simple mechanical design.

The construction of a condenser microphone is shown in Fig. 2.1. The diaphragm and the backplate with the area of A is separated with the distance of D_0 in air medium with the dielectric constant of ϵ_0. Thus, forming a plate capacitance of C. A polarization voltage E_0 is applied to the microphone. The result is

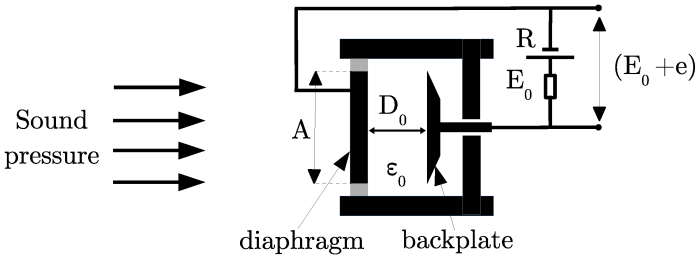

Figure 2.1: Construction of a condenser microphone.

a constant charge on the plate capacitor Q_0, and can be formulated as

$$\begin{aligned} Q_0 &= E_0 \cdot C \\ &= E_0 \cdot \frac{\epsilon_0 \cdot A}{D}. \end{aligned} \tag{2.1}$$

The applied pressure on the diaphragm moves the diaphragm with the displacement magnitude of d. As the result, the plate capacitance changes. With the constant charge, the output voltage correspond to the displacement of the diaphragm can be derived from Eq. 2.1 as follows

$$\begin{aligned} (E_0 + e) \cdot \frac{\epsilon \cdot A}{(D_0 + d)} &= E_0 \cdot \frac{\epsilon \cdot A}{D_0} \\ e &= E_0 \cdot \frac{d}{D_0} \end{aligned} \tag{2.2}$$

From Eq. 2.2, we can see that the output voltage by the microphone is linearly proportional to the displacement of the diaphragm. While the relation between the displacement of diaphragm and sound pressure is determined by the stiffness of the diaphragm and air cavity [23].

(a) RØDE NT45-C (b) B&K 4180

Figure 2.2: An example of condenser microphones for measurement [23, 24].

Fig. 2.2(a) [24] shows an example of commercial class microphone. This kind of micrcophone is commonly used in general application such as in the studio recording. A laboratory standard type of microphone is shown in Fig. 2.2(b) [23]. This is special kind of microphone that is used as the reference standard for calibration of other microphone. The advantages of laboratory standard microphone over lower

class of microphone is that it meets the microphone specification requirements for calibrating other microphones as stated in the IEC 61094-1. Laboratory standard microphone is a reciprocal transducers that can be used as an acoustical transducer as well as a loudspeaker if we apply an input voltage to the microphone terminal. Furthermore, this type of microphone has high stability of sensitivity over a very long period time [25].

Microphone sensitivity shows conversion performance of the transducer from the sound pressure to the voltage. The value is calculated as the ratio between the output voltage for applied sound pressure to the diaphragm. The general unit of microphone sensitivity is millivolt per pascal (mV/Pa). Since the sound pressure is commonly expressed as a logarithmic ratio quantity with the unit of decibel (dB). Hence, the microphone sensitivity can also be expressed in dBV/Pa. The conversion of the sensitivity unit from mV/Pa to dBV/Pa is as follow

$$M_{dB} = 20 \cdot \log\left(M_{volt}\right), \tag{2.3}$$

where M_{dB} is the microphone sensitivity in the unit of dBV/Pa M_{volt} is the microphone sensitivity in the unit of V/Pa.

Depending on the acoustic field used for calibration, the sensitivity can be expressed either as pressure field sensitivity or free-field sensitivity. When the calibration is carried out in the pressure field, such as in an acoustic coupler, the resulting sensitivity is pressure field sensitivity. Otherwise, if the calibration is carried out in the free field environment, such as in an anechoic chamber, the resulting sensitivity is termed free-field sensitivity.

Microphone sensitivity has frequency dependencies caused by a non-linear characteristic of the diaphragm stiffness response to the input frequency. The sensitivities of the microphone for certain frequencies are expressed as frequency response. Below is the typical frequency response of microphone type B&K 4180 that is calibrated in pressure field and free-field environment.

It is seen from Fig. 2.3 that the pressure field frequency response of microphone type B&K 4180 is flat in the frequency range 500 Hz to 8000 Hz and slightly changed in the high-frequency range. On the other hand, the free-field frequency response is flat at low-frequency range and increases from frequency 2000 Hz. This condition is happened because of the damping factor and resonance frequency of the microphone.

2.1.2 Micro-electro mechanical system microphone

The development of micro-electromechanical system (MEMS) technology began with the application of silicon technology for miniaturizing electronic circuits in an integrated circuit (IC). The branch of science that studies this subject is microelectronics. By employing such a lithography technique in the manufacturing process, active and passive electronic components such as the transistor, resistor and capacitor, and wire interconnect are integrated into the silicon wafer chip. The number of components that can be incorporated into the IC is also increasing by

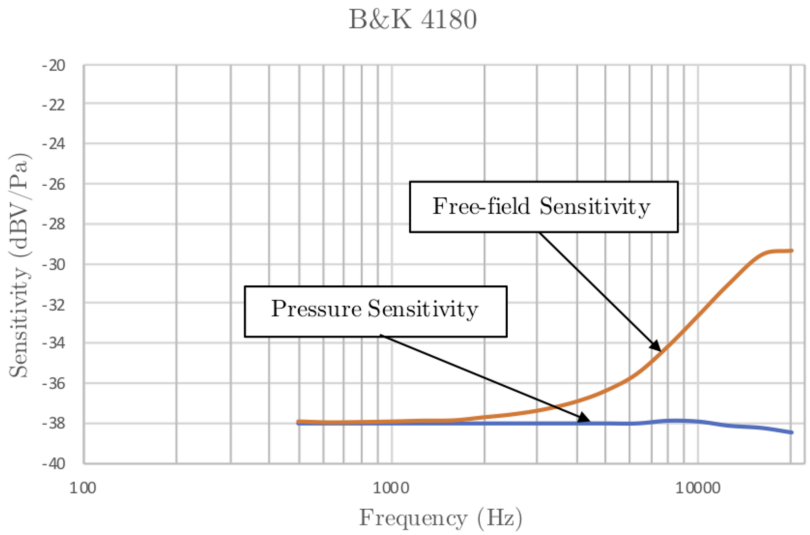

Figure 2.3: Frequency response of microphone type B&K 4180 [26].

the year, starting from Large Scale Integration (LSI) containing about 300000 components to the Very Very Large Scale Integration (VVLSI) containing more than 1.5 million components in a chip. Moore predicted that the number of transistors in the IC doubles every two years, which is known as Moore's Law [27].

With the advancement of material technology and microfabrication engineering, it is possible to miniature the circuit and the mechanical system on a chip. For example, it is possible to design motor, gear, and spring using MEMS technology [28–30]. In the acoustic field, the microphone can be fabricated using MEMS technology. For example, miniaturization of a piezoelectric thin film for acoustic sensor [31, 32]. It has also been successfully implemented to scale down the size of capacitive microphone [33, 34].

Basic construction of the MEMS microphone consists of a diaphragm, backplate, pre-amplifier, and wire interconnect. These parts are packed inside the microphone housing with an inlet port. The sound pressure from the outside flows into the microphone's diaphragm through the inlet port. Based on the port's location in the housing, the MEMS microphone can be classified into two types: top port and bottom port as seen in Fig. 2.4.

(a) Top port MEMS

(b) Bottom port MEMS

Figure 2.4: Type of MEMS microphone based on port location.

According to the output voltage, the MEMS microphone can be categorized into two types, analog and digital. The analog type contains a pre-amplifier circuit. Instead of a pre-amplifier, the digital type also includes an analog-to-digital (ADC) converter and an interfacing circuit. This circuit is implemented as an application-specific integrated circuit (ASIC) that requires external power. Therefore, the MEMS microphone requires external power to make it works.

The MEMS microphone is commonly available in the market as a breakout board. This breakout contains a MEMS microphone and necessary external passive components that are already soldered on a printed circuit board (PCB) to make it easy to interface with other devices.

An example of the MEMS microphone breakout component is Knowles SPU0414 HR5H-SB. This is the analog top port type of MEMS microphone. The breakout component and its schematic diagram are shown in the Fig. 2.5(a) and 2.5(b), respectively.

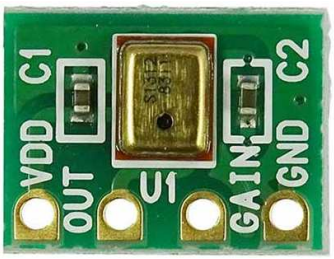

(a) MEMS microphone breakout [35].

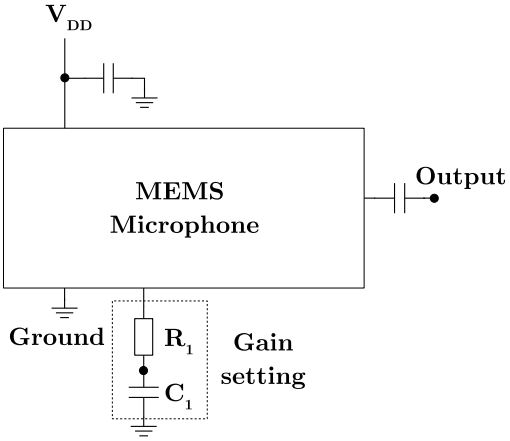

(b) Schematic diagram of the breakout

Figure 2.5: The MEMS microphone breakout and its schematic diagram.

The microphone housing has the size of 2.95 mm in width, 3.76 in length, and 1.10 mm in height. The device requires an external power supply with the minimum input voltage of 1.5 volt and the maximum of 3.6 volt. This microphone has an inlet port diameter of the 0.5 mm. The pre-amplifier gain is adjustable by configuring the value of R_1 and C_1. The calculation of the gain is using following equation:

$$Gain(dB) = 20 \cdot \log\left(1 + \frac{R_F}{(R_S + R_1)}\right), \tag{2.4}$$

where the value of $R_F = 22\ k\Omega$ and $R_S = 2.44\ k\Omega$. The minimum measurement frequency range of the microphone can be adjusted by selecting the value of C_1 as follow:

$$F_{min}(Hz) = \frac{1}{2\pi(R_S + R_1)C_1}. \tag{2.5}$$

2.2 Microphone calibration methods

The sensitivity information is provided by the manufacturer in the microphone datasheet that is called the nominal sensitivity value. However, each microphone's actual sensitivity value may differ from the nominal value due to many factors. Calibration is required to determine the actual sensitivity of a microphone. The sensitivity value of a microphone is changing over time, caused by the usage and environmental condition. Therefore, regular calibration is important to know the updated sensitivity value.

The international methods for microphone calibration are published by the International Electrotechnical Commission (IEC) in the 61094 series standard. This series standard contains eight parts, which describe laboratory standard microphone, calibration methods and procedures, and the measurement uncertainty. According to these standards, the calibration methods consist of an electrical method and an acoustic method. The acoustical methods are the reciprocity method, comparison/substitution method, and the electrostatic actuator's electrical method. The following section describes the acoustical methods for microphone calibration.

2.2.1 Reciprocity calibration method

The microphone reciprocity method was introduced by Cook [36] based on Lord Rayleigh's reciprocity theorem [37] and the Ballantine experiment using a moving-coil sound source measured using Rayleigh disk method [38]. The reciprocity principle describes that the ratio of the volume velocity produced by a transmitter microphone to the input current is equal to the ratio of the receiver microphone's output voltage to the sound pressure acting on the diaphragm [39]. The ratio represents the sensitivity of the microphone. Therefore, the microphone's sensitivity that acts as a transmitter is equal to its sensitivity as a receiver. In the implementation, the calibration method is realized as a voltage transfer function (VTF) measurement and applies to a reciprocal microphone.

The microphone configuration in the reciprocity calibration method is shown in Fig. 2.6. In this configuration, microphone Mic_A functions as the transmitter and

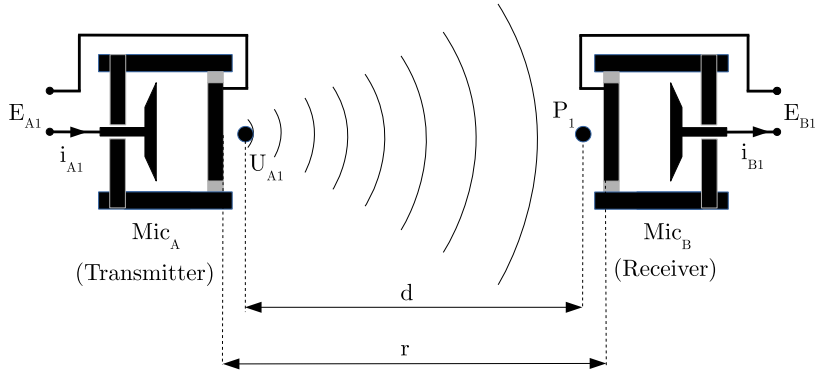

Figure 2.6: Reciprocity calibration configuration where Mic_A as the transmitter and Mic_B as the receiver.

microphone Mic_B is used as the receiver. An electrical voltage of E_{A1} is applied to the input port of Mic_A produces an electrical current of i_{A1}. The amount of current is given by

$$i_{A1} = \frac{E_{A1}}{Ze_A}, \tag{2.6}$$

where Ze_A is electrical transfer impedance which is determined from microphone capacitance using the following equation

$$Ze_A = \frac{1}{j\omega C_{Mic_A}}. \tag{2.7}$$

The volume velocity produces by the transmitter microphone Mic_A which has the sensitivity of M_1 is

$$U_{A1} = \frac{M_A}{i_{A1}}. \tag{2.8}$$

These two microphones are separated with a distance of r, measured from the diaphragm of the microphone. Sound pressure of P_1 is acting on the diaphragm of Mic_B caused by the volume velocity of U_{A1}, The amount of sound pressure can be estimated by using the following equation

$$P_1 = \frac{U_{A1}}{Za_{AB}}, \tag{2.9}$$

where Za_{AB} is acoustical transfer impedance between the microphones. This acoustical transfer impedance can be calculated as

$$Za_{AB} = j\frac{\rho f}{2d}e^{-jkd}e^{-\alpha r}, \tag{2.10}$$

where
ρ = density of air
f = frequency of measurement
k = angular wavenumber
d = distance between the microphone's acoustic center
α = sound attenuation in air

Based on Eq. 2.8, we can re-write equation 2.9 as

$$P_1 = \frac{M_A}{i_{A1}}Za_{AB}. \tag{2.11}$$

The output voltage produced by the receiver microphone caused by the applied sound pressure is determined by the sensitivity as

$$E_2 = \frac{M_B}{P_1}. \tag{2.12}$$

Then, we can substitute the P_1 with the Eq. 2.11 to obtain E_2 as follows

$$E_2 = M_B\frac{M_A}{i_{B1}}Za_{AB}. \tag{2.13}$$

The value of i_{B1} is equal to the ratio of output voltage to the electrical transfer impedance as

$$i_{B1} = \frac{E_{B1}}{Ze_B}. \tag{2.14}$$

Finally, we can re-write Eq. 2.13 into

$$\begin{aligned} E_2 &= M_A M_B \frac{E_{A1}}{Ze_B} Za_{AB}. \\ M_A M_B &= \frac{E_{B1}}{E_{A1}} \frac{Ze_B}{Za_{AB}} \end{aligned} \tag{2.15}$$

From the above equation, we can see that product of microphone sensitivity is equal to the ratio of input and output voltage, electrical transfer impedance, and acoustical transfer impedance. The value of electrical transfer impedance is determined from microphone capacitance which can be obtained from the microphone specification datasheet. A more accurate method to determine microphone capacitance is proposed by Yan *et al.* [40]. To calculate acoustical transfer impedance accurately, several parameters are required such as microphone front cavity depth, temperature, ambient pressure, humidity, and microphone acoustic center. The contribution of these parameter to the calculation of of acoustical transfer impedance are given in the IEC standard.

2.2.2 Substitution calibration method

The reciprocity method described in the previous section produces an accurate sensitivity result. An uncertainty of 0.01 dB in the sensitivity result can be achieved using the reciprocity method. However, the method applies only to a reciprocal microphone. The realization of the method is difficult, especially for the free field reciprocity method. The measurement noise is high caused by a low signal to noise ratio.

The most straightforward way to determine the sensitivity of a microphone is to expose the microphone to a reference sound source that the sound pressure level. A calibrated pistonphone or acoustic calibrator can be used for this purpose. The sound calibrator can generate a stable sound pressure with a nominal level of 94 dB, which is equivalent to a sound pressure of $1.002374467Pa$, at a single frequency of 250 Hz.

In practice, the sound calibrator should be calibrated before used to determine the actual sound pressure level. Then, we use the sound pressure level value for the microphone calibration. The calibration procedure is described as follow:

1. Connect the microphone under test to the preamplifier, and the output is connected to a voltmeter.

2. Attach the microphone under test into the pistonphone or sound calibrator.

3. Turn on the acoustic calibrator and note the voltage output displayed by the voltmeter as the value of V_{out}.

The microphone's sensitivity under test can be calculated from the ratio of the pressure to the output voltage.

$$M_{DUT} = \frac{V_{out}}{SPL_{acousticcalibrator}}, \tag{2.16}$$

where V_{out} is the output voltage of the microphone under test.

The sensitivity is expressed in dBV with the reference of $1V/Pa$ using the following equation:

$$M_{DUT_{dB}} = 20 \cdot log_{10}(M_{DUT}). \tag{2.17}$$

Using this method, we can determine the sensitivity of the microphone at the frequency of 250 Hz.

The substitution calibration method is described in the IEC 61094-5. This standard also described a comparison method that has almost the same calibration procedure. In this method, the microphone's sensitivity under test is determined from the reference microphone's sensitivity. This method's basic principle is to apply the same sound field to both reference and the microphone under test. Thus, both microphones experience the same sound field. The comparison method and the substitution method are the sound field exposure method to the microphones. The method is named as the comparison method when the reference and microphone under test are positioned close to each other so that the sound field applies simultaneously. When the sound field applies to the microphones sequentially, the method is named the substitution method.

Instruments setup for the implementation of comparison calibration method is shown in Fig. 2.7 A loudspeaker is used to generate the sound field. The position of

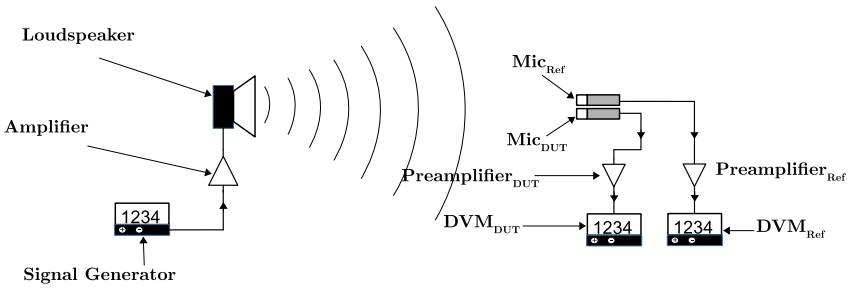

Figure 2.7: Setup of the comparison calibration method.

the reference and microphone under test should be close to each other so that the sound pressure level applied to each microphone is equal. The calibration sequence is described as follow:

1. Generate the sound field at the frequency of calibration.
2. Note the output voltage measured by the DVM_{Ref}. Using the sensitivity value of the reference microphone in the unit of mV/Pa at the calibration frequency and the output voltage, then we can determine the applied sound pressure level in Pascal unit at the measurement position as

$$SPL_{Ref} = \frac{DVM_{Ref}}{M_{Ref}}. \tag{2.18}$$

3. Calculate the sensitivity of the microphone under test from the applied pressure that has been defined previously.

$$M_{DUT} = \frac{DVM_{DUT}}{SPL_{Ref}}. \tag{2.19}$$

4. Repeat the process for other calibration frequency range

The advantage of the comparison method is simpler in the configuration and faster calibration time. But, we need to consider that the reflection of sound, either by the body of reference and microphone under test, will disturb the sound pressure applied to the microphone. This reflection effect should be added in the calculation of the calibration uncertainty.

The same principle applies to the substitution method. The sound pressure level measurement is performed sequentially by each microphone. The procedure is described as follows. In the first configuration, the reference microphone is positioned at a certain distance d from the loudspeaker. Then, sound pressure generated by the loudspeaker is measured by the reference microphone as shown in Fig. 2.8. The

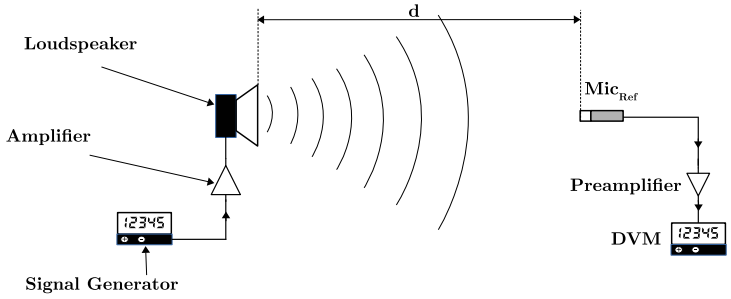

Figure 2.8: Measurement of sound by the reference microphone.

reference microphone's sensitivity placed at a distance of d from the loudspeaker and its output voltage measured by DVM can be used to calculate the sound pressure applied to the diaphragm using Eq. 2.18. After that, the reference microphone is substituted using the microphone under test at the same position as shown in Fig. 2.9 The sensitivity of the microphone under test is then calculated using the

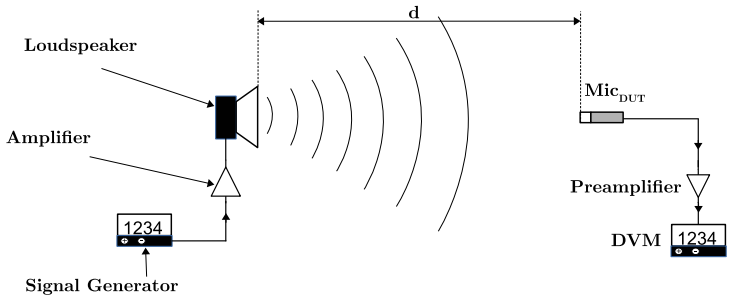

Figure 2.9: Measurement of sound by the microphone under test.

same procedure as the comparison method. Since the measurement is performed

sequentially between the reference and microphone under test, then the effect of reflection from another microphone does not present in the measurement process. However, the placement of the microphone became the most important factor contributing to the calibration uncertainty. When we substitute the microphone, we have to confirm that the microphone under test is at the same position as the reference microphone so that both microphones experience the same sound pressure level.

2.3 Optical measurement system

2.3.1 Laser interferometry

Light is an electromagnetic wave. The wave that can be quantified is intensity amplitude, wavelength, frequency, period, and phase. Amplitude represents the height of the crest or trough of a wave relative to its equilibrium state. Wavelength is defined as the distance between the adjacent trough or a crest of the wave expressed in the meter unit. The period is the time, in seconds, to complete one cycle of a wave from crest-to-crest or trough-to-trough. Frequency is the number of waves that pass a point in one second and is represented in Hertz's unit (Hz). The wave phase represents the current wave position relative to the reference position measured in the unit of degree or radian.

As a wave, the light also experiences some physical phenomena such as reflection, refraction, diffraction, and interference. Reflection is the change of wave propagation caused by an incident on an obstacle object's surface. Refraction is the bend of the wave propagation when they enter a medium with different properties from a certain angle. Diffraction is the change of the waveform when the wave passes through an aperture or slit. Interference occurs as a result of the superposition of two waves in the same medium. The interference result produces a new wave with different properties. For example, when the source waves have the same phase properties, then the interference result is a wave that has a larger amplitude than the source wave. Conversely, when the wave sources are out of phase, destructive interference occurs, and the resultant of the wave amplitude is cancel out each other.

The working principle of laser interferometry utilizes light interference. The simplest optical configuration of laser interferometry is the Michelson type. Fig. 2.10 shows optical configuration of Michelson type interferometry.

A laser with a complex magnitude of $A = aexp(-i\phi)$ is used as the beam source. The beam is split into two beams in the perpendicular direction using a beam splitter. One laser beam is directed onto a reference mirror, and the other beam is directed onto an object mirror. Each beam has the complex magnitude of $A_1 = a_1 exp(-i\phi_1)$ and $A_2 = a_2 exp(-i\phi_2)$, respectively. The value of a_1 and a_2 represent the amplitude of beam 1 and beam 2, while phi_1 and phi_1 represent the phase of the corresponding beam. The beam splitter recombines the reflected beams from the mirrors again to produce interference. Finally, the mixed beam is passed to a photodetector to convert into an electrical signal for signal analysis [41, 42].

The interference of the light correspond to the superposition of the beam ex-

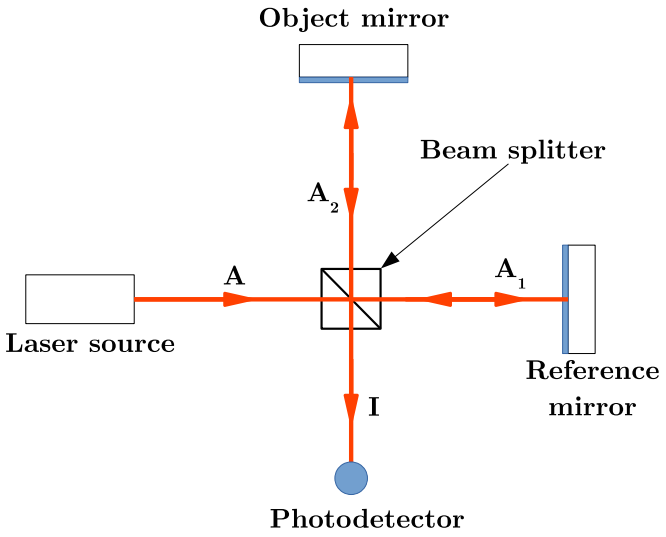

Figure 2.10: Basic configuration of laser interferometry.

pressed by variable I. The magnitude of I is formulated as

$$\begin{aligned} I &= |A_1 + A_2|^2 \\ &= (A_1 + A_2)(A_1^* + A_2^*) \\ &= |A_1|^2 + |A_2|^2 + 2(A_1 A_2)^{1/2} cos(\Delta\phi). \end{aligned} \tag{2.20}$$

The variable A_1^* and A_2^* is complex conjugate of the beam magnitude and $\Delta\phi$ is the phase difference of the laser beams ($\Delta\phi = \phi_1 - \phi_2$).

From Eq. 2.20, we see that the value of I is equal to the summation of beam A_1 and A_2 when destructive interference occurs. Moreover, the value of I is higher when constructive interference occurs, yield a brighter beam. If the beams' phase difference varies linearly, then the value of interference light intensity I change cosinusoidally. Thus, creating a dark and light intensity pattern, which is called the fringe pattern.

Constructive interference occurs when there is no phase difference between the two beams. Conversely, destructive interference occurs when the phase of beam A_2 is the opposite phase A_1. When the object mirror is moving back and forth periodically, then the phase difference will change in the range of 0 to π radians. The phase changes proportionally as a function of the optical path length difference of the two beams. The relation between the optical path difference Δp and the change of phase, $\Delta\phi$, is formulated as follow

$$\Delta p = (\lambda/2\pi)\Delta\phi. \tag{2.21}$$

2.3.2 Laser Doppler vibrometer

An example of an instrument that implements laser interferometry principle is the laser Doppler vibrometer (LDV). The LDV uses the Doppler frequency shift to

measure surface vibration. According to the Doppler effect principle, if a sound source is moving relative to the stationary observer. Then, the frequency of sound received by the observer is shifted. The LDV instrument is widely used in many applications such as structural health monitoring, MEMS devices characterization, machinery vibration analysis, medical analysis, and acoustics measurement [43, 44].

The basic optical configuration of an LDV instrument is shown in Fig. 2.11 [41, 45]. A laser with a frequency of f_r is used as the light source. Commonly,

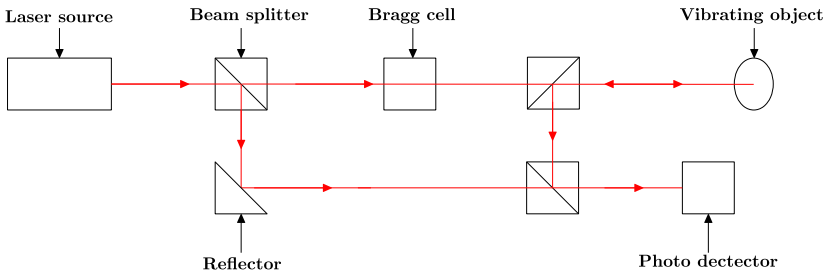

Figure 2.11: Basic building block of a laser Doppler vibrometer.

a helium-neon laser, which has a frequency of 4.471×10^{-10} is used for the LDV system. The beam splitter divides the beam onto the object beam and reference beam. The object beam passes the beam splitter and goes to the Bragg cell. This Brag cell is used to generate a frequency shift of f_b. The resulting frequency yield by the Bragg cell is $f_r + f_b$. The beam is then passing the second beam splitter and goes to the vibrating object surface or a mirror attached to an object. The reflected beam has a frequency of $f_r + f_b + f_d$. Finally, the reference beam and the object beam are mixed and directed toward the photodetector. The frequency shift produced by the vibrating object is determined by

$$f_d = 2 * \frac{V(t)}{\lambda}, \tag{2.22}$$

where $V(t)$ is the vibration velocity of the object, and λ is the laser's wavelength.

2.3.3 Parallel phase-shifting interferometry

Parallel phase-shifting interferometry or commonly abbreviated as PPSI is an instrument that applies the interferometry principle to measure the phase shift of the light. The instrument implement phase-shifting interferometry method [46, 47]. Using the PPSI instrument, it is possible to obtain the phase shift of light over an area of measurement because the laser beam's size is expanded optically. Not only spatial phase-shift information, but we can also obtain temporal phase shift variation over time. This is because the PPSI is equipped with a high-speed polarization camera to capture the light interference. The PPSI system has successfully implemented for visualization of aerodynamic sound [48].

The basic building block of PPSI is shown in Fig. 2.12 [49]. The PPSI uses a green laser source with a wavelength of 532 nm. The type of interferometer applied in the PPSI system is the Fizeau-type polarization interferometer. A Wollaston

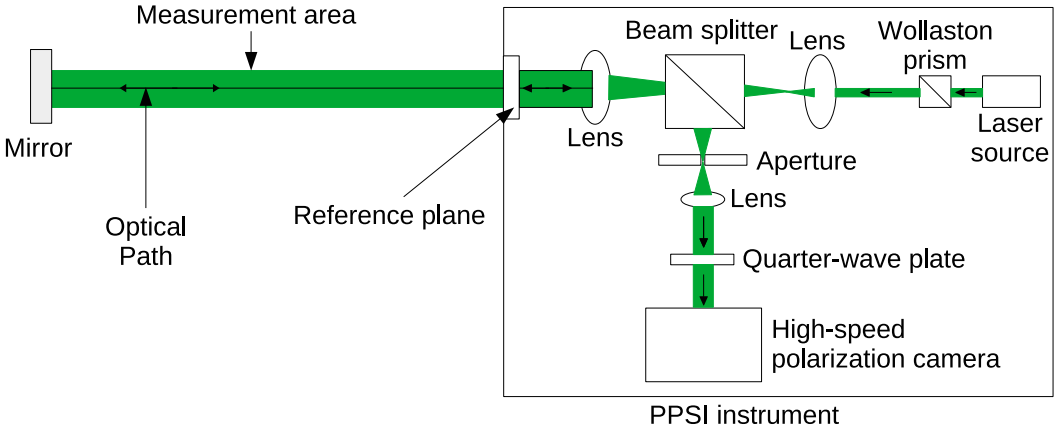

Figure 2.12: Basic building block of PPSI.

prism is used to generate two orthogonal linearly polarized beams whose optical axis slightly differ and passes to the non-polarized beam splitter. A lens is used to expand the laser beam diameter to 10 cm in diameter and direct the reference beam and object beam toward the reference plane. The reference beam is reflected by the reference plane while the object beam passes the reference plane and propagating toward the mirror. The mirror reflects the laser beam to the reference plane.

An optical flat that reflects a small portion of the incident light is slightly tilted toward the mirror so that one polarization of the reference light and other polarization of the object light overlap at the center of the aperture. The light passing through the aperture is the superposition of the orthogonally polarized object beam and the reference beam. A quarter-wave plate is used to produce contra-rotating circular polarized light. Finally, the beam incident goes toward the high-speed polarization camera [50]. The PPSI uses a high-speed camera CRYSTA PI-1P made by Photron Ltd. The pixelated polarizer with the phase retardation element of ϕ_{ret} = (0, $\pi/2$, π, $3\pi/2$) is attached to each of 2×2 arrays of the neighboring image sensor that allows the camera to capture multiple phase-shifted interferograms in a single shot and incorporated into a single image [49, 51].

Image intensity captured by the sensor is represented in the 12-bit grayscale level. The image's maximum resolution is 1024×1024 and achieved when the sampling rate is less than 7000 frames per second (fps). The image's resolution decreases as the sampling frequency increases with the maximum frequency sampling of 1.5×10^6 fps. The captured image is temporarily stored in the internal memory of the camera system. The operation of the camera is controlled by a software Fastcam Viewer developed by Photron. The software performs the transfer process from the internal memory of the camera to the external storage. The saving image format can be selected from the software.

2.4 Sound field measurement using optical system

2.4.1 Acousto-optic effect principle

A sound is a form of energy produced by vibrations of air molecules in a medium. The amplitude of the sound is described as the number of molecules moved by the vibration. In the adiabatic process, the rate of air pressure changes in sound corresponds to the rate of air volume change. This is described by the following equation [16]

$$\begin{aligned} \frac{p}{p_0} &= -\gamma \frac{\Delta V}{V}, \\ p_0 \gamma &= c^2 \rho, \end{aligned} \tag{2.23}$$

where p, p_0, ΔV, V_0, γ, c, and ρ is actual sound pressure, static air pressure, air volume changes, air volume at static condition, the ratio of specific heats constant, sound speed, and density of air, respectively.

Equation 2.23 implies that the volume change is also related to the air density change. The relation between the density of air and the air refractive index is described using Gladstone and Dale relation [52,53]. By assuming the linear process, we obtained the relation between air refractive index and sound pressure as

$$n \cong n_0 + \frac{n_0 - 1}{\gamma p_0} p, \tag{2.24}$$

where n_0 is air refractive index at atmospheric condition.

The geometrical optics describes the relationship between the air refractive index and phase of light propagating through the medium as

$$\phi(r,t) = k_0 \int_{L(r)} n(l,t) dl, \tag{2.25}$$

where k_0 is wave number of the light, n is air refractive index and $L(r)$ is the path following by the beams of the light in the Euclidean space $r = (x, y, z)$ [20,54]. The relation between the sound field and a phase of light that pass through it can be determined by substituting air refractive index change in Eq. 2.25 with Eq. 2.24 as

$$\phi(x,y,t) = k_0 n_0 |L| + k_0 \frac{n_0 - 1}{\gamma p_0} \int_0^Z p(x,y,z,t) dz, \tag{2.26}$$

where the z-axis is parallel to the beam, x-axis, and y-axis are coordinates of the plane perpendicular to the z-axis. If the static term in Eq. 2.26 is removed, then we obtained the following equation,

$$\phi_s(x,y,t) = k_0 \frac{n_0 - 1}{\gamma p_0} \int_0^Z p(x,y,z,t) dz, \tag{2.27}$$

with the unit of phase in radian. This equation shows that the phase of the light corresponds to the line integral of sound pressure along the optical path. Based on this equation, we can realize the measurement of the sound field using the optical method.

2.4.2 Tomography method for sound field projection

Tomography is a reliable method for image reconstruction. The method is commonly implemented in the medical field to reconstruct the inner body using X-rays. The method comprises two steps: scanning and reconstruction process. In the scanning process, parallel rays are passed through the body, and the sensor measures the rays absorption function. The scanning process is conducted from different angles to obtain the projection of the image. The original image can be reconstructed from its projection by implementing the reconstruction process. The simplest and fast reconstruction technique commonly used in tomography is the back-projection algorithm. The original image is reconstructed by projecting back the projection onto the reconstruction area. However, the back-projection algorithm introduces noise in the reconstructed image. To deal with this noise problem, the algorithm is improved by applying a spatial filter. Thus the algorithm is named as filtered back-projection [55, 56].

Tomography method can be implemented using an optical measurement system for measurement of the sound field. A scanning process using laser interferometry is used to obtain the sound field's projection along the optical path. A sound field $P(\overline{x}, \overline{y})$ is scanned using parallel rays with the spatial scanning resolution of d. The scanning is conducted from a different angle with the resolution of θ. The result of this process is the projection of the sound field $R(\overline{x}', \theta)$. The illustration of the scanning process is shown in Fig. 2.13.

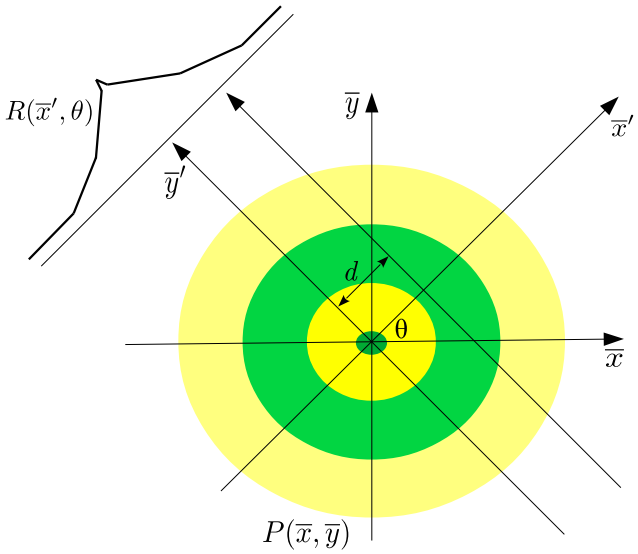

Figure 2.13: Sound field projection scanning process.

The rotation coordinate is described by the following equation:

$$\begin{pmatrix} \overline{x}' \\ \overline{y}' \end{pmatrix} = \begin{pmatrix} \cos\theta & -\sin\theta \\ \sin\theta & \cos\theta \end{pmatrix} \begin{pmatrix} \overline{x} \\ \overline{y} \end{pmatrix}. \tag{2.28}$$

The result of this scanning process is called a projection function or a sinogram where each value in projection function $R(\overline{x}', \theta)$ represents a line integral of the

sound pressure along the optical path.

According to the acousto-optic relation described in the Eq. 2.27, this line integral of the pressure corresponds to the phase shift of the light. Therefore, we can realize the measurement of the line integral of sound by measuring the light's phase shift.

Phase shift measurement can be realized either using an LDV or PPSI instrument. The realization of the measurement method for visualization of the sound field has been shown in the literature [57, 58]. The proposed method applies the acousto-optic effect principle and is measured using the LDV instrument.

The measurement configuration in the proposed method is described as follows. The laser beam from LDV is targeted to a rigid surface. Using this configuration, the LDV measures the time derivative of the phase of the light along the optical path. The LDV quantifies this time derivative of the phase as the vibration velocity. Therefore, an integration process to the vibration velocity produced by the LDV is required to obtain the phase shift.

The formula for this measurement process can be derived from Eq. 2.27. Thus, we obtain the relation between the sound pressure and the vibration velocity output of the LDV as

$$\int_L p(x, y, \omega) dl = V(\omega) \frac{\gamma p_0 n_0}{j\omega(n_0 - 1)}, \tag{2.29}$$

where $V(\omega)$ is the vibration velocity measured by LDV. Therefore the sound field projection can be obtained by measuring the vibration velocity using LDV and applying the Eq. 2.29.

A projection of sound field projection can be obtained using the PPSI [59, 60]. Since the PPSI directly measures the phase shift, an integration process is not required. Thus, the relation of sound with the phase shift of the light can be described as Eq. 2.30.

$$\int_L p(x, y, \omega) dl = \phi_s(x, y) \frac{\gamma p_0}{k_0(n - 1)}, \tag{2.30}$$

where $\phi_s(x, y)$ is the phase shift ectracted from PPSI measurement.

2.4.3 Sound field reconstruction

In the tomography method, the original image can be reconstructed from the projection. A common algorithm for reconstruction from projection is back-projection. The algorithm is easy to implement and fast due to simple mathematical operation [61]. The original image is recovered by smearing back the projection function onto the reconstruction plane with the same angle used in the scanning projection process. Mathematically, the process can be written as

$$p(x, y) = \int_0^\theta R(\overline{x}', \theta) d\theta. \tag{2.31}$$

However, the reconstructed image by this process produces a blurred image. The amount of noise is increasing as a function of spatial distance from the center

of the image. The blurring noise is formulated as

$$p(x,y) = f(x,y) \times \frac{1}{\sqrt{x^2+y^2}}. \tag{2.32}$$

The blurring noise resulted from the back-projection process can be compensated by applying a spatial filter. Because the process consists of back projection and spatial filtering, the algorithm is called filtered back-projection (FBP).

The computational of FBP algorithm can be speeded up by applying the Fourier slice theorem. The theorem describes that 1D Fourier transform of the projection is equal to the 2D transform of the original image. This means that we can apply a 2D spatial filter to the Fourier transform of the projection function. The representation of sound field projection in the frequency domain can be written as

$$R(\overline{x}', \theta, \omega) = \frac{\gamma p_0}{k_0(n_0-1)} \phi_s(\overline{x}, \overline{y}, \theta, \omega), \tag{2.33}$$

where ω is the angular frequency of sound. Therefore, the implementaion of FBP algorithm according Fourier slice theorem can be written as

$$\tilde{P}(\overline{x}, \overline{y}, \omega) = \int_0^{\pi} \int_{-\infty}^{\infty} |W(\xi)|\,|H(\xi)|\,\tilde{R}(\xi,\theta) e^{2\pi i \xi x'} d\xi d\theta, \tag{2.34}$$

where ξ is the spatial frequency bin and $\tilde{R}(\xi,\theta)$ is projection in spatial frequency domain. The variable $W(\xi)$ and $H(\xi)$ represents spatial low-pass and high-pass filters that are used to remove the blurring effect in the backprojection technique and high-frequency spatial noise in the reconstructed image.

A Ramp filter is commonly used for the high pass filter. It has the frequency response as shown in Fig. 2.14 [62]. An improvement of the conventional ramp filter has been proposed by Zeng to increase the reconstruction accuracy [63]. The modified ramp filter equation is shown in Eq. 2.35.

$$H(\xi) = \frac{1}{4} - \frac{2}{\pi^2} \sum_{l=1}^{\frac{M}{2}-1} \frac{\cos\frac{2\pi l \xi}{M}}{l^2}, \tag{2.35}$$

where l is an odd number, $M = 2\Psi - 1$, and Ψ is the number of lines used for the projection scanning.

Instead of low-frequency spatial noise, the back-projection algorithm also produces high-frequency spatial noise. This high-frequency noise occurs as a result of

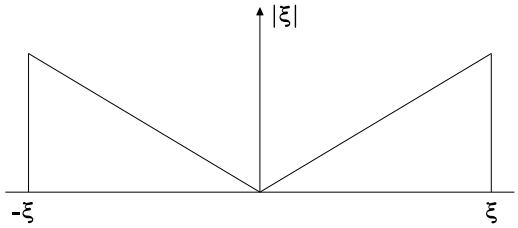

Figure 2.14: The frequency response of a ramp filter.

undersampling in parallel scanning process [64,65]. An insufficient number of parallel lines for the scanning process may cause the undersampling of a projection. The unmatching construction of the reconstruction grid also produces aliasing in the reconstruction image. This aliasing may appear as the addition of a high-frequency component to the original image. A low-pass spatial filter can be used to remove the high-frequency component of the image. However, the type of high pass filter used needs to be considered not to eliminate the image's original high-frequency component.

Several filters are available for tomography application such as Butterworth, Hamming, and Sheep-Logan [66]. The best appropriate filter for a specific application can be chosen based on the image object's characteristics being reconstructed. In general, the combination of ramp high-pass and Sheep-Logan low-pass filter produces a fairly accurate reconstructed image. The frequency response of each filter can be described as the following equation,

1. Butterworth:
$$W(\xi) = \frac{1}{[1 + (\xi/\xi_c)^{2n}]}, \tag{2.36}$$

2. Hamming:
$$W(\xi) = \begin{cases} 0.54 + 0.46\ cos(\frac{\pi\xi}{\xi_c}), & 0 \leq |\xi| \leq \xi_c \\ 0, & \text{otherwise} \end{cases} \tag{2.37}$$

3. Sheep-Logan:
$$W(\xi) = \frac{2\xi_c}{[\pi(sin|\xi|\pi/2\xi_c)]}, \tag{2.38}$$

where ξ is the spatial frequency and ξ_c is the frequency cut-off of the filter.

I have described the implementation of a fast filtering process in the back-projection reconstruction algorithm by taking advantage of the Fourier slice theorem. The temporal phase shift of the light recorded by the PPSI can be regarded as a signal that corresponds to the sound pressure variation. The phase variation is converted into the frequency domain to extract the phase shift's magnitude at the frequency of interest. The conversion process is applied to each point in the measurement area. By this process, we obtained the spatial distribution magnitude of the projection on the measurement area. Then we apply filtered back-projection to reconstruct the original signal magnitude distribution using the Eq. 2.34.

The reconstructed signal magnitude resulted from Eq. 2.34 is still in frequency domain. To reconstruct the spatio-temporal sound pressure variation on the measurement area, we need to convert back the signal to the time domain. A conversion is done by inverse Fourier transform to the signal as described by the following equation:
$$\tilde{p}(\overline{x}, \overline{y}, t) = \frac{1}{2\pi} \int_{-\infty}^{\infty} \tilde{P}(\overline{x}, \overline{y}, \omega) e^{i\omega t} d\omega. \tag{2.39}$$

Chapter 3

Implementation of optical method for sound measurement

3.1 Measurement framework

Overview about the optical method for sound field measurement has been given in Chapter 2. This research proposes an acousto-optic based tomography method using a laser interferometer to measure the sound field. There are two main processes in the tomography method, which are the scanning process and reconstruction process. The scanning process is used to obtain the projection of the sound field. Meanwhile, the reconstruction process is used to recover the measured sound field from its projection. The general sequence of the measurement process is illustrated in the flowchart as shown in Fig. 3.1.

In the first process, we perform the parallel scanning to construct the sound field's projection. This process is obtained by passing the light through the sound field of interest, where the number of parallel scanning lines determines the reconstructed field's resolution. The scanning process can be done sequentially, line by line, using a laser beam, or simultaneously using a PPSI instrument. This scanning process is repeated for different angles in the range of 0 degrees to 170 degrees. Projection from angles beyond 170 degrees produces the same projection results as the projection from the opposite angles.

In the implementation, the parallel scanning using optical measurement instrument does not produce a single projection data but for a period of time. The instrument's number of recorded data is determined by the recording time and the sampling rate of measurement. The recorded data frames of parallel scanning from different angles are stored in an instrument's memory or external disk for processing. In the context of tomography, the result of the scanning process is called a sinogram.

These sinogram data are used to reconstruct the sound field. Firstly, the parallel scanning data from different angles need to obtain data only at the measurement frequency. Magnitude at the frequency of measurement is extracted from temporal measurement data by applying Fourier transform. The process is applied to all recorded data from the parallel scanning process. Hence, we have the projection

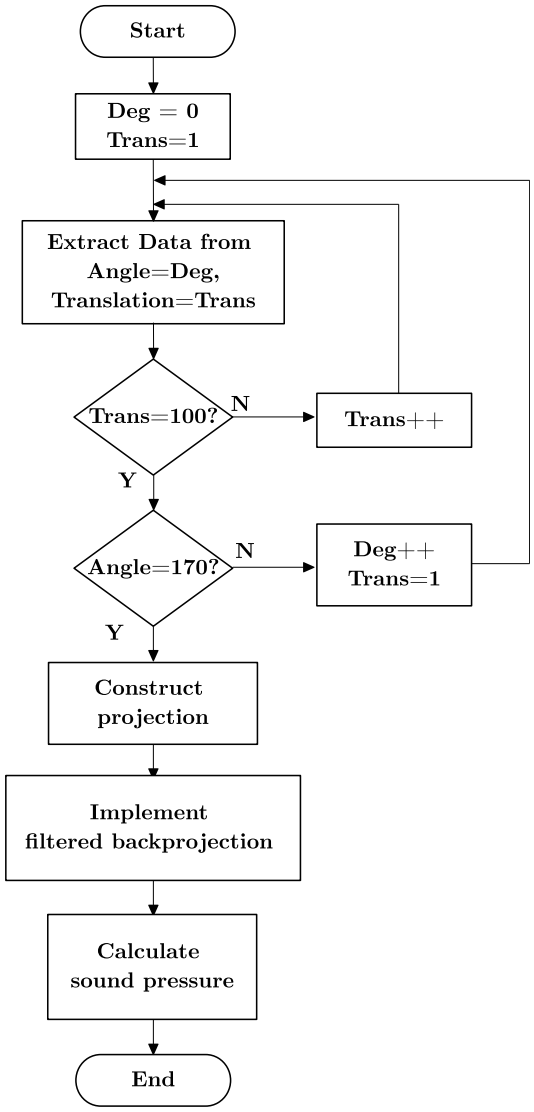

Figure 3.1: Flowchart of sound field reconstruction data processing.

of the sound field at the frequency of interest. The pseudocode of this process is shown below. Variable $RecordedData(trans, rot, \omega_t)$ is the measurement data for each translation step and rotation step in the time domain. While, variable

Algorithm 1 Pseudo-code for constructing projection from parallel scanning data

Input: RecordedData(trans,rot,t)
Output: Projection(trans,rot,ω_t)

for iii=1 to rot_num **do**
  for jjj=1 to $trans\_num$ **do**
    $Projection(iii, jjj, \omega_t) = \mathcal{F}(RecordedData(iii, jjj, t))$
  end for
end for

$Projection(trans, rot, \omega_t)$ is the frequency domain representation of the data at the measurement frequency of ω_t.

The second process is the reconstruction process using a filtered back-projection (FBP) algorithm. A Fourier slice theorem is implemented to perform filtering to the sinogram data. The filtering process is performed as the convolution between the projection data with the spatial filter. The pseudocode of the filtering process is shown in the pseudocode 2.

Algorithm 2 Pseudo-code for filtering process

Input: Projection(trans,rot,ω_t)
Output: FilteredProjection(trans,rot,ω_t)

1: $Initializefilter H(\omega_s)$
2: **for** iii=1 to rot_num **do**
3: **for** jjj=1 to $trans\_num$ **do**
4: $Projection(iii, jjj, \omega_s) = \mathcal{F}(Projection(iii, jjj, \omega_t))$
5: $FilteredProjection(iii, jjj, \omega_s) = Projection(iii, jjj, \omega_s) * H(\omega_s)$
6: $FilteredProjection(iii, jjj, \omega_t) = \mathcal{F}^{-1}(FilteredProjection(iii, jjj, \omega_s))$
7: **end for**
8: **end for**

The process is started by the definition of spatial filter parameters such as frequency cut-off and filter order. According to the Fourier slice theorem, the 2D spatial filtering of the projection can be implemented by applying the 1D filter to the projection data from each angle. To do the filtering, first, we need to convert the projection data from each angle into a spatial frequency domain using the Fourier transform. The filtering process is then calculated as the multiplication operation between the projection data and the filter response. The projection after filtering is obtained by applying inverse Fourier transform to the filtered projection data's spatial frequency representation.

The backprojection is performed by smearing back the projection data onto the reconstruction area. The pseudocode of the process is shown in the pseudocode 2.

Algorithm 3 Pseudo-code for backprojection algorithm.

Input: FilteredProjection(trans,rot,ω_t)
Output: ReconstructedData(x,y,t)

1: **for** jjj=1 to $trans\_num$ **do**
2: **for** kkk=1 to $trans\_num$ **do**
3: **for** iii=1 to rot_num **do**
4: $temp = jjj * cos(rot(iii)) + kkk * sin(rot(iii))$
5: $Result(jjj, kkk) = Result(jjj, kkk) + Input(rot(iii), temp)$
6: **end for**
7: **end for**
8: **end for**

The result of the backprojection process is the spectrum magnitude of the re-

constructed sound field. Temporal variation of the reconstructed sound field can be obtained by applying inverse Fourier transform. The pseudocode of the process is shown below.

Algorithm 4 Pseudo-code to obtain temporal variation of reconstructed sound field.

Input: Reconstructed Sound Field(ω_t)
Output: Reconstructed Sound Field(t)

1: **for** iii=1 to $reconstx$ **do**
2: **for** jjj=1 to $reconsty$ **do**
3: $Result(iii, jjj, t) = \mathcal{F}^{-1}(Input(iii, jjj, \omega_t))$
4: **end for**
5: **end for**

3.2 Numerical simulation of the method

A simulation of the measurement and reconstruction process was developed to evaluate the proposed sound field measurement method's performance. The sound field of the plane-wave and point source was used for the simulation. The sound source was simulated at a distance of 15 cm from the measurement plane, and the size of the measurement area was 36 mm × 36 mm.

The parallel scanning was simulated by calculating the line integral of the sound pressure on the measurement plane sequentially with the translation step of $2mm$. It is assumed that the sound field is axis-symmetric. Therefore, the same data was used for the projection from other angles. The rotation step was 10 degrees. The frequencies used for the simulation were 1000 Hz, 2000 Hz, 4000 Hz, 5000 Hz, 8000 Hz, and 16000 Hz. The filtered back-projection implementation for the reconstruction process uses a spatial ramp filter combined by a Butterworth low pass filter. The order of the Butterworth filter was $n = 5$ with the frequency cut-off of $\xi_c = 5$.

In the first simulation, I evaluated the effect of the translation error of the scanning process on the reconstruction result. Hence, we created data with no translation error and several data with scanning translation error. The range of the translation error were 10 %, 20 %, 30%, 40%, and 50% of translation step. The visualization of the reconstructed sound field for plane-wave sound source can be seen in Fig. 3.2.

Figure 3.2(a) shows the simulated sound field and Fig. 3.2(b) shows the reconstructed sound field using the FBP algorithm. We compared the two images and calculated the deviation. The result is shown in Fig. 3.2(c). We see that the reconstructed field yield by the FBP algorithm has a deviation from the original field. The error is small in a circular area around the center of the image and large at the reconstructed field's corners. Thus, becoming the effective reconstruction area yield by the FBP algorithm.

The visualization of the reconstructed sound for other measurement frequencies

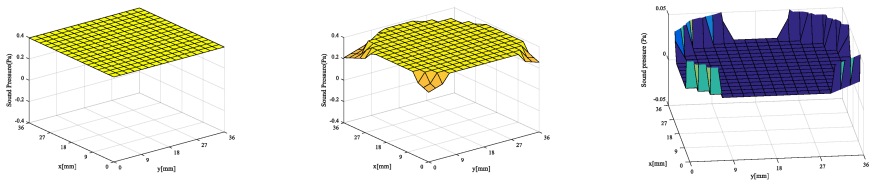

(a) Original (b) Reconstructed (c) Error

Figure 3.2: The original sound field, reconstructed sound field and the reconstruction error.

representing low, middle, and high-frequency range is shown in Fig. 3.3. The upper

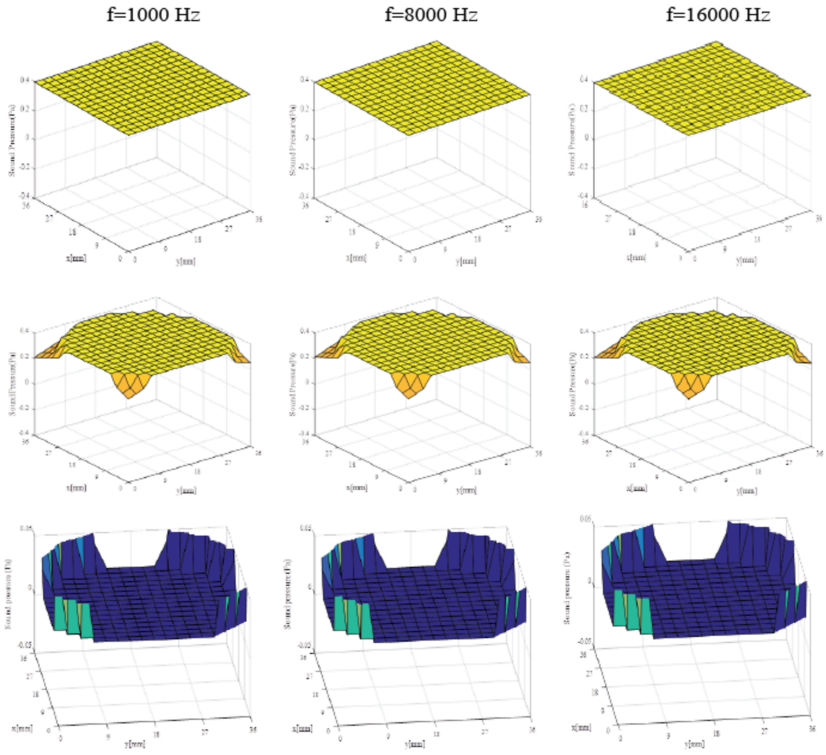

Figure 3.3: Simulation result for the plane-wave sound source.

figures show the original sound field for the corresponding frequency. The second image represents the reconstructed figures, and the deviation from the original sound field for the corresponding frequency are shown in the lower figure. From the image, we see that the reconstruction method worked well for the plane-wave sound source.

Afterward, we simulated the measurement for point source and reconstructed using the FBP algorithm. The simulation result is shown in Fig. 3.4. From the figures, we see that the FBP algorithm can be used to reconstruct point sound source. The reconstruction error is small for reconstruction of low frequency and slightly increases as frequency increases.

Furthermore, we evaluated the accuracy of the reconstruction result. For this

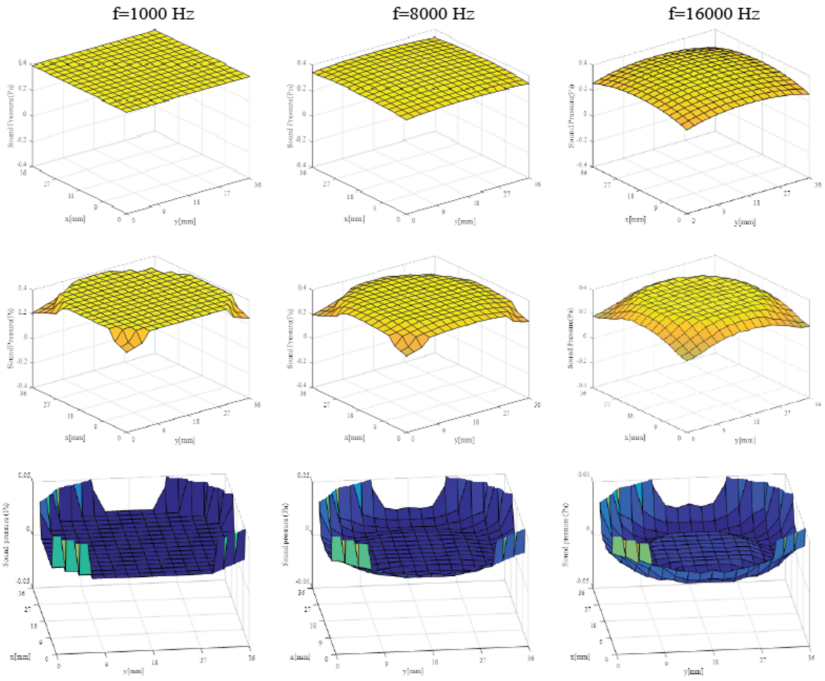

Figure 3.4: Simulation result for point sound source.

purpose, we simulated ten times and used the average value as the final result. Then, we compare the amplitude of the sound pressure of the original sound field and the reconstructed sound field for a different translation error. In the first simulation, we compare the sound pressure at the center of the reconstruction plane. The result is shown in Fig. 3.5.

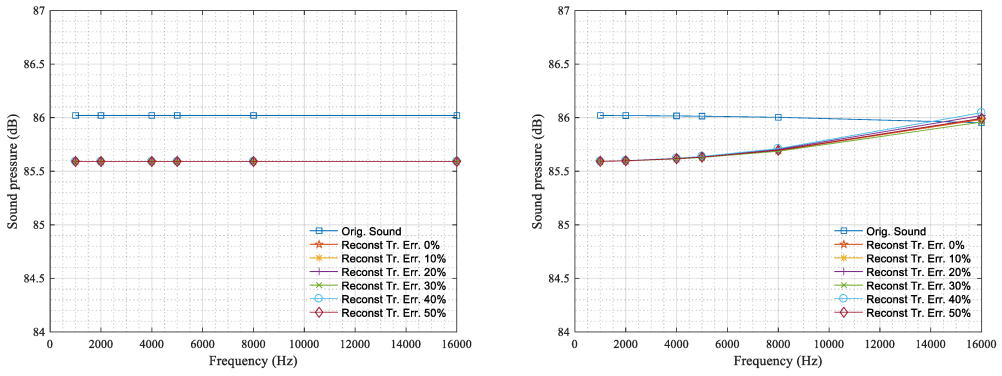

(a) Planewave (b) Point source

Figure 3.5: Performance of the reconstruction result at center point.

The x-axis represents frequency, and the y-axis expressed the sound pressure in the dB unit. At the center position, we found that the deviation between the original sound and the reconstructed sound pressure for the plane-wave is 0.43 dB for all measurement frequencies. We can see that the translation error did not

contribute to the reconstruction result. For the point source, the error was varies depending on the frequency. In the frequency range of 1000 Hz to 5000 Hz, the error is about 0.4 dB. However, the error is decreasing as the frequency increases. The translation error contributes to small errors only at the high-frequency range.

Then we evaluated the performance based on the average of the sound pressure. The result is shown in Fig. 3.6.

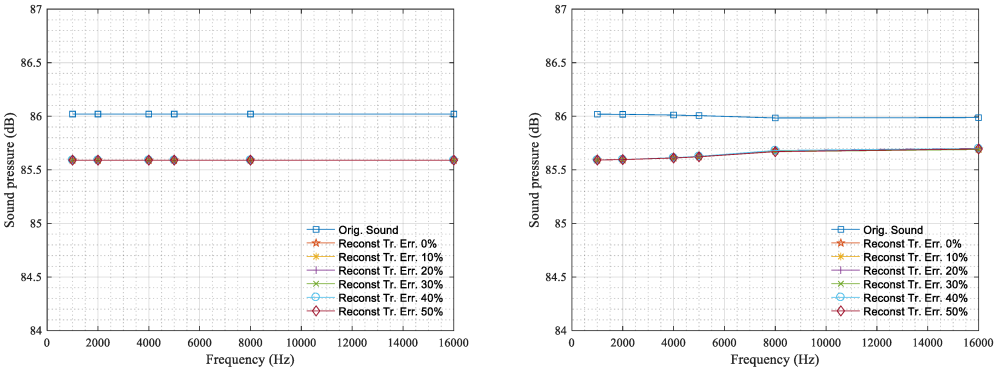

(a) Planewave (b) Point source

Figure 3.6: Performance of the reconstruction result from average value.

For plane-wave, the error is the same as before because the distribution of sound pressure is equal at every point. In the case of a point source, the average value error was 0.4 dB in the frequency range of 1000 Hz to 5000 Hz and then increased to 0.3 dB for frequencies 8000 Hz and 16000 Hz. This error indicates that there was a small sound pressure distribution difference produced by the reconstruction method.

Figure 3.7 shows the standard deviation of the reconstruction error for plane-wave and point source. The standard deviation value is expressed in the unit of Pascal. The result is obtained from the 10 times simulation with the random

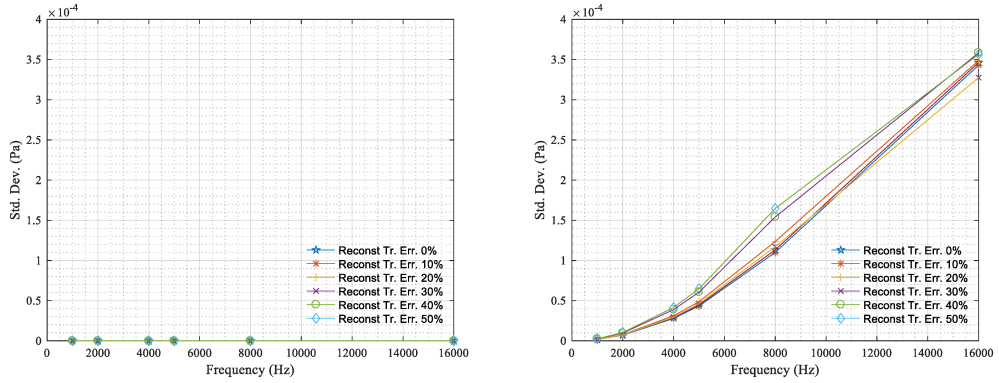

(a) Planewave (b) Point source

Figure 3.7: Standard deviation of the error in the simulation.

translation error for each error condition. It is seen that the translation error did not affect the reconstruction result for the plane-wave. For a point source, there is a small reconstruction error caused by the translation error.

3.3 Sound field measurement using a LDV

3.3.1 Measurement in free field

In the first experiment, we perform the reconstruction of the sound field in the free field environment. The experiments were conducted in the anechoic room of Waseda University. An LDV type Polytec OFV-505 was used as the interferometry system. The LDV was used to measure the sound field at a plane of 1 mm above the round table. The table was mounted on a rotating table to obtain the projection of the sound field from different angles. The LDV was mounted on a controlled traverse system with a single axis linear translation to perform parallel scanning. A loudspeaker positioned 20 cm above the table was used as a sound source to generate the plane's sound field.

A MEMS microphone type Knowles SPU0414HR5H-SB was mounted on the table to validate the sound pressure value. This microphone was positioned in the center of the rotating table as shown in Fig. 3.8.

For the tomography method's implementation to reconstruct the sound field, we performed scanning by sequentially translating the LDV along 200 mm with the translation step of 2 mm and the rotation step of 10 degrees. The LDV sensitivity setting was set to 1 (mm/s)/V, and its output was connected to the NI-PXI system

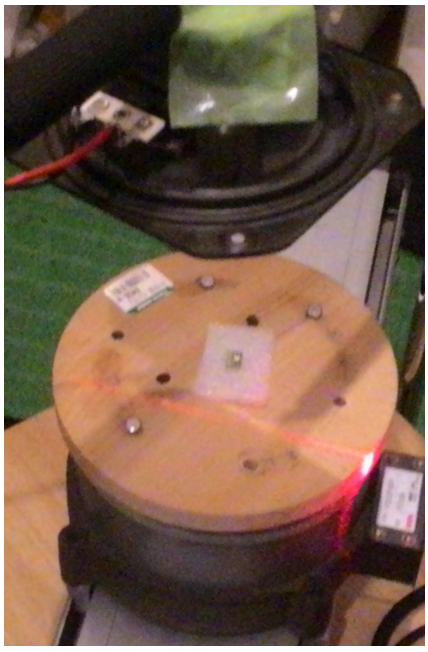

Figure 3.8: Configuration of sound field measurement at anechoic chamber using an LDV.

for recording the vibration velocity signal yield by the interferometry system. The synchronization between translation, rotation, and recording was performed by the National Instrument PXI system and LabView software program. The frequency sampling of the recording process was 48 kHz, with the total number of samples 1000. A windowed sound signal with a frequency of 1000 Hz and 2 ms was generated by the signal generator and reproduced by the loudspeaker.

The total number of scanning steps for each angle of projection is 100 steps. And, for each step, the total number of collected samples was 1000. Therefore, we have 100000 data samples for each projection angle. The rotation was conducted from 0 degrees to 170 degrees. Thus the total rotation step was 17 for one complete set of measurements. The total data collected for one complete measurement set is 1.7×10^6 samples.

A MATLAB code was developed for the sound field reconstruction from the measurement data. The output data yield by the LDV was in the Volt unit. Thus we converted this voltage value into the vibration velocity value based on the LDV sensitivity setting before processing the data.

The frequency of the sound used in this experiment was 1000 Hz. Figure 3.9 shows several images of reconstruction result in different time sequence. In the images, the x-axis and y-axis represents the position coordinates in the reconstruction plane, while the z-axis represents the amplitude of the sound pressure. The reconstruction plane's effective spatial resolution was 2 mm in the circular area with a radius of 100 mm. We can visualize the pressure distribution of the loudspeaker's sound from the initial condition where the was no sound. The amplitude of the sound pressure was then increased and then decreased.

To compare the accuracy of the sound amplitude measured using the optical method, we recorded the sound generated by the loudspeaker using the microphone. We plotted the signal measured using the microphone and optical method in one graph. The result is shown in Fig. 3.10.

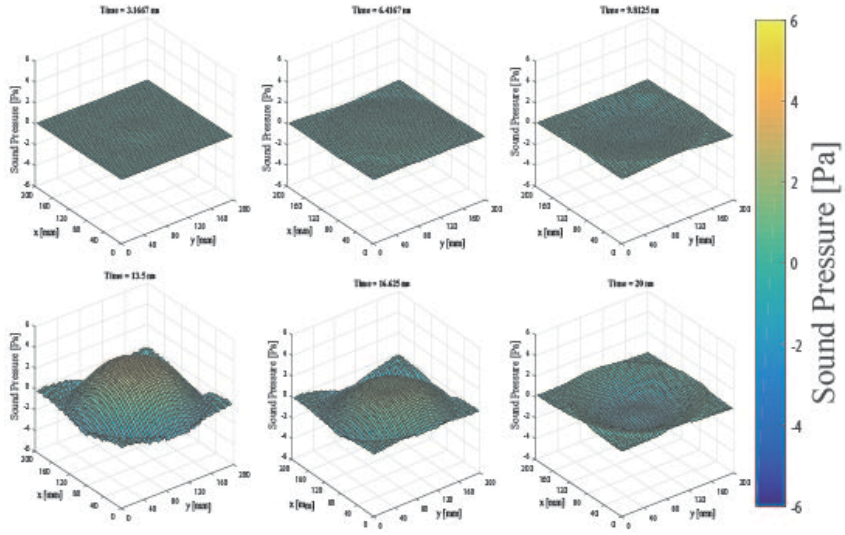

Figure 3.9: Reconstruction of sound field from measurement in the free field.

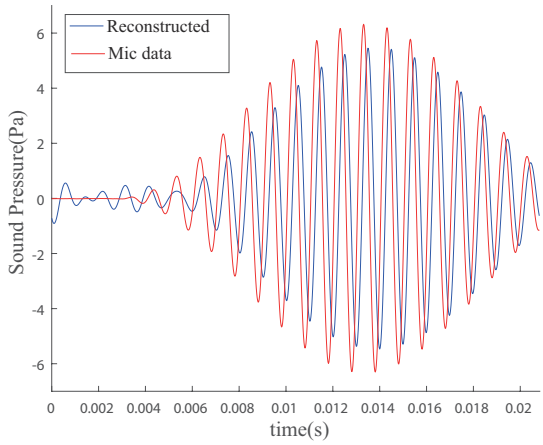

Figure 3.10: Comparison of the signal measured by using the microphone and optical method.

From the waveform comparison, we see that the sound generated by the loudspeaker can be reconstructed correctly with a small deviation. The phase of the sound measured by using the optical method has a lag of 0.2 ms compared with the microphone. The peak of the sound pressure measured by the microphone was 103.44 dB. The deviation between the microphone and optical method was found to be 1.49 dB. By using the optical method, we obtained the peak amplitude of the sound pressure was 101.95 dB. This evidence shows that the amplitude of the microphone's sound is greater than the optical method.

3.3.2 Measurement in pressure field

In the second experiment, we conducted measurement of sound field measurement inside a cylindrical tube. The cylindrical tube was made from acrylic glass with a thickness of 3.5 mm and 61.75 mm. On one side of the tube, we attach a loudspeaker as the sound source while an acrylic board sealed the other side of the tube with a thickness of 5.11 mm. To reduce the loudspeaker's body vibration and resonance to the tube, we strengthen the tube construction using bolts. Furthermore, we hang the tube using ropes, so there was no direct contact between the tube and the table. This configuration was used to avoid the propagation of the structural vibration from the loudspeaker to the optical components on the table. The LDV and mirror were arranged so that the laser beam can pass through the tube. The arrangement of the LDV, optical components and the tube is shown in Fig. 3.11.

Tomography method was implemented by translating the mirror sequentially along with the traverse system with a step of 2 mm with a distance of 18 mm from the tube's center position. Since the measured sound field was assumed to be axis-symmetric, we only performed parallel scanning only from one angle and half the tube's size. The projection data for other angles were assumed to be equal. Therefore, the total measurement area was 36×36 mm. On the edge of the tube, the parallel scanning was difficult because the beam was dispersed, and only a small

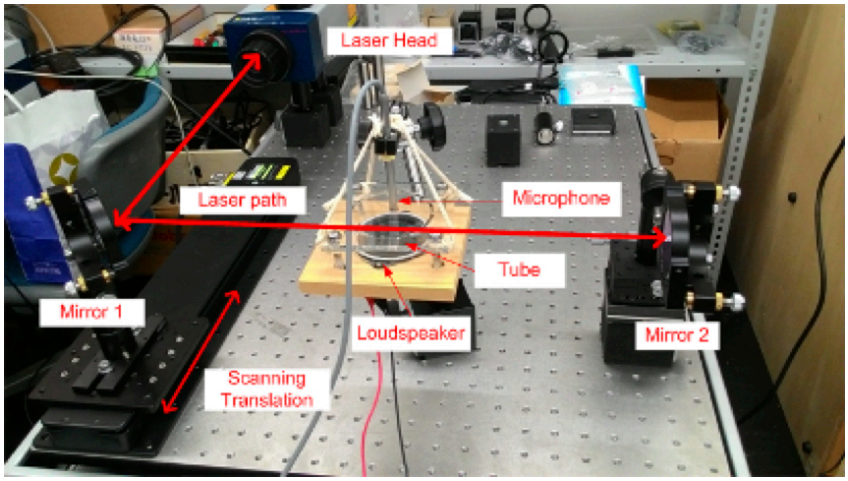

Figure 3.11: Configuration for measurement of sound field inside a tube.

amount of the light was reflected. This condition made the SNR of the interference became low. The light also refracted as we moved further from the center of the tube. To compensate for this, we adjust the panning of mirror 2.

For validation of the optical sound measurement method, we flush mounted a microphone type B&K 4939 by making a hole in the center of the tube enclosure. The microphone was connected to a preamplifier B&K 2692 and a digital voltmeter. A National Instrument data acquisition system was used to generate the signal and recording the voltage output from the LDV. The instrument is also used to perform the control of the traverse system movement. The synchronization of the process was performed by developing software using LabVIEW programming language. The recording process's sampling rate was 50 kHz, and the length of the generated signal was 1.5 seconds. The measurement data were saved in the comma-separated values (CSV) format.

For the experiment, we generated the sound at the frequency of 1000 Hz. The constants for calculation of the acousto-optic were as follow: static pressure value $p_0 = 101325Pa$, air refractive index $n_0 = 1.000279$, and air specific heat index $\gamma = 1.41$.

The reconstructed sound field from the measurement for several time sequences are shown in Fig. 3.12. From the visualization, we can see the distribution of the sound pressure on the reconstruction plane. The shape of sound pressure distribution on the reconstruction plane is concave and convex representing the rarefaction and compression state of the sound propagation. And because the shape of the tube enclosure is flat, the shape of the sound field is flat at some point. This represents the reflected sound by a flat surface.

To evaluate the reconstructed sound field's accuracy, we compare the magnitude of the sound pressure measured by the optical method and microphone. I selected the point at the center of the reconstruction plane, which is equal to the microphone placement position. In this experiment, we found the magnitude of the sound pressure at the center of the tube measured by the optical method was 131.59

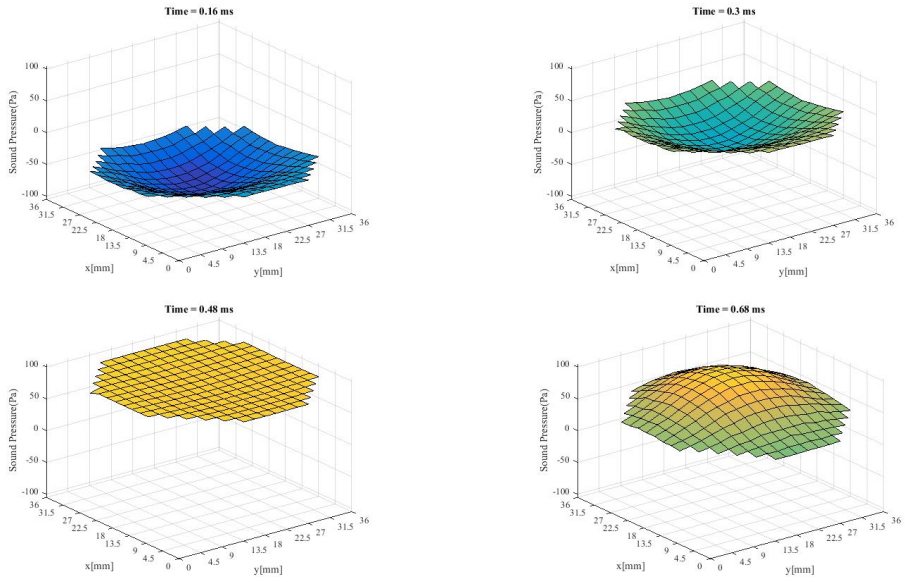

Figure 3.12: Sound field reconstruction result.

dB. Meanwhile, the sound pressure measured by the microphone was 130.73 dB. From this result, we found that the difference between the optical method and the microphone was 0.86 dB. The vibration of the optical system that includes in the measurement result possibly caused this difference.

3.4 Conclusion

The acousto-optic effect principle describes that the phase shift of the light corresponds to the line integral of sound pressure along the optical path. The principle has been successfully implemented for sound field measurement by applying a tomography reconstruction method. The method comprises two consecutive steps: parallel scanning and reconstruction process. Parallel scanning processes from multiple angles are performed to obtain the projection of the sound field. The reconstruction step is used to restore the measured sound field into the reconstruction plane. In this study, filtered back-projection was implemented for the reconstruction.

A numerical simulation of the measurement method was developed to characterize the reconstruction performance. A sound field of plane wave and point sound source was scanned and successfully reconstructed. The maximum reconstruction error for the plane wave was 0.43 dB, while the point source's maximum reconstruction error was 0.4 dB.

We demonstrated the implementation of the proposed method in the experiments. A laser Doppler vibrometer was used to perform parallel scanning through a sound field generated by a loudspeaker with a translation step of 2 mm and a rotation step of 10 degrees. The microphone was used to validate the sound pressure level measured using the optical method.

The first experiment was performed in the free field environment. The sound at a distance of 20 cm from a loudspeaker and a pressure level of 103.44 dB was successfully reconstructed. We found that the discrepancy between the optical method and microphone was 1.49 dB.

Implementation of the optical method for measuring sound in closed tubes was carried out in the second experiment. The laser beam was passed through the tube, and the projection was assumed to be axis-symmetric. A sound pressure inside the tube with a pressure level of 130.73 dB can be measured using the optical method with a measurement error of 0.86dB.

Chapter 4

Characterization of PPSI system

4.1 Introduction

The PPSI's configuration utilizes a lens to create a measurement area of the system. The lens is used to expand the laser beam size from the source to the interferometry system's reference lens, and we can adjust the optical zoom by moving of lens. The earliest PPSI system used a reference and mirror lens with a diameter of 100 mm. Thus, the maximum effective measurement area of the PPSI system was 100 mm in diameter.

Recently, the measurement area of the PPSI system has been improved. The maximum effective measurement area of the PPSI system has been increased from 100 mm to 200 mm in diameter. The improvement has been made by replacing the reference and mirror with a new lens with a diameter of 200 mm, as seen in Fig. 4.1. Therefore, the maximum effective measurement area becomes 200 mm in diameter.

The optical distortion of the lens caused the light to be aberrated. A straight line image can be seen as curved inward or outward due to optical distortion. In the PPSI system, the reference and mirror lens is an essential part of the interferometry

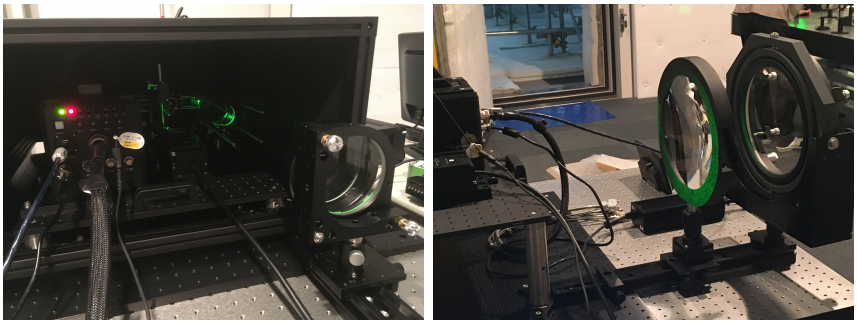

(a) Old PPSI system (b) New PPSI system

Figure 4.1: Optical part of old PPSI system and new PPSI system.

system. The lens must be able to pass the laser beam perfectly. However, the distortion-free lens is difficult to find. Lens imperfections cause light interference pattern to be aberrated. Thus, producing pattern error in the interferogram that is captured by the PPSI' camera. An investigation of the new PPSI's optical system is required to find the optical distortion type in the new PPSI system.

Background noise was determined from PPSI's measurement area when there was no sound generated by the sound source. Hence, the measured sound by the PPSI was pure noise coming from the measurement environment.

The simplest method to analyze optical distortion is using calibration plate [67, 68]. The calibration plate is a transparent glass with a pattern such as parallel lines or checkerboard. Ideally, the shadow of the pattern caused by the light passing the plate will match the original pattern. However, the shadow of the pattern will change due to optical distortion. The type of distortion can be analyzed from the image pattern.

4.2 Acoustical background noise measurement

4.2.1 Noise assesment using power spectral density

The PPSI system comprises a laser, optical system, and high-speed camera. The system measures the phase-shift of the light that is proportional to the variation of sound. The PPSI system's performance can be characterized by its basic function that is measuring the phase of the light caused by the sound. This can be done by utilizing the PPSI system to measure sound background noise in the experiment room. By using this method, we can determine if any other frequency component includes in the measurement result.

The characteristic of background noise is the random broadband signal. Hence, we can characterize the background noise from power spectral density (PSD) measurement, which shows the power of frequency components in the signal [69–71].

The total energy of a signal $x(t)$ is an integral of instantaneous signal power which is described as

$$E = \int_{-\infty}^{\infty} x^2(t)dt. \tag{4.1}$$

While signal power is defined as the total energy for T of a periodic signal, and the value is given by

$$P = \frac{1}{T}\int_{-\frac{T}{2}}^{\frac{T}{2}} x^2(t)dt. \tag{4.2}$$

According to the Parseval's theorem,

$$\int_{-\frac{T}{2}}^{\frac{T}{2}} \mid x(t) \mid^2 dt = \int_{-\infty}^{\infty} \mid \mathcal{F}(x(t)) \mid^2 df, \tag{4.3}$$

where $\mathcal{F}(x(t)$ is the Fourier transform of the signal. Dividing the equation 4.3 above by T, we will obtain the average signal power

$$\frac{1}{T}\int_{-\frac{T}{2}}^{\frac{T}{2}} \mid x(t) \mid^2 dt = \frac{1}{T}\int_{-\infty}^{\infty} \mid \mathcal{F}(x(t)) \mid^2 df. \tag{4.4}$$

The PSD is defined by taking the limit of T on the right-hand side of equation 4.4 approaches infinity,

$$PSD = \lim_{T\to\infty}\left[\frac{|\ \mathcal{F}(x(t))\ |^2}{T}\right]. \tag{4.5}$$

Therefore, the PSD measures the average signal power as a function of frequency.

A Fourier transform of a discrete signal ($x[n] = x_0, x_1, \ldots, x[N-1]$) is calculated by using the following equation,

$$X(\omega) = \sum_{n=0}^{N-1} x[n]e^{(-j\omega nT)}. \tag{4.6}$$

where N is the number of samples, T is the sampling period. The spectral resolution of the signal in the Nyquist band is calculated as ω_s/N. Based on the Eq. 4.5, we can calculate the PSD of the discrete signal using the Fourier transform. This is called periodogram function, and is defined by the following equation,

$$PSD(\omega) = \frac{1}{N}\ |\ X(\omega)\ |^2\ . \tag{4.7}$$

4.2.2 Experiment configuration

The instruments configuration for measurement of the acoustic background noise of the PPSI instrument is shown in Fig. 4.2. In the new PPSI system, the user has an option to adjust the optical zoom system to determine the effective measurement area. However, due to the optical system's noise, the manufacturer limits the effective measurement area of the new PPSI system to 150 mm, and the predefined measurement size is 70 mm, 100 mm, and 150 mm. The measurement area's adjustment is made by changing the position of the zooming lens according to each zooming setting. The PPSI system is also equipped with fans that are used to cool down the high-speed camera system. Therefore, we also consider the fans' effect on the PPSI measurement result by analyzing the background noise while the fan is running and stop condition. A push-button switch was installed in the PPSI system to control the fan. When we push the button, the fan is turned off, and the fan's operation is automatically resumed after 15 seconds.

PPSI settings for the measurement of background noise were as follow. The recording frame rate was set to 50000 fps, and the number of samples for one

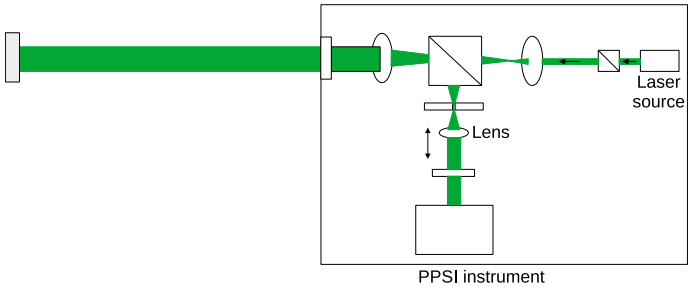

Figure 4.2: PPSI system with 200 mm lens size.

measurement was 50000 samples. The size of the image was 256×256 pixels. A HEFS algorithm was used to extract the spatio-temporal phase shift of the light corresponding to the sound. The signal for the calculation of the PSD was obtained from the phase signal at the center of the measurement area. The measurement was repeated three times for each fan condition and each measurement area size. The final PSD values were calculated from the average of the phase values obtained from each measurement.

4.2.3 Result of background noise measurement

In this experiment, we have two measurement condition, which is a fan on and fan off. And for each measurement condition, we characterize each predefined measurement area. Therefore, we have six background noise measurement data in total.

Figure 4.3 shows the PSD result for the measurement area of 70 mm. Since the quantity measured by the PPSI is the phase shift of the light correspond to the sound pressure, then we represent the measured signal in the unit of a radian and the unit of PSD in dB(rad)/Hz. The power of the signal as a function of frequency can be seen from the graph. The measured signal's PSD when the camera fan is running during the measurement process is shown in the red line. We can see that the power of the signal is less than -90 dB across the frequencies. However, we found a dip around 3000 Hz and 3400 Hz includes in the measurement result.

The green line shows the PSD result when the fan is turned off during the measurement process. The average of the signal power is about -85 dB(rad)/Hz. This value is slightly higher than the first condition when the fan is running. This small discrepancy is caused by the variation of the phase result in each measurement result. Interestingly, we found a dip in the frequency of 3000 Hz and 3400 Hz disappear from the graph. This finding indicates that the rotation of the camera-fan generated a sound at those two frequencies.

Figure 4.4 shows the PSD result for the measurement area of 100 mm. When

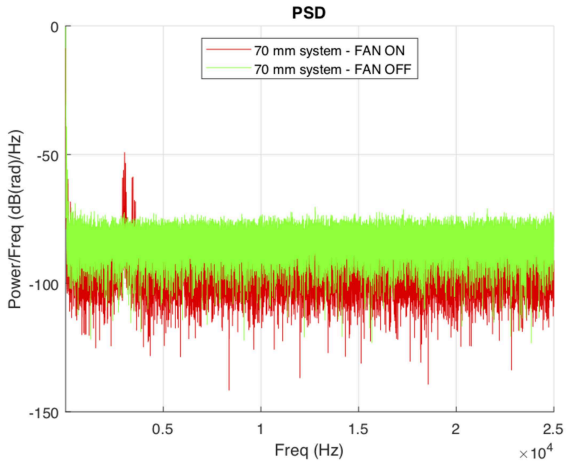

Figure 4.3: Result of measurement area of 70 mm.

the camera fan was running and stopped, the PSD values are shown in the red and green line, respectively. From the graph, we obtained that the average PSD values are about -90 dB(rad)/Hz when the fan is running and -95 dB(rad)/Hz when the fan is turned off. Again, we found a dip at a frequency of around 3000 Hz and 3500 Hz. We also found another dip at a frequency around 6000 Hz, which is the harmonic of the first dip frequency component. This finding also shows that the camera fan sound has a significant contribution to the PPSI measurement result.

Figure 4.5 shows the PSD result for measurement area of 150 mm. The average PSD values when the camera fan is running and stopped have shown an almost equal value of -95 dB(rad)/Hz. But the dip around frequencies of 3000 Hz and 3500 Hz occurs. Also, we found the dip at frequencies of 6000 Hz 6600 Hz which are the harmonics frequency components. To summarize the analysis, we combined all the measurement results into a single image and the result is shown in Fig. 4.6.

From the image, we see that the overall background noise performance of the new PPSI system is less than -80 dB(rad)/Hz. Variation in the results shown in Fig. 4.6 shows the difference in the measurement results obtained from one measurement with another. This difference in results is due to differences in laser alignment between one measurement and other measurements. But, the measured background noise level is small and has no significant contribution to the measurement result. However, our finding confirms that the camera fan generates sound at a frequency of around 3000 Hz. The fan's noise level is high, affecting the measurement result if we use PPSI to measure sound around that frequency.

4.3 Optical distortion measurement

4.3.1 Types of optical distortion

A lens is used to collect or scatter light rays. There are two types of lenses, namely convex lenses and concave lenses. The convex lens is used to collect light, while the

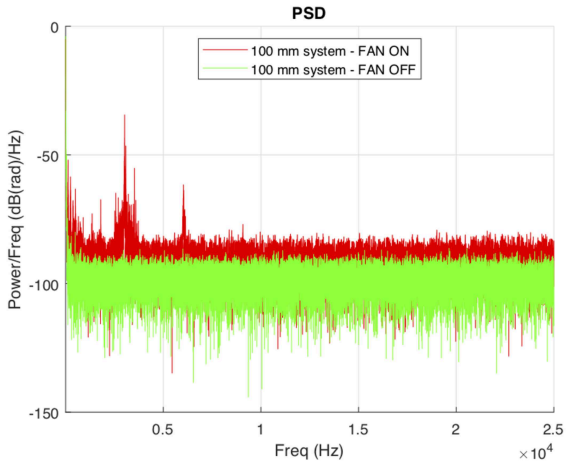

Figure 4.4: Result of measurement area of 100 mm.

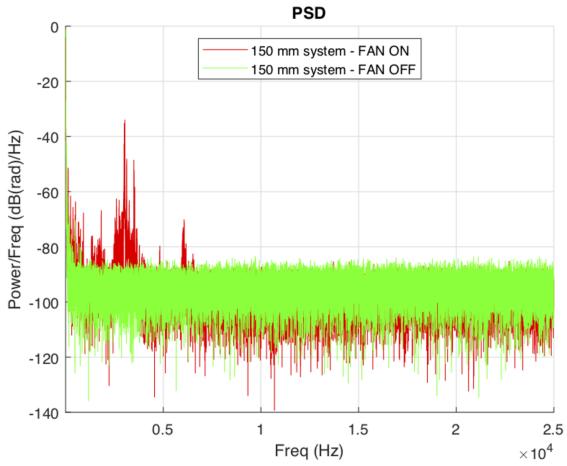

Figure 4.5: Result of measurement area of 150 mm.

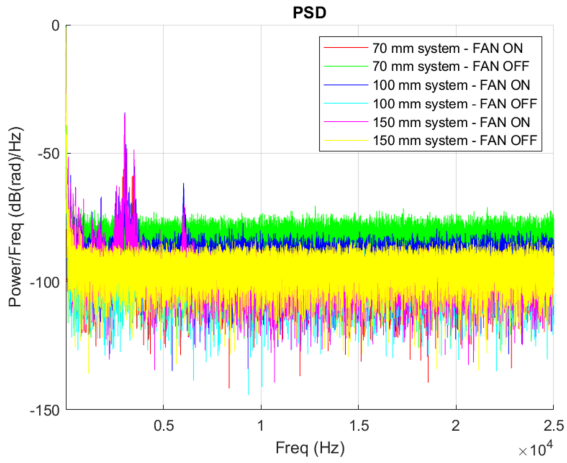

Figure 4.6: Background noise performance of the new PPSI system.

concave lens is used to scatter light rays. In a camera system, the lens is used to project an image onto the sensor [72, 73].

The imperfection of the lens manufacturing leads to image distortion. In general, image distortion by lens can be formulated using the Brown model as [74, 75]:

$$\begin{aligned} x_u &= (x_d - x_0)(1 + k_1 r_d^2 + k_2 r_d^4 + k_3 r_d^6 + \cdots) + (1 + p_3 r_d^2 + \cdots) \\ &\quad \{p_1 [r_d^2 + 2(x_d - x_0)^2] + 2p_2 (x_d - x_0)(y_d - y_0)\}, \\ y_u &= (y_d - y_0)(1 + k_1 r_d^2 + k_2 r_d^4 + k_3 r_d^6 + \cdots) + (1 + p_3 r_d^2 + \cdots) \\ &\quad \{p_1 [r_d^2 + 2(y_d - y_0)^2] + 2p_2 (x_d - x_0)(y_d - y_0)\}, \end{aligned} \tag{4.8}$$

where (x_0, y_0), (x_u, y_u), and (x_d, y_d) represent the center of the image, coordinate of undistorted point, and distorted point in an image, respectively. Variable $r_d = \sqrt{(x_d - x_0)^2 + (y_d - y_0)^2}$ is the distance of the distorted point to the center of the image. Parameter k_i represents the radial distortion and p_i represents decentering coefficients.

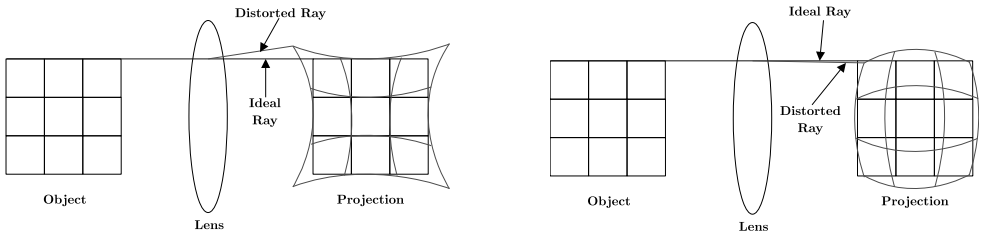

(a) Pincushion distortion (b) Barrel distortion

Figure 4.7: Types of optical distortion.

From the Brown model, we can derive two kinds of radial distortion, namely Barrel distortion and pincushion distortion [76,77]. In the pincushion distortion, the image became thin in the center, and magnification increases as a function of spatial distance from the center of the lens [78, 79]. In opposite, there is Barrel distortion where the magnification decreases as a function of distance from the center of the lens [80, 81]. This effect occurs because the ray is not hit at the correct focal plane on the image. The comparison between pincushion and Barrel distortion can be seen in Fig. 4.7.
Optical distortion can also be expressed using another model as follow [82]

$$\frac{(y' - y)}{y} = ah^2 + bh^4, \tag{4.9}$$

where y is the height of the object image, y' is the height of the projected image. The left-hand side of the Eq. 4.9 is called relative distortion $\frac{(y'-y)}{y}$. Using the model, the pincushion distortion is expressed as positive value of variable a. In contrast, the negative value of a expressed Barrel distortion.

4.3.2 Experiment configuration

The determine the optical distortion occur within the PPSI system, we employed an optical calibrator plate made by Shibuya Optical Co., Ltd. The model is CBC01–150T which has checkerboard pattern as shown in Fig. 4.8 The dimension of the plate is 160 mm × 160 mm with the thickness of 3 mm. The size of the each square in the grid is 5 mm × 5 mm.

The calibrator is positioned in the light path between the mirror and the PPSI system's reference plane as shown in Fig. 4.9(a). A stand table is used to mount and adjust the height of the calibrator to make the laser beam pass through the calibrator as shown in Fig. 4.9(b). With this configuration, some portion of the light was blocked by the plate, and the other portion of light can pass the plate and be directed to the mirror. The mirror will reflect the passing light to the reference lens to create the interference pattern.

The measurement was started by adjustment of the laser alignment until the fringe pattern is developed. Afterward, the PPSI is ready to record the interferogram. For the experiment, the recording sample rate setting of PPSI is 6000 fps.

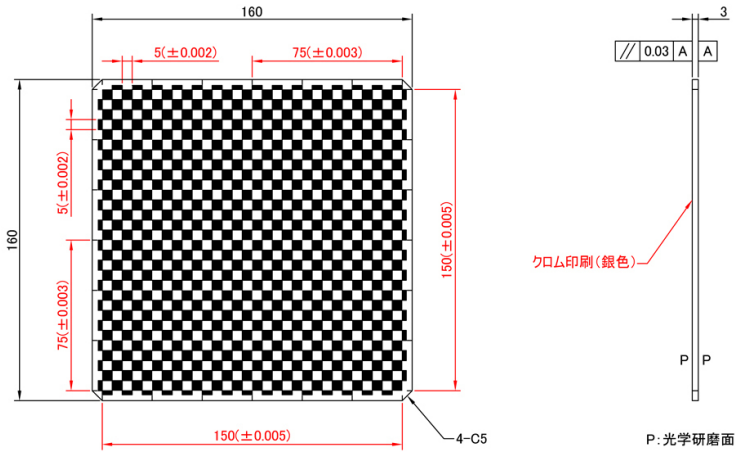

Figure 4.8: Calibrator plate.

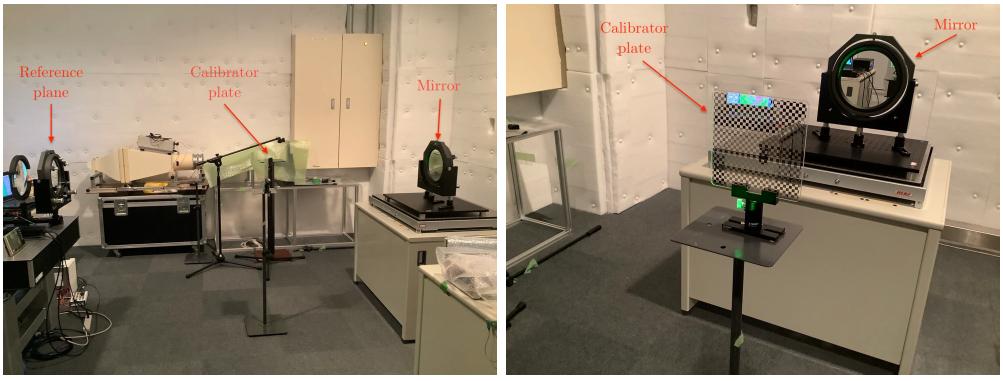

(a) Calibrator plate position (b) Calibrator mounting

Figure 4.9: Optical distortion measurement using a calibrator plate.

The size of the recorded image is 1024 × 1024 pixels. The number of recorded samples is 100. However, for the analysis, we only used one image frame.

A single image recorded by PPSI contains four phase-shifted images corresponding to each phase retardation of 0, $\pi/2$, π, and $3\pi/2$. The arrangement of phase data in the image is shown in Fig. 4.10. For the analysis of optical distortion, we used the actual image without extracting the phase shift. A single phase retardation angle was extracted from the original image. This was done by grabbing pixel values consecutively with a one-pixel interval in the row and the column direction of the image. The function for extraction is shown in pseudocode 5.

4.3.3 Result and discussion

For the analysis, we extracted image intensity correspond to phase retardation of 0 degrees from the interferogram. The original image intensity recorded by the PPSI is shown in Fig. 4.11(a) and the resulted image after processed by the edge detector algorithm is shown in Fig. 4.11(b). The processed image has the size of 512 × 512 pixels, which is a half resolution of the original recorded image by PPSI.

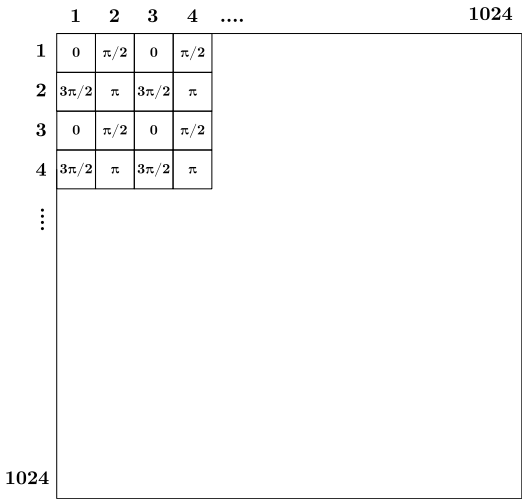

Figure 4.10: Layout of phase data in the image.

Algorithm 5 Pseudo-code for extracting single phase-retardation image intensity

Input: raw pixel intensity image
Output: single phase-retardation pixel intensity image

Initialize $s \leftarrow 1$
Initialize $p \leftarrow 1$
for $i \leftarrow 1$ to n-rows by 2 **do**
    for $i \leftarrow 1$ to n-cols by 2 **do**
        Output(s,p) = Input(i,j)
        $s \leftarrow s + 1$
    end for
    $p \leftarrow p + 1$
end for

The reduction of the size is the result of the extraction process.

The measurement area of PPSI appears as a circle object. Inside the measurement area of PPSI, we can see the white square pattern. This pattern is formed by the light that passes through the calibrator plate so that interference can occur. While the gray image represents the light that is blocked by the calibration plate pattern. On the right part of the image, the square shape can be seen clearly. But, on the left part of the image, the square pattern is difficult to see. The square pattern looks like a dot pattern. This can be caused by the calibration plate position that is not perfectly perpendicular to the light beam. The distribution of light captured by the camera is also uneven, where the area around the center point of the image has a higher light intensity, thereby reducing image contrast.

The type of optical distortion was evaluated based on the image of the calibrator pattern. Image processing was carried out to separate the calibration plate pattern image from the background image to emphasize the pattern. This was achieved by applying an edge detector to obtain the square pattern in the image. The flowchart

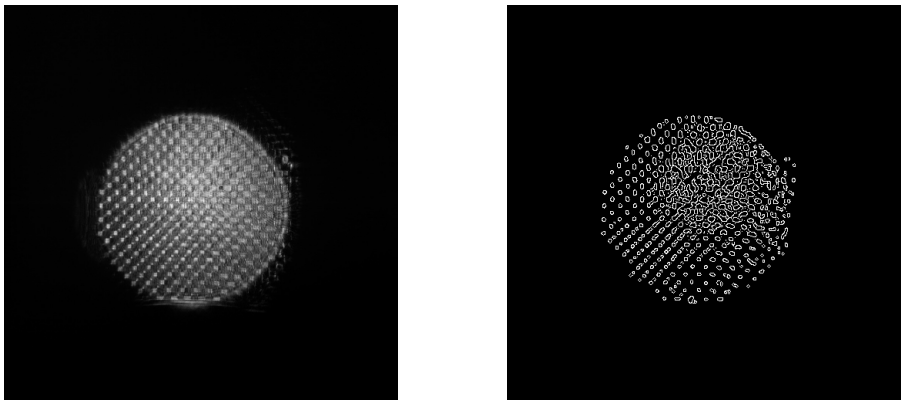

(a) Extracted plate image (b) Processed image with edge detector

Figure 4.11: The extracted calibration plate image from the interferogram and the result of processing to obtain the pattern for analysis.

of the processing steps is shown in Fig. 4.12.

A MATLAB code was developed to process the image based on the described flowchart. The extracted image is containing information about pixel intensity with a dynamic range of 12 bits. Therefore, we need to convert it to grayscale for further processing. This process can be implemented using MATLAB's *mat2gray* function. The background image can be removed by emphasizing the white area in the image. To do this, we can implement the *binarize* function provided by MATLAB. Finally, a Canny edge detector was implemented to detect the square pattern and suppress noise in the image. The result of the process is shown in Fig. 4.11(b).

We see from the result that the detected shape is not perfectly in square shape. The square shape is difficult to be observed on the upper right part of the image. This condition is due to the lack of contrast between the grid pattern and the background image. Hence, the edge detector is not working effectively. The edge detector can detect the pattern on the left part of the image because the contrast is relatively high.

To analyze the distortion, we observed the alignment of the dots in the grid by using a line. We edited the image 4.11(b) using the LibreOffice Drawing application by attaching a red grid line to the image as shown in Fig. 4.13.

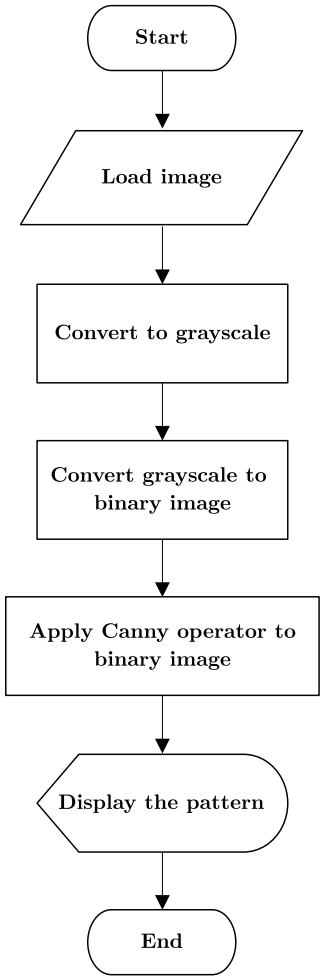

Figure 4.12: Flowchart of image processing to obtain the pattern from the calibration plate image.

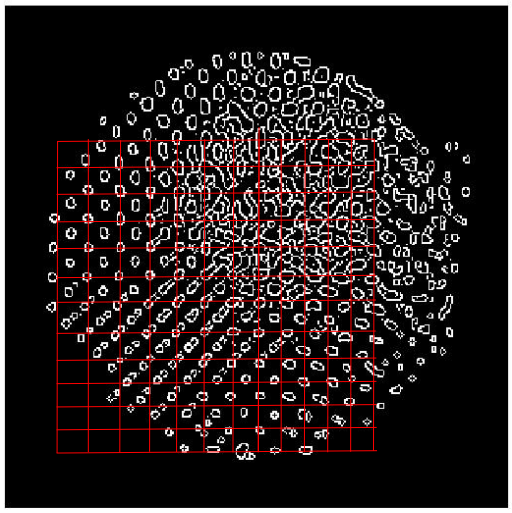

Figure 4.13: Image analysis for optical distortion.

It is seen in Fig. 4.13 that some square patterns are not hitting the crossing line of the grid. This evidence shows that optical distortion occurs in the new PPSI's optical system. The square pattern deviation is small on the left part of the image but looks significant on the lower part of the image. Some square patterns appear in an outward direction relative to the grid line. This type of optical distortion is the characteristic of pincushion distortion.

The level of the optical distortion can be determined using the following formula [83]:

$$dist(\%) = \mid \frac{T_{imag} - A_{imag}}{A_{imag}} \mid \times 100\%, \tag{4.10}$$

where T_{imag} represents the distance of the target position. This is the coordinate of the undistorted image relative to the center of the image. Meanwhile, the variable A_{imag} represents the position of the distorted image relative to the center.

Based on the visual inspection results, the largest deviation of the pattern from its ideal position occurs on the lower part of the image. The deviation is increasing as the function of distance from the center of the image. The regularity of the pattern also shows the change to be spanned than the ideal image. From the calculation, the largest distance of the distorted image relative to the center is 136.9379, while the ideal position relative to the center is 124.0363. Therefore, we can estimate that the maximum distortion level is 9.42%.

4.4 Conclusion

In measuring sound using optical methods, optical components have the main contribution that affects the results. This applies to PPSI which is used as a sound measurement instrument. The characteristics of the PPSI instrument need to be known before using it for sound measurement. In this chapter, we evaluated the background noise and optical distortion in the measurement system.

The evaluation of background noise of phase measurement was performed from the measurement of power spectral density. Two measurement conditions were evaluated, when the PPSI's camera was turned on and turned off. It was found that the noise at frequency 3000 Hz includes in the measurement result when the camera was turned on during the interferogram recording process. Nevertheless, the noise disappeared when the camera fan was turned off during the recording process. The background noise was -80 dB(rad)/Hz when the camera was turned off.

A calibrator plate with checkerboard pattern was used to analyze the optical distortion. The pattern was positioned in the middle between the mirror and reference plane of the PPSI instrument. The recorded pattern by the camera was analyzed to determine the optical distortion. An image processing technique was employed to emphasize the pattern for evaluation. We revealed using a visual observation that pincushion optical distortion existed in the optical system of PPSI with the maximum distortion level of 9.42 %.

Chapter 5

MEMS microphone calibration using PPSI

The MEMS type microphones differ from the conventional condenser microphones. The most obvious difference is in the size and shape of the microphone. The traditional condenser microphone has a standardized size and standard diaphragm geometry shape. In contrast, there is no standardization of MEMS microphone geometry at present. And, the most significant difference is the size. The size of the MEMS microphone is much smaller than a regular microphone.

Sensitivity of the microphone represents the output voltage for the applied sound pressure. To determine the sensitivity of a microphone, several microphone methods are available in the standard. In these methods, the sound exposed to the diaphragm is estimated from the acoustic propagation model derived from the geometry of the conventional condenser microphone. Therefore, the sound field estimation results are inaccurate when applied to the MEMS microphone. It is also impractical to measure diaphragm geometry for the calibration.

This chapter presents the PPSI instrument's application for measuring the sound field on the surface of the MEMS microphone when a sound source is applied. The measured sound and voltage output from the MEMS microphone is then used to determine the microphone's sensitivity under test. The validation of the result by the implementation of the substitution calibration method is also described.

5.1 Introduction

The microphone calibration methods are documented in the IEC 61094 series standard [84]. The IEC 61094-2 and IEC 61094-3 explain the reciprocity calibration method in the pressure and free field environments. The calibration procedure and sensitivity calculation have been presented in Chapter 2. A reciprocal microphone, which acts as a receiver and transmitter, is required to implement the reciprocity method. The microphone's sensitivity is determined from the measurement of electrical transfer impedance, and calculation of acoustical transfer impedance [36, 85]. To calculate the acoustical impedance, detailed information about the microphone geometry such as microphone front cavity depth and an environmental condition

during the calibration process is required [86].

A less precise microphone calibration method is the substitution method described in the IEC 61094-5 [87]. A calibrated microphone is required to be used as the reference microphone. A reference microphone is then substituted by the microphone under test by assuming that the sound field applied to both microphones is equal. To achieve this condition, it is required that both microphones have the same geometry. In this method, the microphone's sensitivity under test is determined from the sensitivity of the reference microphone.

Recently, conventional condenser microphone has begun to be replaced by using MEMS type condenser microphones. Modern instruments such as communication devices, multimedia system, acoustic imaging, energy harvesting system, and measurement instruments use MEMS microphone as the acoustical transducer [6,88–91]. Current MEMS microphone technology has wide operating range, better SNR, high sensitivity, and smaller packaging [92–94]. The sensitivity of the MEMS microphone is an important information parameter to build reliable devices. For example, a far-field application such as a smart speaker requires a high-sensitivity microphone to pick up sound from a distance. In contrast, a high-sensitivity microphone is not suitable for near-field devices such as cellular devices because the signal will be clipped and produces a distortion in the output signal.

Nevertheless, the standard calibration method of the MEMS microphone has not been established yet. The difference in the geometry and the size between the MEMS and conventional microphone makes the currently available microphone calibration standard is not applicable for MEMS. Therefore, a novel method for calibrating a microphone is needed.

Although MEMS microphones have been widely used in various types of instruments, only a few developments of MEMS microphone calibration methods have been done. Wagner *et al.* implemented the pressure reciprocity method for MEMS microphone calibration according to IEC 61094-2. As the MEMS microphone is not reciprocal, the MEMS is used only as of the receiver. To adapt the reciprocity calibration apparatus, an adapter for MEMS microphone mounting was developed. The front cavity depth for calculation of acoustical transfer impedance is estimated from an iterative fitting method [95]. Prato *et al.* proposed implementation of microphone comparison method in the pressure field according to the IEC 61094-5 [96]. An adapter was developed so that the MEMS microphone has the same geometry as the reference microphone. The reference microphone and the MEMS microphone are interchanged at the measurement point so both microphones experienced the same sound field.

The optical has been used in the vibration field to calibrate the accelerometer [97]. Recently, the application of the optical method for microphone calibration has gained attention. Laser interferometry has been used to determine the condenser microphone's sensitivity by measuring the diaphragm vibration [98]. Another solution is the direct realization of microphone sensitivity definition by measuring sound pressure applied to the microphone.

Based on the literature study, there are two available methods for realizing sound pressure measurement using an optical method. The first method is based

on the relation between sound pressure and particle velocity. The method estimates the sound pressure from the measurement of particle velocity that can be measured using a laser Doppler shift technique [10, 99] or photon correlation spectroscopy (PCS) [100, 101]. The application PCS for calibration of the MEMS microphone has been reported in the literature [102]. The second method is based on the acousto-optic effect that describes the phase shift of the light caused by the sound pressure. The realization of acousto-optic based sound pressure measurement using an LDV has been proposed [21].

In this research, the MEMS microphone's sensitivity is determined from the sound field and output voltage measurement. Sound field measurement is realized based on the acousto-optic effect employing a PPSI instrument. The tomography technique using PPSI is implemented to obtain the sound field's projection on the area near the microphone surface. The advantage of PPSI for the tomography technique is that it does not require a parallel scanning process to measure the line integral of the sound pressure. A filtered back-projection technique was implemented to reconstruct the sound field from its projection. The output voltage was measured for given sound pressure. Therefore, the sensitivity can be calculated directly from the pressure and voltage value as in the definition. In this experiment, I used Knowles MEMS SPU0414HR5H-SB breakout as the microphone under test (DUT). The DUT was configured to have a gain of 20 dB with a power supply of 1.8 Volt. I mounted this DUT on the self-made MEMS adapter.

5.2 Calibration procedures

The proposed calibration method comprises three main processes, which are: initialization step, phase measurement step, and data processing step. The functions in each step are described as follows.

5.2.1 Initialization step

The initialization step is used to determine the voltage setting to generate reference sound pressure. The instrument configuration for the initialization step is shown in Fig. 5.1. The calibration was performed in a room where the environmental noise effect is minimized as low as possible. For room treatment, I installed an absorbing material on the room walls to reduce the reflection of the sound from the loudspeaker to the microphone. As the sound source, I used a loudspeaker Fostex FD48D that was mounted on a supporting table. The loudspeaker was connected to an amplifier with a fixed gain and signal generator type Iwatsu FG-4321.

To measure the sound pressure generated by the loudspeaker, a working standard microphone type B&K 4939 serial number 2851722 was used. The reference microphone has been calibrated by the manufacturer and stored in the microphone database. A sensitivity database was provided by the manufacturer in compact disc media bundled with the microphone. The microphone was hanged on a supporting rod made from aluminum with a distance of 43 cm above the loudspeaker. A laser alignment-line Bosch GLL 3-50 was used to align the microphone to the loud-

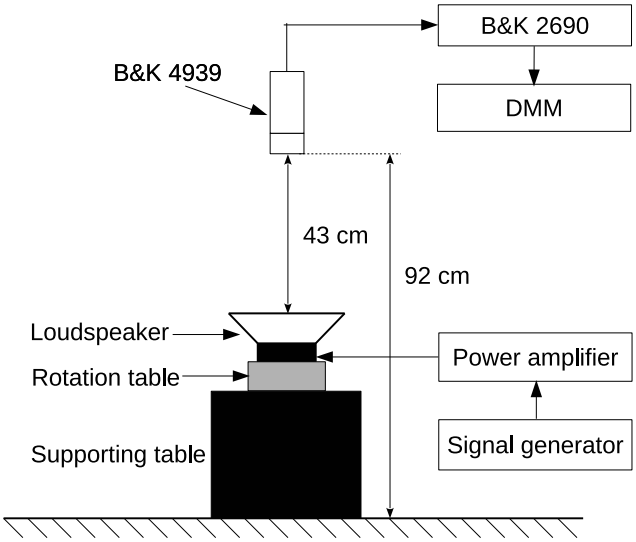

Figure 5.1: Instrument setup for initialization step.

speaker's cone center. The microphone output signal was amplified by conditioning amplifier type B&K 2690, while the signal output from the conditioning amplifier was measured by a $6^1/_2$ digit multimeter type Tektronix DMM4040.

The working standard microphone's sensitivity for each calibration frequency was corrected according to the environment condition. Since I used the microphone in a free field environment then I used a free-field frequency response of the corresponding microphone from the database. A software B&K Microphone Viewer was used to retrieve the data from the database. A reference sound source for the calibration was generated by adjusting the signal generator voltage setting so that the loudspeaker generates sufficient sound pressure without signal clipping. The process was repeated for each calibration frequency, and the voltage setting value for the corresponding frequency was noted.

5.2.2 Phase-measurement step

The phase measurement step is the implementation of sound field measurement using the PPSI system. The instrument configuration in this step is visualized in Fig. 5.2. The distance between the mirror and the reference plane of the PPSI system was 2.5 m. The DUT was positioned inside the PPSI measurement area and in the middle position between the mirror and was at the midpoint between the mirror and PPSI's reference plane. The DUT was installed in the same place as the working standard microphone as in the initialization step and aligned using a laser alignment-line. The realization of the phase measurement can be seen in Fig. 5.3. The recording setting of the PPSI was 50000 fps with an image resolution of 256 $\times$ 256 pixels. The loudspeaker was mounted on the rotating table to implement the tomography method in the measurement process. All instruments were connected to the National Instrument NI-PXI system for synchronization between the recording process and rotation of the table. A software was developed using LabView

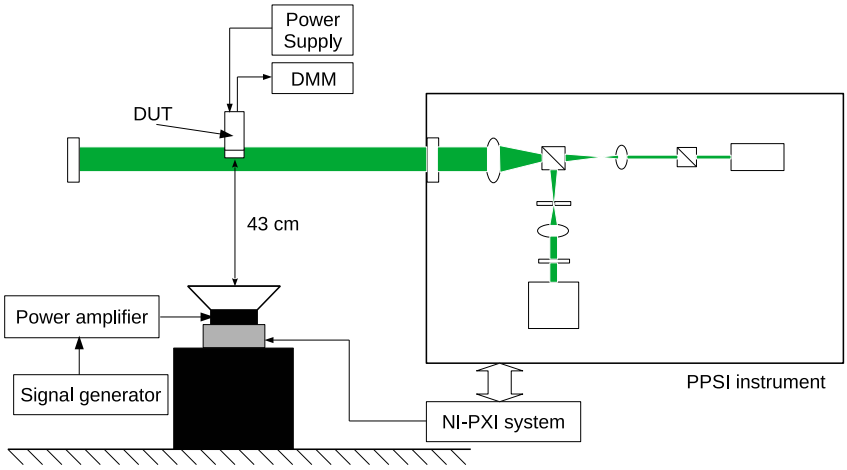

Figure 5.2: Instrument configuration of phase measurement step.

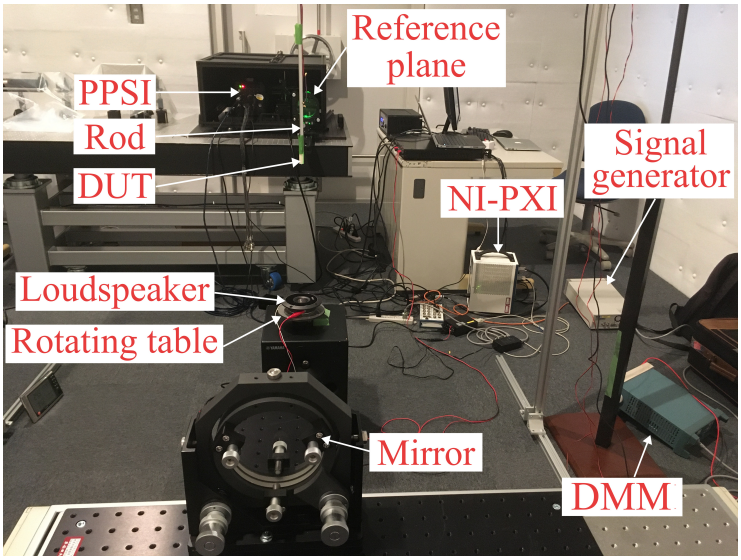

Figure 5.3: Photo of phase measurement configuration.

programming language to control the sequence of the process. I have described in Chapter 4 that measurement using PPSI is affected by the noise coming from the fan. Therefore, I developed a custom switch to turn off and resume the operation of the fan.

The sequence of the process in the phase measurement step is visualized in the flowchart as shown in Fig. 5.4. Before performing the measurement, the laser should be correctly aligned so that light interference occurs. The measurement started with initializing the position of the rotation table to 0 degrees. If the initialization of the table was finished then I generated the signal with the amplitude setting determined in the initialization step. Then, it was followed by turning off the camera. After the operation of the fan stopped, the PPSI started to record the interferogram. The recording period for each projection angle was 1.5 ms, and the total samples of 500

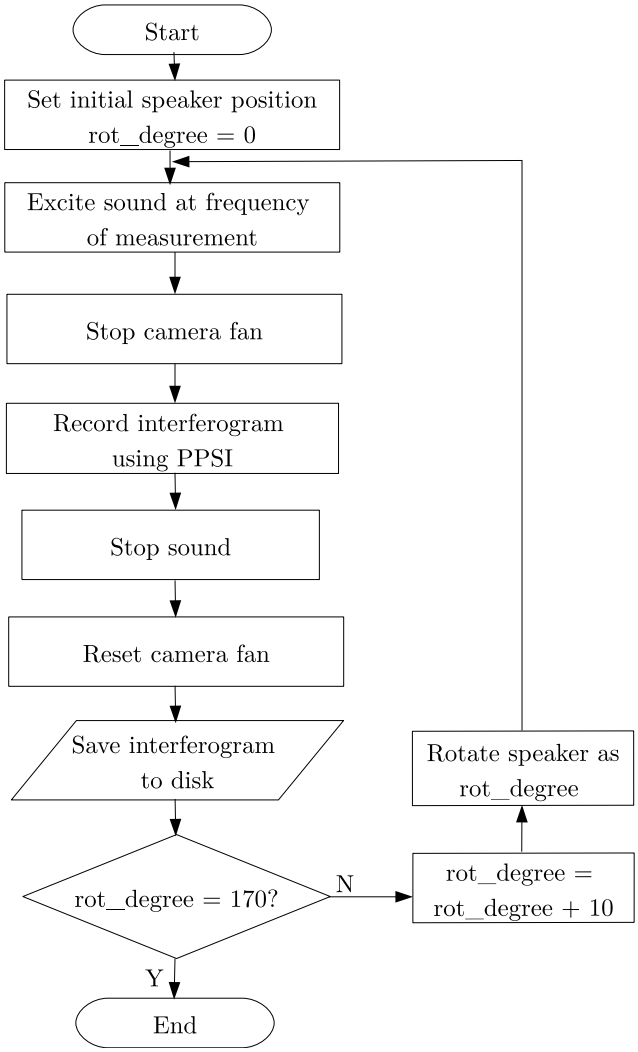

Figure 5.4: Flowchart of the phase measurement process.

interferograms per angle.

It is very important to maintain the stability of the sound pressure during the measurement process. Based on the observation, I found that the stability of the loudspeaker was decreased after a while. Therefore, I turned off the signal generator after recording. An environmental condition such as temperature, air pressure, and humidity was measured during the measurement process to calculate actual physical properties in the calculation of acousto-optic. For this purpose, I employed thermo-hygrometer Testo 622.

The rotation was performed from angle 0 degrees until 170 degrees with a rotation step of 10 degrees. The total files for one complete set of measurements were 9000 files. All the files were then transferred from the PPSI system onto an external drive for later processing.

5.2.3 Data processing step

The data obtained from the previous step is processed in this step. The main processes in this step are extracting the phase values from the recorded interferogram, reconstructing the sound field using the FBP technique, and calculate the DUT's sensitivity values. All the processes were implemented in the Matlab program with a sequence of the process described in the pseudocode 6.

Algorithm 6 Pseudo-code for extracting phase from measurement data.

Input: Recorded data
Output: Phase data

1: **for** iii=1 to $total_rotation$ **do**
2: $wrapped_phase = HEFS(Input)$
3: $phasemap\_tmp = unwrap(wrapped\_phase)$
4: **end for**
5: $Result = TDFS(phasemap\_tmp)$

Flowchart of the data processing step is shown in Fig. 5.5. Firstly, all the data were loaded into memory. A HEFS method was implemented to extract the phase information from the interferogram [103–105]. The output of the HEFS is the phase map which has the size half of the original interferogram size.

In this experiment, the size of the phase map was 126×126. However, the phase yield by the HEFS method was still unwrapped and contain a temporal static phase component. To unwrap and remove this static phase from the phase maps, I applied a time directional filter [106]. A ramp high-pass filter and Butterworth low-pass filter with the parameter $\Psi = 128$, $\xi_c = 1$, and $a = 2$ were applied to the FBP calculation. The spatial resolution which represented the translation step was calculated from the PPSI measurement area and the number of pixels on the diameter line. The value of this spatial resolution was 1.11 mm/pixel. Selected rows from phase maps were chosen for the reconstruction plane.

The Ciddor equation [107] was used to calculate the actual air refractive index using the temperature, air pressure, and humidity data during the measurement process. The other constants for calculation of acousto-optic were $k_0 = 1.181 \times 10^7$ and $\gamma = 1.4008$.

The final sound pressure value for the calculation of the microphone sensitivity was determined from the average sound pressure amplitude around the center point of the reconstruction plane. This sound pressure value, together with the output voltage of the MEMS microphone, was used to calculate the microphone sensitivity using the equation 5.1. In this equation, the sensitivity was represented in the unit of dBV/Pa unit.

$$S_{\mathrm{DUT}} = 20\log_{10}(\frac{V_{\mathrm{meas}}}{\tilde{p}}). \tag{5.1}$$

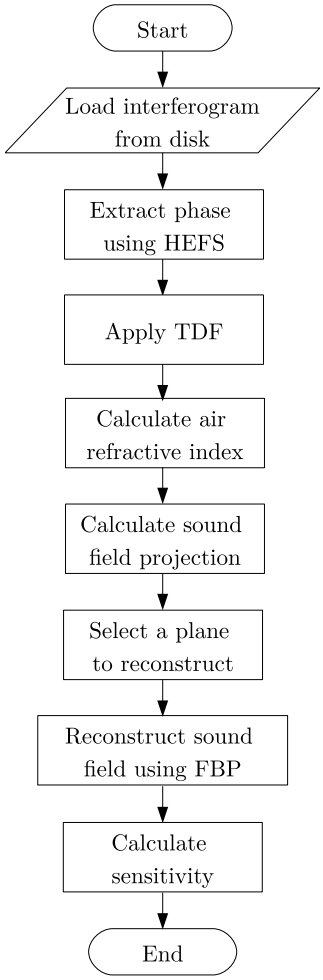

Figure 5.5: Flowchart of data processing.

5.2.4 MEMS microphone configuration

The geometry of the breakout is rectangular with a dimension of 10 mm length and a 7.5 mm width. The maximum thickness of the breakout including the MEMS microphone transducer, passive components, and the terminal soldering part is 2.1 mm. Therefore, I develop a rectangular area on top of a cylindrical adapter, which has a diameter of 12.7 mm or equal to 0.5 inches, equal to the dimension of a 0.5-inch condenser microphone. The rectangular area's dimension is 10.113 mm in length, 7.677 mm width, and 2.2 mm depth to accommodate the size of the breakout. I also created three ports for the cable path with and the total adapter length is 50 mm. This adapter was designed using AutoCAD 2016 software and realized using a 3D printer. The prototype of the adapter is shown in Fig. 5.6 below.

I started the frequency of calibration from 1000 Hz because the stability of the sound source system below 1000 Hz was not good. Another problem for frequency below 1000 Hz was the signal to noise ratio of the phase measurement using the PPSI system was very low. Thus, the resulted phase maps were very noisy. In the high frequency, I limited our experimental calibration at 12000 Hz to evaluate the

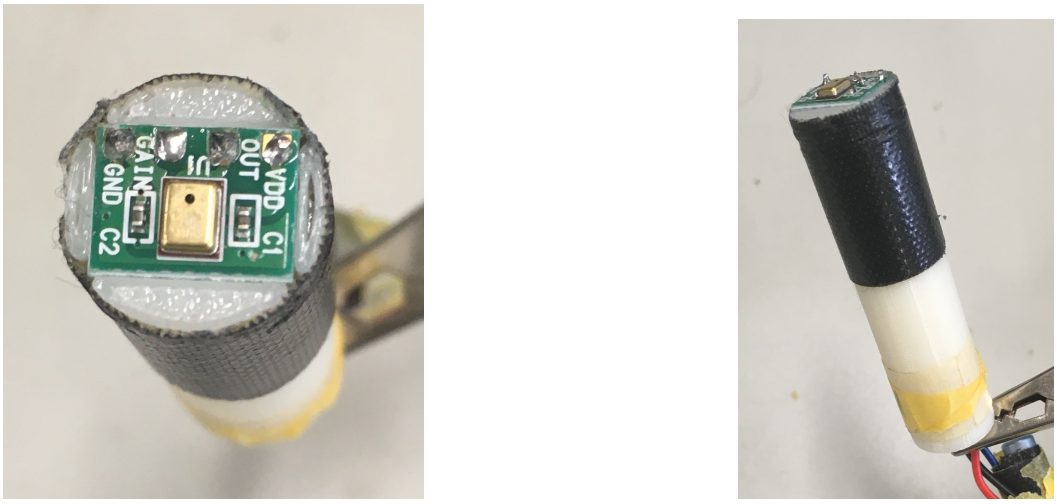

(a) Top view (b) Side view

Figure 5.6: The mounting of the MEMS microphone on the adapter.

alteration of sensitivity values at the high-frequency range.

5.3 Result and discussion

5.3.1 Experiment result

The example of interferogram recorded by PPSI at a projection angle of 10 degrees and sample number 90 with the frequency of the measured sound of 12000 Hz is shown in Fig. 5.7. The interferogram in Fig. 5.7 is composed of four phase-shifted interferograms. The pixel values for the corresponding phase retardation angle was represented by the image intensity level. The measurement area of the PPSI can be seen as the circle inside the image. We can see the shadow of the microphone inside the image because, at this part, the laser light is blocked. Thus the interference doesn't occur. Hence, the area became darker than the surrounding. Figure 5.8 shows the image intensity for each corresponding retardation angle.

By implementing the HEFS method and unwrapping the resulted phase using the TDF method, I obtained the phase map as seen in Fig. 5.9. The color in Fig. 5.9 represents the magnitude of the phase-shift. From the phase map, the wavefront of a sound wave can be seen. The blue color represents the wave crest state, and yellow represents the wave trough. The coordinate of each pixel in the phase map describes the corresponding position in the measurement area of the PPSI system. Based on the phase map, I determined the line's position corresponds to the plane on the surface of the DUT. In Fig. 5.9, it is marked in red dashed-line, which corresponds to position $y = 12.1$ relative to the center of the measurement area.

The FBP method was then applied to reconstruct the sound field from the phase map data. The process reconstructs the sound pressure distribution on the surface of the DUT. For calculating the microphone sensitivity, I averaged the sound pressure on an area with a diameter of 6.363 mm on the reconstruction plane.

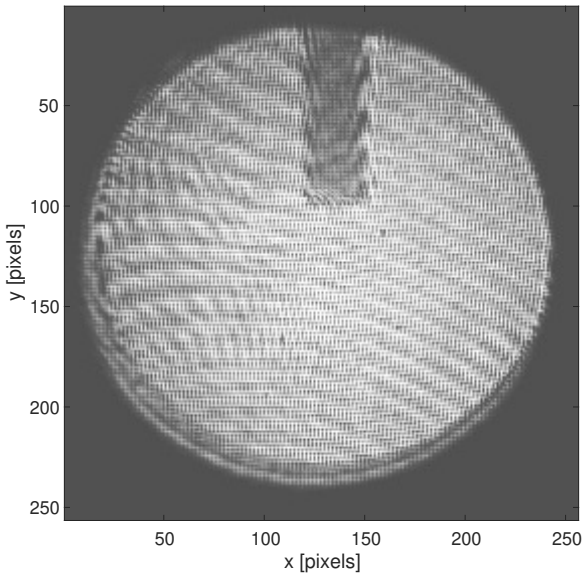

Figure 5.7: Recorded interferogram by PPSI.

For validation of the proposed method, I performed a substitution calibration method for the same DUT. The substitution method calibration procedure has been described in Chapter 2. I used microphone type B&K 4939 as the reference microphone. It was positioned at a distance of 43 cm from the loudspeaker. The reference sound was then generated by the loudspeaker and then the reference microphone was substituted with DUT. The voltage output of the DUT was used to calculate the sensitivity. The performance of calibration using the optical method was evaluated by comparing the sensitivity result with the substitution method result.

The experiments were performed three times for each calibration method to observe the standard deviation of the calibration result. The frequency response result is shown in Fig. 5.10. The sensitivity results obtained using the optical method are represented by the blue line. Meanwhile, the result of the substitution method is shown by the red line.

According to the MEMS microphone datasheet, the sensitivity at 1000 Hz is -22 dBV/Pa with a three dBV/Pa tolerance. The implementation of the proposed optical method yielded a sensitivity of -21.5 dBV/Pa, while the substitution method yielded -21 dBV/Pa. These results are closed with the typical sensitivity value written in the datasheet. It shows that the substitution method and the optical method can be used to determine MEMS microphone sensitivity, and the result is in agreement with the microphone specification.

The microphone's sensitivity in a specific frequency range is represented as the frequency response of the microphone. From Fig. 5.10, I found that the MEMS microphone frequency response is flat at a frequency range lower than 3000 Hz and starts to increase from frequency 4000 Hz to 12000 Hz.

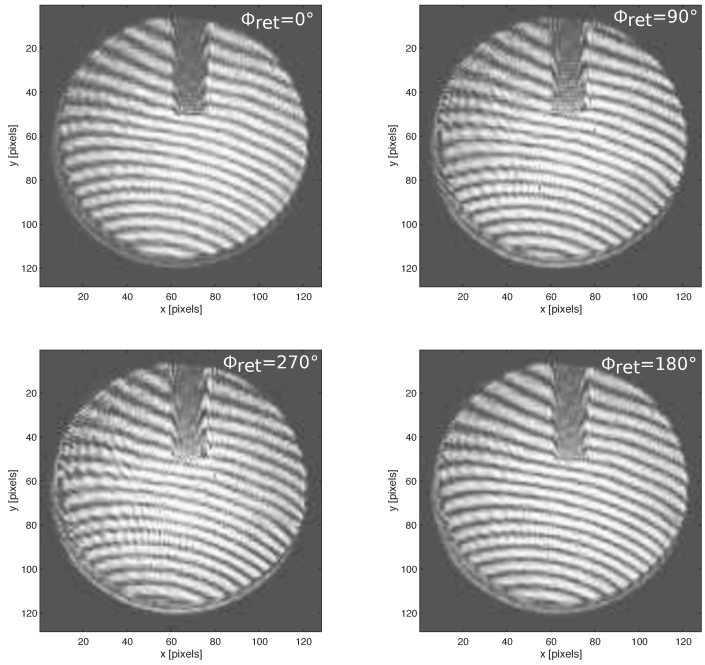

Figure 5.8: Interferogram for each corresponding retardation angle.

The minimum standard deviation obtained by the substitution method is 0.03 dBV/Pa at the frequency of 10000 Hz, while the maximum standard deviation of sensitivity was 0.29 dBV/Pa. This evidence shows that the substitution method's implementation has a good reproducibility result, thus providing good reliability to be used for validation.

The frequency response produced by the optical method agreed with the substitution method with small discrepancies. This fact is supported by the overlapped error bar value in Fig. 5.10. The maximum discrepancies are 0.5 dBV/Pa at the frequency of 1000 Hz and 5000 Hz. The optical method's maximum standard deviation sensitivity was 0.65 dBV/Pa, which is still good enough compared with the sensitivity tolerance given in the datasheet.

I compared the frequency response resulted from calibration with the datasheet. The frequency response in the datasheet is flat in all frequencies. But, the datasheet does not mention the calibration method that is used to determine the frequency response. However, compared to the typical free-field frequency response of a conventional condenser microphone, I found that a traditional condenser microphone's free-field frequency response has a characteristic similar to our result. Mydlarz *et al.* [90] shows that the increase of the sensitivity in the high frequency is caused by the effect of MEMS microphone mounting on the PCB. Helmholtz resonance inside the inner chamber was also responsible for increased sensitivity for frequency above 10000 Hz [108].

I found from the implementation of the substitution method that the minimum standard deviation was 0.03 dBV/Pa at a frequency of 10000 Hz, and the maximum

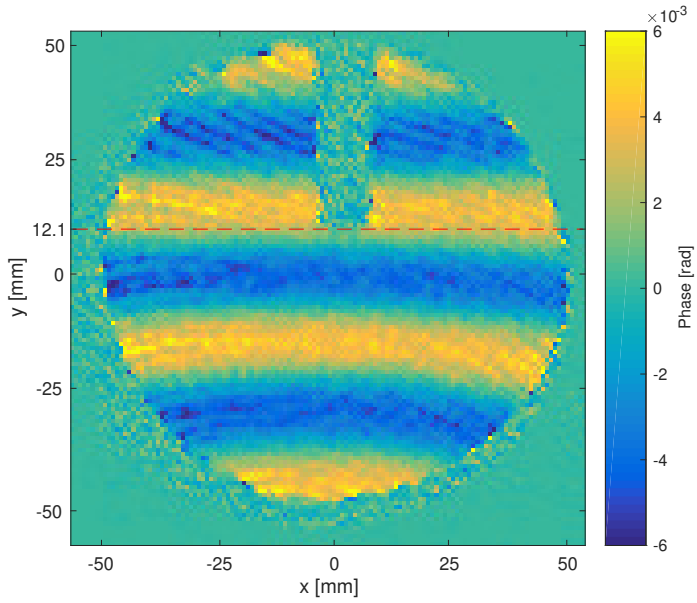

Figure 5.9: Phase map result from the interferogram.

was 0.29 dBV/Pa at the frequency of 2000 Hz. Meanwhile, the optical method's minimum standard deviation was 0.21 dBV/Pa at a frequency of 5000 Hz, and the maximum standard deviation was 0.62 dBV/Pa. The result shows that there is variation in the sensitivity result obtained by the repeated calibration process. The variation of the sensitivity results was caused by the instability of the loudspeaker during the calibration process.

The discrepancies of the sensitivity result between the optical and substitution methods are 0.5 dBV/Pa at a frequency of 1000 Hz. At a frequency of 3000 Hz, the discrepancy is only 0.06 dBV/Pa. The maximum discrepancy occurs at the frequency of 5000 Hz, which is 0.62 dBV/Pa. The discrepancy occurred because I assumed that the sound field applied to the reference microphone and the MEMS microphone was the same in the substitution method. Meanwhile, in the optical method, I measured the actual sound pressure applied on the MEMS microphone's surface. There was a sound from the instrument and floor reflection that affected the sound field applied to the MEMS microphone. As a result, the sound pressure distribution on the MEMS surface and the sound pressure entering the inlet port of MEMS were changed. This alteration in sound pressure distribution yielded a difference in the sensitivity result. The difference in sensitivity result by the optical method is also caused by the instability of the loudspeaker's sound pressure during the phase measurement step. The sound field reconstruction error occurred when the sound pressure from a different projection angle was different.

The substitution calibration method determines the microphone's sensitivity from the sensitivity of the reference microphone. However, the definition of microphone sensitivity is obtained from the ratio between the applied sound pressure to the microphone's output voltage. This definition can not be achieved using the

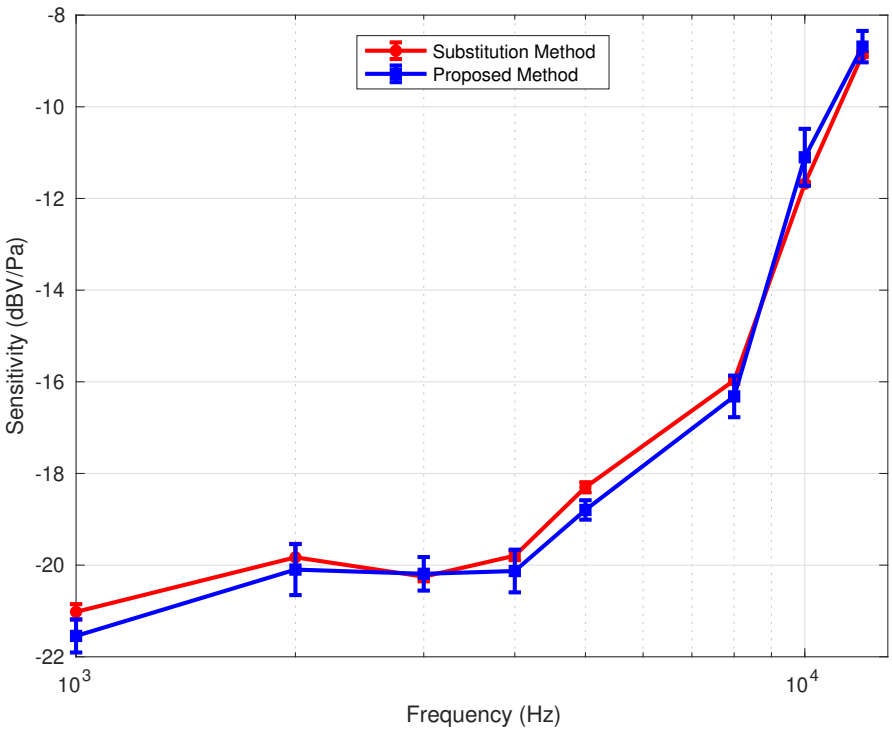

Figure 5.10: Comparison of frequency response.

substitution method. The optical method realizes this definition by measuring the sound pressure and the output voltage from the calibrated microphone.

5.3.2 Measurement uncertainty sources

The main process in calibration is measurement. Because the measurement always contains an error, it is necessary to include a range value that covers the actual value of a measurand to express a result of calibration. This range is expressed as the measurement uncertainty. According to the GUM (Guide to the Expression of Uncertainty in Measurement), the definition of measurement uncertainty is the parameter related to the measurement which described the dispersion of the value of the measurand. Measurement error sources are from the components that affect the measurement, such as the measurement method, instruments used in the calibration, environmental condition, and calibration operator. Therefore, the first step in the determination of measurement uncertainty is identifying the uncertainty components.

Common method used to identify sources of measurement uncertainty is fishbone diagrams or Ishikawa diagrams [109, 110]. The diagram shows the cause and effect of an event. I implemented the Ishikawa diagram to identify various effects in our proposed calibration method to estimate uncertainty. I identified four main uncertainty components in the calibration system: output voltage, pressure ampli-

tude, sound source, and residual effect. The represented in Ishikawa diagram shown in Fig. 5.11.

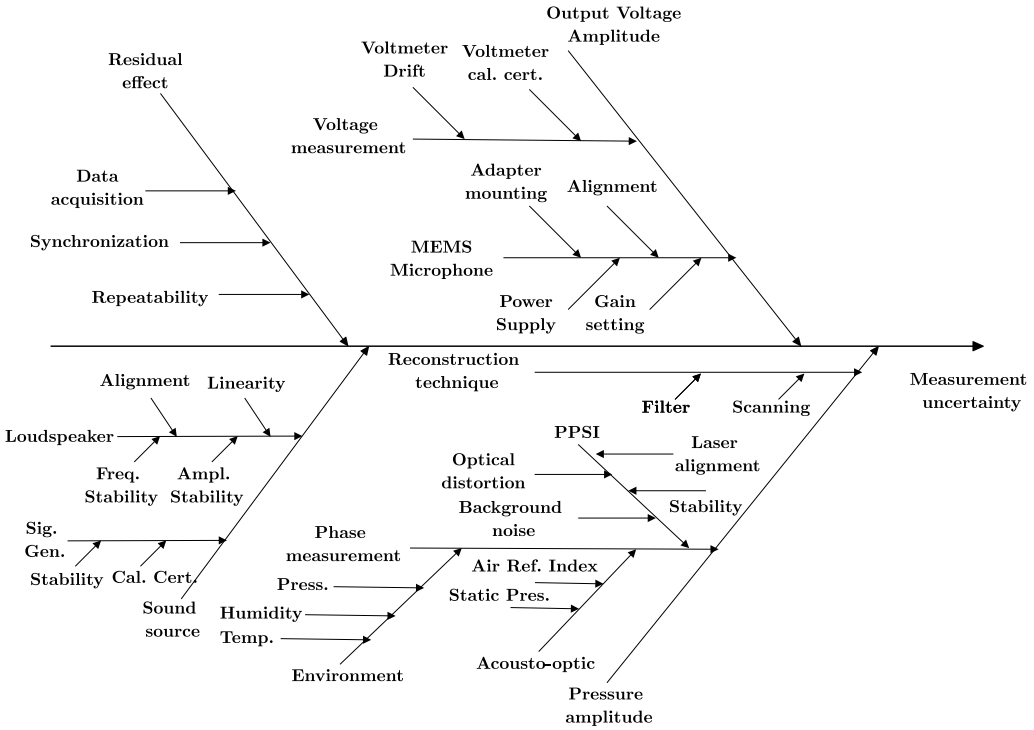

Figure 5.11: Uncertainty analysis using Ishikawa diagram.

Output voltage amplitude

The proposed calibration method measured the sound pressure and output voltage from the MEMS microphone. Obviously, the output voltage from the microphone affects the calibration results. There are two main components cause variations in the amplitude of the output voltage. First, the voltmeter that is used for voltage measurement. To determine how much the contribution voltmeter to the calibration uncertainty, we can figure it out from the voltmeter's calibration certificate. We should also consider the drift of the voltmeter would increase the uncertainty contribution.

Another component that affects the output voltage is the MEMS microphone itself. According to the observation, the output voltage from the MEMS microphone can be affected by four factors. In order to work, the MEMS microphone requires an external power supply. In fact, there is a minimum supply voltage to apply to make the MEMS microphone working properly. The MEMS microphone also has an integrated pre-amplifier. To set up the gain of the pre-amplifier, passive components such as resistor and capacitor are used. These passive components have a tolerance that varies the pre-amplifier gain. Thus, vary the MEMS microphone output voltage. In the calibration, the MEMS microphone breakout is mounted on a self-made adapter. Improper mounting of the microphone to the adapter affect

the sound field applied to the microphone and its output voltage. The alignment of the adapter to the loudspeaker also affected the output voltage because of the microphone directivity.

Pressure amplitude

Another major contribution of uncertainty is in the results of the phase measurements. I have identified several sources of uncertainty that affect sound pressure measurement. The main processes in the pressure measurement are phase measurement using PPSI and reconstruction of the sound pressure using filtered back-projection. The acoustic and optic relation is given by the acousto-optic relation, which includes the air refractive index and static pressure in the calculation. The actual air refractive is influenced by the environmental condition as described in the Ciddor equation. Where each instrument used for measuring environmental conditions also contributes to the uncertainty of the calibration system.

The PPSI is the main part for the measurement of phase measurement. I have described the PPSI characterization in Chapter 4 and found that there are background noise and optical distortion, which causes the phase measurement error. Hence, I need to include these uncertainty components into the uncertainty calculation. Laser alignment also has a major contribution to measurement error in systems that uses laser interferometry. Because PPSI instruments also use laser interferometry, it is important to include laser alignment error to phase measurement error. Another thing that needs further analysis is the effect of environmental conditions on phase changes.

For the reconstruction of the sound field, I implemented the tomography method, which includes a reconstruction process. I have shown in Chapter 3 that the reconstruction of the sound field using FBP produces an error in the pressure result. This error is contributed by the translation error during the scanning process and the filters used in the reconstruction process. Therefore, these processes should be added to the uncertainty sources.

In the calibration, I generated a reference sound source using a loudspeaker. The sound is generated by the signal generator and converted into sound by the loudspeaker. The signal generator's contribution to measurement uncertainty is from the calibration certificate of the signal generator and the stability of the generated signal. Another source of error in the calibration system being developed is the loudspeaker for reproducing sound. Because the loudspeaker produces the sound, the stability of the sound pressure level and frequency can produce an error in the calibration result. Moreover, since the loudspeaker being used also has a directivity, then the loudspeaker's alignment also contributes to the uncertainty of the calibration.

Residual effect

The residual effect covered the other sources contributing to the measurement error. These include the error from the high-speed camera system while capturing the interferogram. In the implementation, the measurement process is automated using

the NI-PXI system. The NI-PXI synchronize the PPSI's camera and the movement of the motor for rotating the loudspeaker. The synchronization error between the camera and motor operation produces a phase measurement error that affects the accuracy of the calibration result.

5.4 Conclusion

The MEMS microphone is different from a conventional condenser microphone in size and geometry. The conventional microphone's diaphragm size is in the range of centimeters, while the MEMS microphone size is in micrometer. The diaphragm of a conventional microphone is directly exposed to the sound field. Meanwhile, the diaphragm of the MEMS microphone is located inside the microphone housing and exposed to the air through a port. Since the calculation of the sensitivity of the current calibration method is derived from the geometry of conventional condenser microphones, it cannot be applied directly to calibrate mems microphones.

In this study, I propose a new approach to the microphone calibration method. The sensitivity is calculated from the measurement of the sound field applied to the microphone and its output voltage. Hence, it can be applied without the influence of size and geometric shape. A non-invasive sound field measurement based on acousto-optic effect is realized using a PPSI instrument to determine the sound field on the MEMS microphone's surface.

The calibration procedure consists of three stages, namely the initialization step, phase-measurement step, and data processing step. The initialization step is used to set the voltage setting to generate the reference sound source. The tomography scanning process using the PPSI instrument is implemented in the phase measurement step to obtain the sound field's projection. The data processing step processes are the extraction of phase map from the interferogram data, reconstruction of the sound field from the projection, and calculation of the sensitivity.

An experimental calibration of the MEMS microphone using the proposed method has been realized in the frequency range of 1000 Hz to 12000 Hz. A MEMS microphone adapter was developed to mount the MEMS microphone in the calibration setup. The microphone was positioned at the center of the PPSI measurement area with a distance of 43 cm from the loudspeaker. The tomography scanning process was implemented by using a PPSI instrument with a rotation step of 10 and recorded by the PPSI with a sample rate of 50000 fps and an image size of 256 $\times$ 256 pixels.

Phase-maps were successfully extracted from the recorded interferogram data using the HEFS algorithm and TDF filter. A filtered back-projection technique was implemented to reconstruct the sound field from the projection. For the reconstruction, a ramp high-pass filter and Butterworth low-pass filter was implemented with the properties of $\Psi = 128$, $\xi_c = 1$, and $a = 2$.

The sound field was successfully reconstructed on a plane associated with the surface of the MEMS microphone, and the voltage output from the MEMS microphone was measured using a voltmeter. The sound pressure level for the calculation of sensitivity was obtained from the average of measured sound pressure on the sur-

face of the MEMS microphone. Finally, the sensitivity was calculated by dividing the output voltage by the sound pressure level.

A substitution calibration method was implemented to validate the sensitivity result of the proposed method. From the comparison, it is shown that both methods yield a good agreement on the sensitivity results. The substitution method's reliability for validating the proposed method was demonstrated by the maximum measurement standard deviation of 0.29 dBV/Pa. The maximum sensitivity discrepancy between the proposed method and the substitution method was 0.62 dBV/Pa at a frequency calibration of 5000 Hz. In comparison, the minimum discrepancy was 0.06 dBV/Pa at the frequency of 3000 Hz.

I identified four main causes affecting the calibration results. The first is the components that affect sound pressure measurements, namely the instruments used for phase measurement, such as the PPSI instrument, and the techniques used for sound field reconstruction. The second is the components that affect the measurement of the output voltage, namely the instrument used to measure the MEMS microphone's voltage and internal properties, which can affect the performance, such as power supply and pre-amplifier gain.

For the future work, the proposed calibration method should be validated with a more precise microphone calibration method such as the reciprocity method in a suitable calibration environment. More experiments have to be done to quantify the contribution of each uncertainty source that has been identified.

Chapter 6

Determination of microphone acoustic center using optical method

6.1 Background

The microphone's free-field sensitivity can be determined accurately by using the free-field reciprocity microphone calibration method. In the calibration process, two microphones are configured pair-wise and facing each other to be a transmitter and receiver transducer. They are acoustically coupled in axis and separated each other at a certain distance. The sensitivity is determined from the acoustic model derived from the geometry of the microphone. For the calculation, the physical properties of the microphone are required.

The distance between the microphones is an important parameter that affects the accuracy of the calibration results. The distance between microphones is not the distance between the microphone diaphragm but the distance between the microphone's acoustic center. The acoustic center is the position of an equivalent point source of a microphone that acts as a transmitter unit.

The acoustic center can be determined by exploiting the property of the point sound source. The propagation of sound pressure generated by the microphone from the acoustic center's position will follow inverse distance law. Thus, the acoustic center can be estimated from the rate of pressure changes. This condition occurs if the receiver microphone in the reciprocity arrangement acting as a point receiver. However, the body of the receiver microphone will disturb the sound field of the transmitter microphone. Hence, the acoustic center can not be estimated accurately. As a solution, the acoustic center is determined from the measurements of the electrical transfer function. The transfer function is obtained from the measurement of the electrical transfer function of three microphones as in reciprocity calibration.

In this research, we proposed a novel approach for the determination of acoustic center. The acoustic center is estimated from the sound field generated by the microphone under test. An optical sound measurement method is implemented to

obtain the sound field of a microphone act as the transmitter unit. A sound field of point sound source model is used to approximate measured sound field data to estimate the acoustic center position. For the realization, the PPSI instrument was used to record the phase shift of the light corresponds to the sound based on the acousto-optic effect principle. In the experiment, we estimated the acoustic center of laboratory standard microphone type B&K 4180 using the proposed method. The estimation result is validated by the IEC 61094-3 to evaluate the proposed method's accuracy.

6.2 Laboratory standard microphone

Condenser microphone is commonly used as a measurement microphone because it has a simple shape, design, and flat frequency response [111]. The construction and working principle of the condenser microphone has been described in Chapter 2. Because of its simple design, the properties of the microphone can be studied. Based on their characteristic, the measurement can be categorized into classes. A working standard microphone is typically used for field measurement instruments such as sound level meter and audiometer. For the standardization, the specification of working standard (WS) microphone have to fulfill standard IEC 61094-4 [112].

Another class of measurement microphone is the laboratory standard (LS) microphone. The shape of both microphones is the same. But, the laboratory standard microphone has high sensitivity stability over a long time. The LS microphone specification is described in the IEC 61094-1 [25]. This type of microphone is used as the reference microphone for calibration purposes. Currently, there are two types of LS microphones, namely LS1p and LS2p. The difference between the two is in the size of the diaphragm. The LS1p has diaphragm size of 1 inch while the LS2p diaphragm size is 1/2 inch as shown in Fig. 6.1 (a) and 6.1(b) .

(a) Type LS1p (b) Type LS2p

Figure 6.1: Two types of laboratory standard microphones [113].

The LS microphone is a reciprocal microphone that can produce output voltage when received sound and reproduce a sound when a voltage is applied in the microphone terminal. The amplitude of the output voltage generated by the microphone for the applied sound pressure is represented by the microphone sensitivity value and vice versa.

The properties of this microphone has been studied thoroughly [23, 114]. Not only the frequency response characteristics of the microphone but also the environmental influence on microphone sensitivity are known and documented in the standard IEC 61094-2. The sound field on the microphone diaphragm for the simple sound source can be estimated and modeled based on the microphone's geometry. The model is then used to develop the microphone calibration method.

The reciprocity method is the most precise microphone calibration method. The calibration method and procedures have been described in Chapter 2. In the reciprocity principles, the product of the free field sensitivities between two microphones is equivalent to the ratio of the electrical transfer impedance and acoustical transfer impedance of the microphones. The electrical transfer impedance between the microphone pair is determined by measuring the transmitter input current and receiver output voltage using the insert voltage technique. Meanwhile, the acoustical transfer impedance is calculated from the acoustic propagation model derived from a condenser microphone's equivalent circuit under free-field. The information about the environmental condition and the distance between the transmitter and receiver microphones is required to accurately calculate acoustical transfer impedance.

6.3 Microphone acoustic center

The actual distance between the transmitter and receiver microphone in the reciprocity calibration is not determined from the physical distance between the microphone's diaphragm. It is the distance between the acoustic center of the microphones. The acoustic center is defined in the IEC 61094-3 as "point from which approximately spherical wavefronts from sound-emitting transducer producing a sinusoidal signal at a given frequency appear to diverge with respect to a small region around an observation point at a specified direction and physical distance from the sound source" [115]. At this location, either the transmitter and receiver microphone will act as a point source and point receiver where the reciprocity principle is applicable [116, 117]. The location of the acoustic center is unique for every microphone and has frequency dependency. The acoustic center is also influenced by the receiver orientation and its distance from the transmitter. The determination of the acoustic center is important to obtain accurate sensitivity results.

Several analytical and numerical methods have been proposed for the determination of the microphone's acoustic center. The method is developed based on the characteristic of the point source. Previously developed methods are: the acoustic center's estimation based on the inversely proportional distance law of sound propagation of point source using scanning microphone and boundary element method (BEM) [114, 118].

The transfer function method has been implemented to determine the acoustic center of microphone type LS2. The result has a good agreement with BEM, and the value given in the IEC Publication 486 document [119]. The acoustic center's estimation based on phase measurement is also found in the literature [120, 121]. The implementation of these methods for condenser microphones has been briefly discussed by Jacobsen *et. al* [122]. Rodrigues *et. al* improved the acoustic cen-

ter measurement technique by using inverse distance law-based methods. By the method, the calibration frequency range can be extended [123].

6.4 Estimation method

According to the definition, the acoustic center is the position of the point source generated by the microphone. The position of the point source is not exactly at the diaphragm but slightly ahead or behind the microphone diaphragm as shown in Fig. 6.2. The sound radiated by a point source at the origin propagating spherically

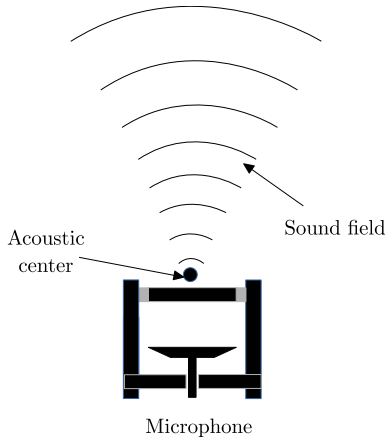

Figure 6.2: Illustration of microphone acoustic center.

with a complex sound field of

$$p(r) = \frac{p_0}{r} e^{jkr}, \tag{6.1}$$

with parameter of r is the relative distance to the origin. In three dimensional cartessian space, the value of r is calculated as $r = \sqrt{x^2 + y^2 + z^2}$.

The optical sound field measurement based on acousto-optic effect principle has been described briefly in Chapter 2. It is mathematically written as:

$$\phi_s(x, y, t) = k_0 \frac{n_0 - 1}{\gamma p_0} \int_0^Z p(x, y, z, t) dz. \tag{6.2}$$

This equation implies that phase-shift of the light is proportional to the line integral of sound pressure along the optical path.

The measurement principle can be exploited to obtain a two-dimensional projection of spherical sound propagation. This principle is implemented by performing a scan on the selected axis in the measurement area. Hence, we obtain a two-dimensional matrix of phase shift. Each point in the phase-shift matrix represents the sound pressure amplitude at a corresponding point in the measurement area described in the Eq. 6.2. The projection area is perpendicular to the scanning axis.

A measurement of phase shift can be realized using a laser interferometry instrument such as LDV or PPSI instrument. If using LDV, the scanning process is carried out sequentially at each point in the measurement area. The distance between scanning points determines the resulting projection resolution. A PPSI instrument can

be used to obtain the phase-shift on the measurement area simultaneously. The data processing of the recorded image by the PPSI produces a two-dimensional matrix known as a phase map. Each point in the phase-map matrix represents the amplitude of sound pressure at the measurement area's corresponding position. This matrix is equivalent to the projection of the scanned sound field.

When the transmitter microphone is positioned inside the measurement area of the PPSI and excite a sound, the sound field of the microphone can be projected. The resulted phase map represents the projection of sound propagation originated from the acoustic center of the microphone. Suppose we assumed the propagation of the sound follows the point source model. In that case, we can estimate the acoustic center's position from the sound propagation data using the point source model. A least-square fitting method can be used to determine the sound propagation model's parameter from measurement data.

The phase maps matrix is represented as the variable $\tilde{S}(x, y)$, and the sound field is modeled as

$$S(x, y) = \int_{-z}^{z} \frac{p_0}{r} e^{jkr} dz. \tag{6.3}$$

where $r = \sqrt{(x - x_0)^2 + (y - y_0)^2)}$ is the distance from the acoustic center coordinate (x_0, y_0). A least square method can be used to minimize the sum of squared error between the measurement data and the fitted value provided by the model as

$$\min_r \sum (\tilde{S}(x, y) - S(x, y))^2. \tag{6.4}$$

6.5 Numerical simulation

A numerical simulation of the estimation process was created to evaluate the estimation method's performance. The direction of the light beam is on the z axis. Thus, we have the projection plane on the x and y axis. The point source is simulated in the middle between the light source and the projection plane. Illustration of the simulation configuration is shown in Fig. 6.3.

The point source was simulated at the $y = -0.57167$ mm from the bottom in the upward direction. The visualization of the point source sound propagation for the frequency of 50000 Hz is shown in Fig. 6.4.

The size of the projection plane was simulated to be 64×64 pixels representing the measurement area of 36.6×36.6 mm. In a PPSI measurement system, this projection plane corresponds to the phase-map matrix. A pixel in the projection plane corresponds to the interval of 0.57167 mm in the measurement area by this configuration. A projection was obtained by calculating a line integral of sound pressure in the range of -1.25 m to 1.25 m. The range represents the distance between the reference plane and the mirror of the PPSI system.

A MATLAB's non-linear least square function $lsqonlin()$ was used to estimate the point source's position from the projection data. The $SpecifyObjectiveGradient$ algorithm was selected for the parameter of $lsqonlin$ function. From the estimation result, the point source position is at $y = -0.57167$ mm, which is the simulated point source's exact position. This condition means that the estimation correctly

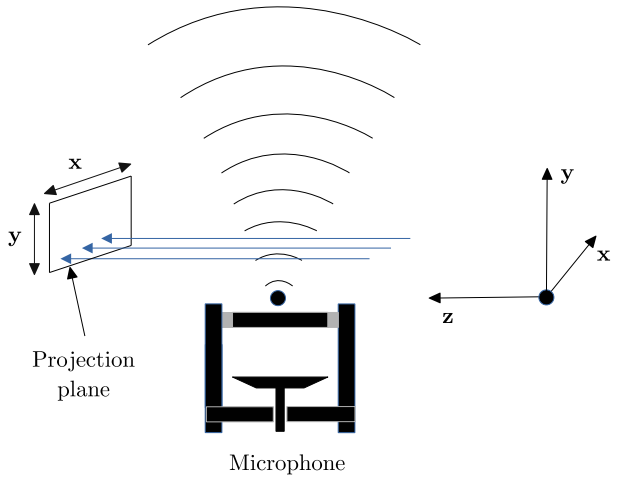

Figure 6.3: Simulation configuration and axis convention.

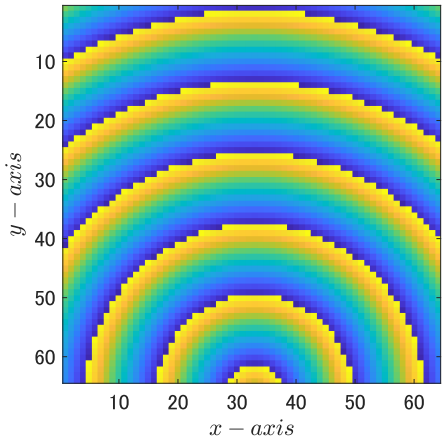

Figure 6.4: Original sound field of point source at frequency 50000 Hz.

estimated the position of the point source from projection data. The sound field's visualization based on the estimated point source position result is shown in Fig. 6.5. The image shows that the sound propagation from the estimated point source position matches the simulated point source.

To evaluate the performance of the estimation method in noisy data, we added normally distributed random noise to the phase map data and perform the estimation with a noise level of a 10%. The visualization of noisy projection data can be seen in Fig. 6.6(a) . With the noise random noise of 10%, the estimation result yields a value of -0.56886 mm. The error of estimation result is about 2.8043×10^{-3} mm.

Evaluation of the estimation method at different noise levels was performed by adding random noise with the level in the range of 10% to 50%. The error in the estimation result for different noise levels is plotted as a curve to evaluate the estimation method's performance. The result is shown in Fig. 6.7. We can see from

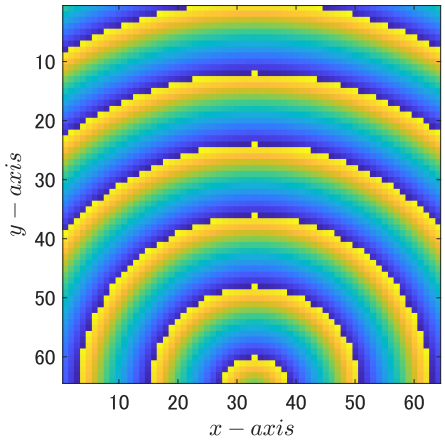

Figure 6.5: Phase map of measured sound field.

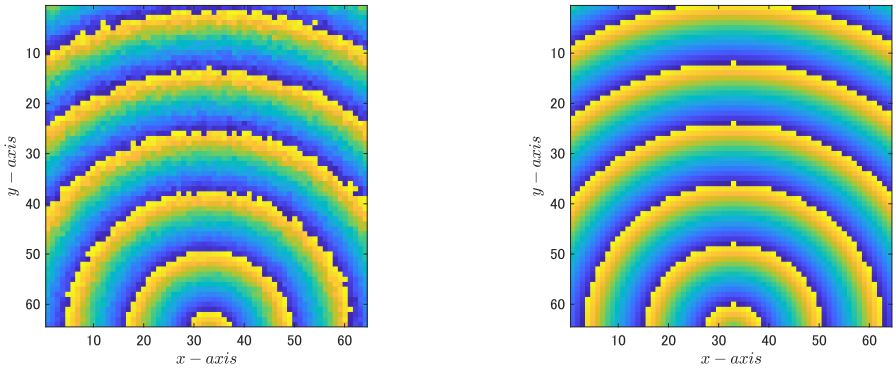

(a) Noisy sound field

(b) Reconstructed

Figure 6.6: Reconstruction of noisy sound field.

the figure that the estimation error increases as the noise level increases. We found that the estimation error increases significantly when the noise level is above 40%. At a noise level of 50 %, the deviation between the true point source position and the estimation is about 0.0744 mm. The overall estimation error for the noise level below 50 % is still below 0.1 mm.

The sound field of a point source with a noise level of 50% can be seen in Fig. 6.8(a). It is seen from the figure that the visibility of the wavefront is low. Hence, yield a higher estimation error. The sound field of the point source at the estimated position is shown in Fig. 6.8(b). It is seen that the visualization of the estimated sound field still shows a similar result with the sound field of the point source.

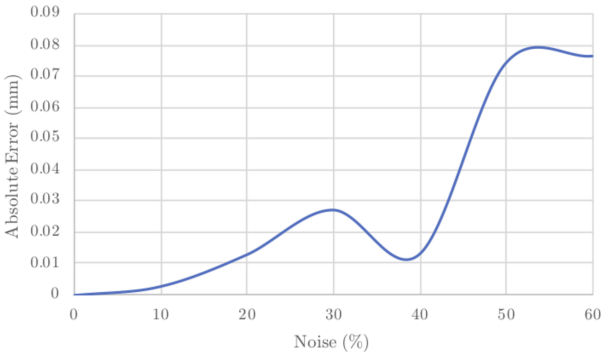

Figure 6.7: Point source position estimation error for different noise level.

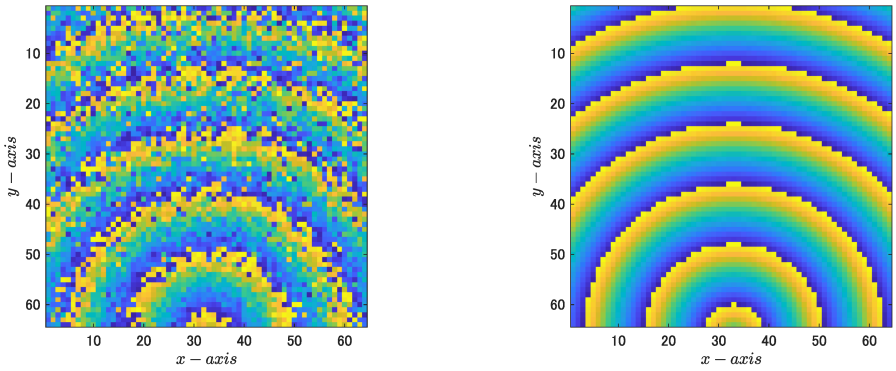

(a) 50% noise level (b) Reconstructed

Figure 6.8: Reconstruction of sound field with 50% noise level.

The performance of the estimation for different frequencies were evaluated by simulating a point source for different frequency in the range of 5000 Hz to 50000 Hz, while the position of the point source was fixed at 0.5717 mm. The estimation error for different frequencies is shown in Fig. 6.9. The result shows that the estimation

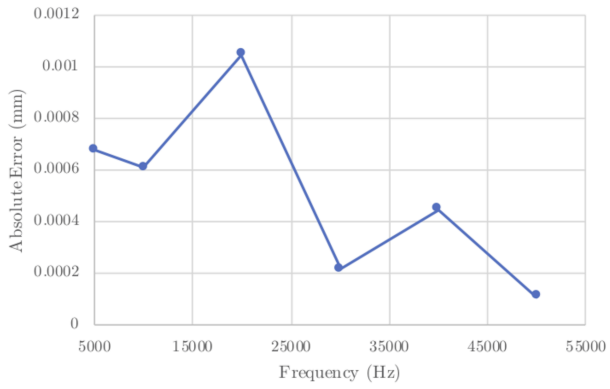

Figure 6.9: The estimation error of point source position for different frequencies.

error decreases as frequency increases. The improvement of the estimation result occurs because the number of wavefronts covered inside the measurement area that is used for estimation calculation increases as frequency increases. Therefore, the measurement data contain more information for the least square fitting process. This result shows that the estimation method has better performance for the high-frequency range.

6.6 Experiment

6.6.1 Measurement Configuration

In this experiment, we determined the acoustic center of LS2p microphone type B&K 4180 serial number 3055348. This microphone is a reciprocal microphone that can be configured as a transmitter and receiver. In this experiment, the microphone was configured as a transmitter unit. The microphone requires a polarization voltage of 200 V. A polarization voltage calibration unit type B&K 5008 is used to provide the microphone's polarization voltage. On the microphone adapter, there are two connectors AC and DC. The DC connector connects to the polarization input voltage, while the AC connector is the input signal to the microphone. The setup of the instrument is shown in Fig. 6.10.

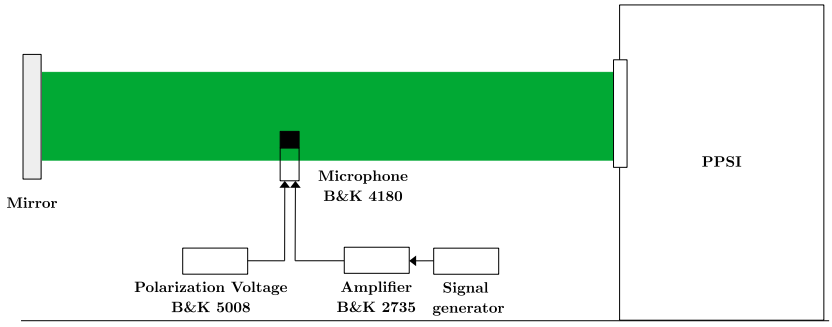

Figure 6.10: Configuration for the experiment.

A signal generator was built on the NI-PXI platform using LabVIEW programming language. The output signal from the generator was connected to amplifier type B&K 2735. The gain setting on the amplifier was set to 20 dB. The output of the amplifier was connected to the AC input connecter on the adapter to drive the microphone. The amplitude of the signal was set to 1 V.

A microphone type B&K 4939 was used to measure the sound pressure level generated by the microphone type B&K 4180. This microphone is positioned facing toward the microphone type B&K 4180 at the center of the PPSI measurement area as shown in Fig. 6.11. The output of microphone type B&K 4939 was connected to a conditioning amplifier type 2690, and the output from the conditioning amplifier was connected to the input channel on the NI-PXI system. The Bosch GLL 5-50 line laser was used to align microphone alignment.

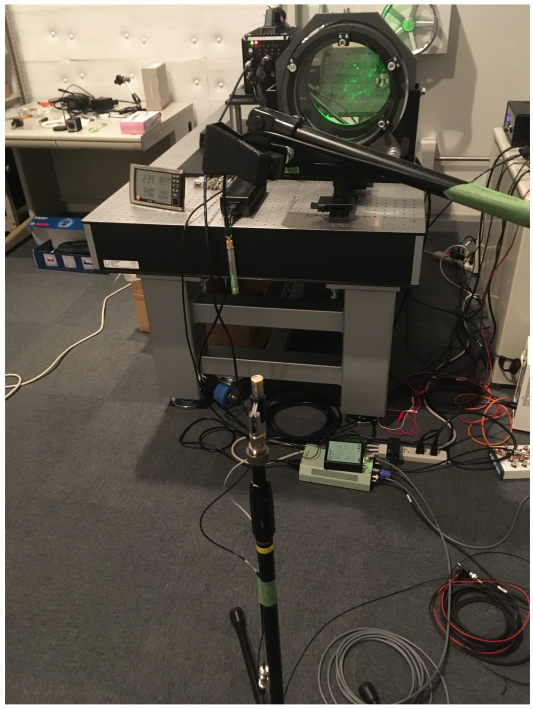

Figure 6.11: Measurement of SPL generated by the microphone type B&K 4180.

A spectrum analyzer software was developed using LabVIEW to obtain the sound pressure level of the microphone type B&K 4180. The analyzer's sampling rate was set to 150 kHz, and the number of samples is 1500.

With the current PPSI's sample rate setting, the PPSI measurement area's dimension became 128×128 pixels. The microphone was adjusted so that the annulus' position was at the boundary of the measurement area as seen in Fig. 6.12. Therefore, the distance between the microphone and boundary of PPSI's measurement area was 0 cm.

The sound pressure level generated by the microphone type B&K 4180 at several frequencies are shown in Fig. 6.13

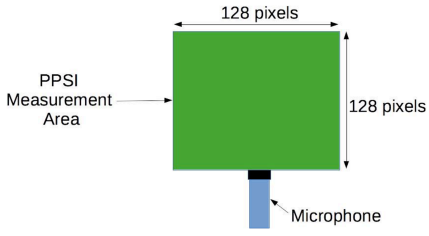

Figure 6.12: Position of the microphone on the PPSI measurement area.

Table 6.1: Sound pressure level generated by microphone type B&K 4180 at several distances from PPSI measurement area.

Freq. [Hz]	SPL [dB]		
	0 cm	2 cm	4 cm
10000	67.75	63.16	58.38
20000	87.27	78.05	74.05
30000	89.93	79.86	76.00
40000	86.84	79.00	75.25
50000	86.80	79.05	75.44

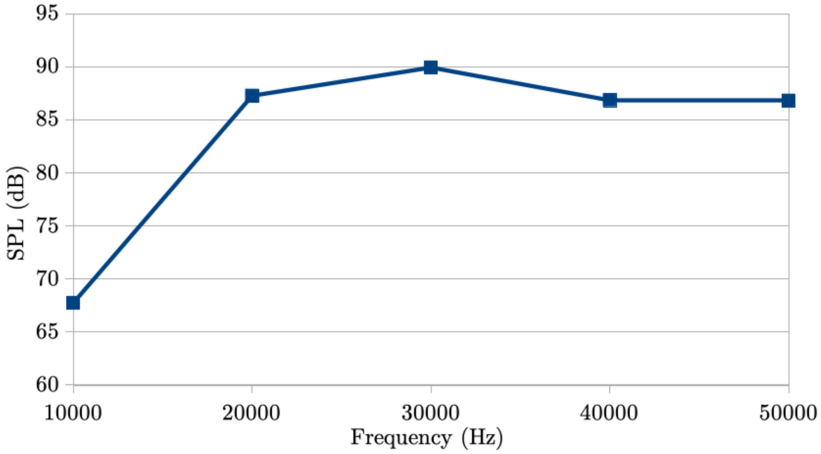

Figure 6.13: Sound pressure level generated by microphone type B&K 4180 at a distance of 0 cm from PPSI measurement area.

From the image, we see that the sound pressure level generated by the microphone type B&K 4180 has frequency dependency, especially in the low frequency. In the frequency 20 kHz and higher, the sound pressure level is almost flat around 86 dB and a maximum of 89.9 dB at 30000 Hz.

The environmental background noise is about 20 dB. Meanwhile, the PPSI requires the measured signal to be at least 40 dB above the background noise. The microphone's minimum sound pressure level was 67 dB, which has a difference of 47 dB above the background noise. Therefore, we expected to get sound field data in the frequency measurement of 10000 Hz when the microphone's distance to the measurement area was 0 cm.

The photograph of the measurement process is shown in Fig. 6.14. We analyzed the sound pressure level generated by the microphone at several distances from the measurement area of PPSI. We adjust the microphone position at a distance of 2 cm and 4 cm. The result is summarized in the Table 6.1.

It is seen from the table that the SPL dropped significantly when the microphone was moved away from the measurement area of the PPSI. At a distance of 2 cm, the SPL dropped at a maximum of 9 dB in the frequency above 10000 Hz. While at

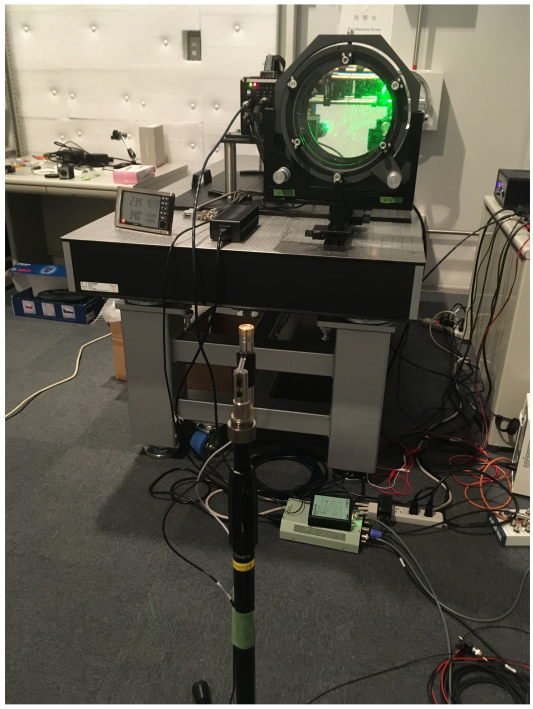

Figure 6.14: Photograph of the measurement process.

frequency 10000 Hz, the SPL dropped only about 4 dB. At a distance of 4 cm, the SPL dropped about 11 dB in the frequency above 10000 Hz and dropped about 9 dB at the frequency 10000 Hz. The cause of this significant drop in sound pressure is probably the alignment between the microphone type B&K 4180 and type B&K 4939.

The deviation between the generated SPL and background noise at a distance of 2 cm and frequency of 10000 Hz is about 43 dB. Within this level, the sound pressure can be sensed by the PPSI, but the signal to noise ratio is low. At a distance of 4 cm, the difference with the background noise is about 38 dB. Thus, it cannot be sensed by the PPSI. In other frequencies than 10000 Hz, the differences from the background noise are higher than 40 dB. Hence, the measurement using PPSI is still can be done.

6.6.2 Measurement procedure

The procedure comprises of the phase-measurement process using a PPSI instrument and data processing. The procedure for phase-measurement using PPSI has been described briefly in Chapter 5. The same procedures were applied to this experiment. However, this experiment has a slight difference from the previous experiment in Chapter 5. The difference is in the process of storing interferogram data recorded by PPSI. The recorded image was saved in the MRAW format instead of the ordinary RAW format. This process was done because the number of collected samples was 150000. Using this format, all image samples are embedded in a single file to reduce the file transfer time. Option for saving in the MRAW for-

mat was selected in Photron's FastCam Viewer application software. Two files are created by the PPSI for one measurement. One file contains the interferogram data in MRAW format, and the other file contains the setting of the PPSI. The transfer was successfully reduced from 24 hours to 40 minutes. A single measurement in the MRAW format took a space of 24 gigabytes on the disk.

The data processing includes the extraction of the RAW data images from MRAW file, phase-maps retrieval from the recorded interferogram, and the acoustic center's estimation. A MATLAB routine written by Markus Lindner was used to open and retrieve frames from the MRAW file [124]. A MATLAB software was developed to extract the interferogram sequentially and saved the extracted file in a folder. The flowchart of the extraction process is shown in Fig. 6.15. The result of this process is the interferogram data in RAW format.

The next process was the retrieval from recorded interferogram data. The standard procedure to extract phase-shift from the interferogram has been described

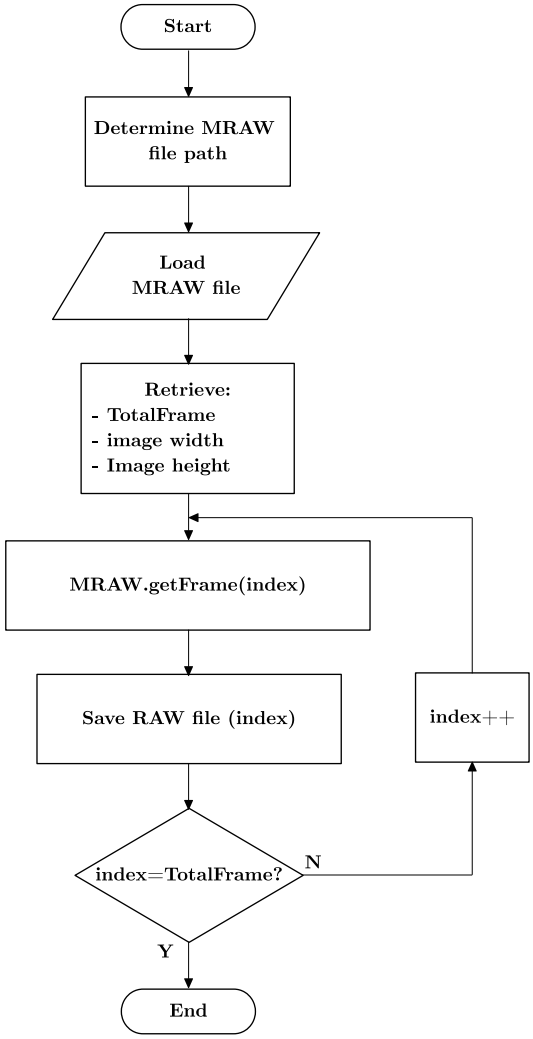

Figure 6.15: Flowchart of MRAW data extraction.

in Chapter 5. The process includes phase retrieval using the HEFS algorithm and phase unwrapping process. The resulted phase map has a size of 64×64. The final phase map file size for the estimation process was 67 kilobytes.

The final process is the estimation of the acoustic center from the phase map data. The estimation method has been described in the section 6.4 of this chapter. The result of the estimation process is the position of the point source. Nevertheless, the location of the point source is not exactly the position of the acoustic center. In order to determine the acoustic center from the estimated point source location, it is needed to consider the geometry of the microphone.

The microphone structure without the protective grid is shown in Fig. 6.16. The figure shows the view of the microphone seen from the side. The top part of the microphone seen from the side is called the annulus. The microphone diaphragm part is not directly located at the annulus but a certain distance from the annulus. The distance between the annulus and the diaphragm is called the front cavity depth. This value is different for each microphone. For a very accurate determination of front cavity depth, a special measurement technique is required [125, 126].

The acoustic center is represented by the distance of the point source relative to the diaphragm. Therefore, to determine the acoustic center, we have to consider the front cavity depth. In Fig. 6.16, the variable B represents the front cavity depth of the microphone. Meanwhile, variable A represents the position of the acoustic center relative to the annulus of the microphone. Therefore, the acoustic center is stated as C, which is the summation between A and B.

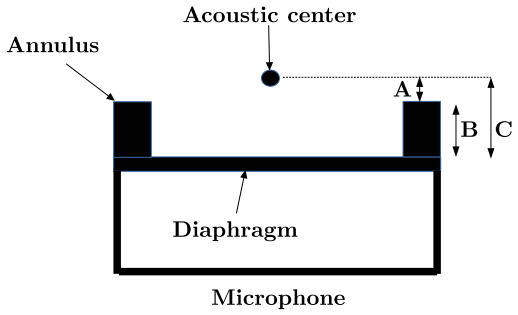

Figure 6.16: Position of acoustic center.

6.7 Result and discussion

6.7.1 Acoustic center estimation

The frequency used for experiments were 10000 Hz, 20000 Hz, 30000 Hz, 40000 Hz, and 50000 Hz. The measurements were repeated three times for each frequency, and the total number of measurements was 15. Meanwhile, for each measurement, the size of the MRAW file is 24 gigabytes. Therefore, the total amount of space used to store the measurement results is 360 gigabytes.

The PC used for the extraction process of MRAW files into RAW files, and the estimation calculation process has the specification of Intel i7 processor and

32 gigabytes of RAM. The time is taken to extract an MRAW file, calculate the phase-map, and estimate the acoustic center was approximately 2 hours. Therefore, the total time to proceed with measurement data was 30 hours.

The value of front cavity depth for microphone type B&K 4180 was obtained from the nominal value described in the IEC standard. The nominal front cavity depth of the LS2p microphone is 0.48 mm.

The final acoustic center result was reported as the average of three measurement data. The standard deviation was calculated to obtain the estimation result's distribution and expressed as an error bar in the chart. To validate the proposed method, the result is compared against the acoustic center's nominal value described in the standard IEC 61094-3.

We conducted the experiments with three different configurations. We measure the microphone's sound field placed at a distance of 0 cm, 2 cm, and 4 cm from the PPSI measurement area. The result is shown in Fig. 6.17.

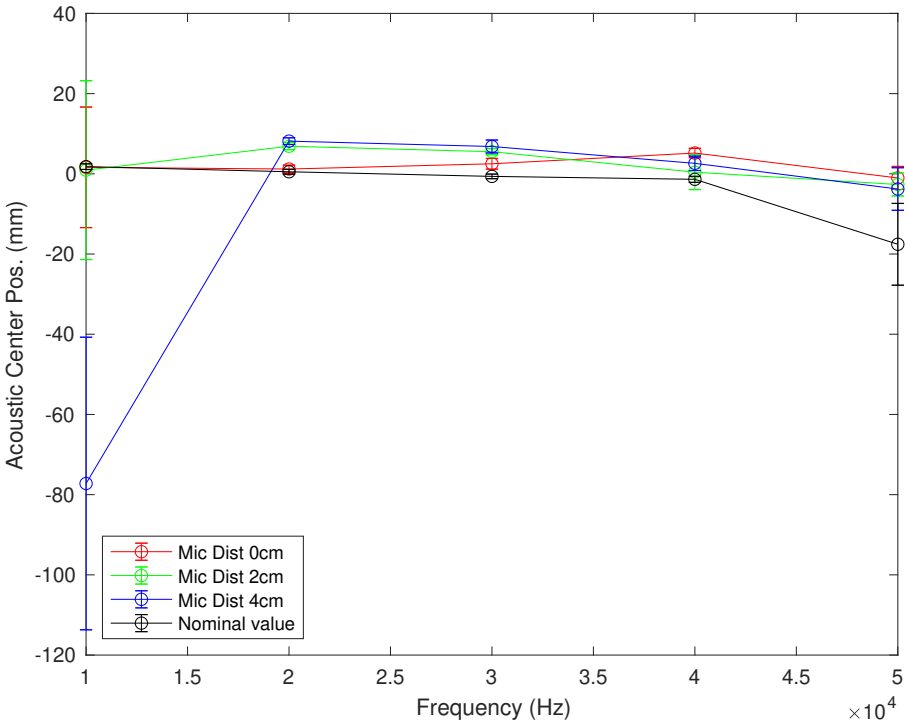

Figure 6.17: The estimation of the acoustic center with three different microphone positions.

We see that estimation yield a reliable result except for a frequency of 10000 Hz from the figure. From the error bar, we see that the standard deviation of the estimated results exceeds 10 mm. This unreliable result shows that the sound field measurement data has high noise, causing a fairly high estimation error.

For further analysis, we plot the result with the frequency 10000 Hz omitted. The result is shown in Fig. 6.18.

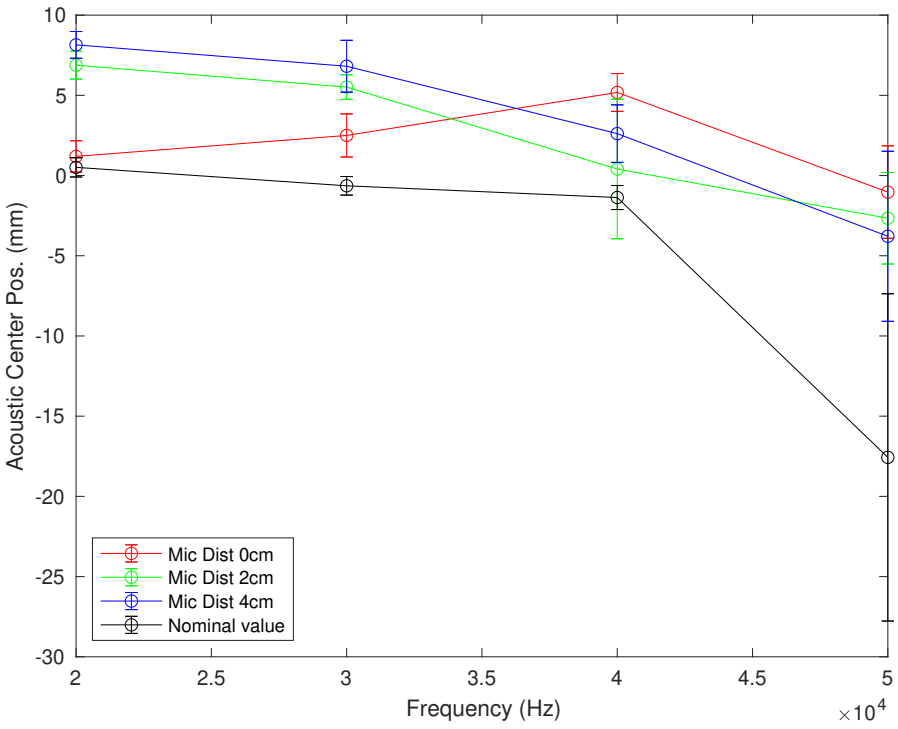

Figure 6.18: The estimation of the acoustic center with frequency 10000 Hz omitted.

From the error bar, it can be seen that the result has a fairly reliable value with a minimum value of 1 mm and a maximum value of 3 mm. This small error bar result indicates that the proposed estimation method can provide a reliable result with fairly good consistency. It was found that the standard deviation at 20000 Hz was smaller than other frequencies. The standard deviation of estimation was about 1 mm for three different microphone configurations. This result indicates that the sound field

The accuracy of the proposed method was evaluated by comparing the estimation result against the nominal acoustic center value of microphone type B&K 4180 described in the IEC 61094-3. It is seen from Fig. 6.18 that the estimation result is influenced by the distance of the microphone to the PPSI measurement area. At the frequency of 50000 Hz, the deviation of estimation result from the nominal value is large for all microphone configuration. This is due to the fact that the maximum sampling rate of PPSI is not high enough compared to the frequency of sound. This issue causes an aliasing in the sound field measured by PPSI, thereby reducing the estimation process's accuracy.

The estimation result of microphone distance of 2 cm and 4 cm yield almost the same result with the maximum deviation from the nominal value is about 15 mm at the frequency of 50000 Hz, while the other frequencies the deviation is about 6 mm. However, the estimation result when the microphone was configured at a distance of 0 mm to the measurement area of PPSI shows promising results. The

Table 6.2: Comparison of acoustic center between nominal value and estimated result.

Frequency [Hz]	Nominal value [mm]	Estimated value [mm]
10000	1.8	1.61
20000	0.51	1.19
30000	-0.64	2.50
40000	-1.37	5.18
50000	-17.57	-1.03

comparison with nominal value is shown in Table 6.2. From the table, we obtained that the minimum deviation from nominal value is 0.2 mm at frequency 10000 Hz. But since standard deviation of estimation at this frequency is 15 mm, then the estimation result at this frequency is not reliable. At frequencies 20000 Hz, the deviation is about 0.6 mm, and increases as frequency increases. In terms of accuracy and reliability of the acoustic center estimation method, configuration of the microphone at a distance of 0 cm to the PPSI measurement area is the best configuration in this proposed method.

6.7.2 Uncertainty components

An Ishikawa diagram is used to identify the uncertainty sources in the proposed measurement method. We categorized the uncertainty sources into three main causes. They are pressure amplitude, phase-amplitude, and microphone properties. The sources associated with the generated sound pressure are categorized into pressure amplitude. Sources that contributes to the phase measurement error are categorized into the phase-amplitude group. The sources related to the generation of sound pressure, which is the microphone, are categorized into microphone properties. While other sources that influence the estimation error are grouped into residual effect. The diagram is shown in Fig. 6.19.

Phase amplitude

This category is associated with instruments and procedures that can cause an error in the phase measurement. Since the measurement of phase was implemented using a PPSI instrument, then the uncertainty sources in this group are related to the PPSI instrument. The error in phase measurement can come from the PPSI system itself. The causes of errors in measurement using PPSI are optical distortion, background noise, laser alignment, and the laser wavelength's stability in the interferometry system. The environmental's static pressure and air refractive index stability during the measurement affect the resulted phase values because it is used in the calculation of acousto-optic. Environmental conditions such as temperature and humidity have the opportunity to influence the PPSI hardware in conducting interferogram recording.

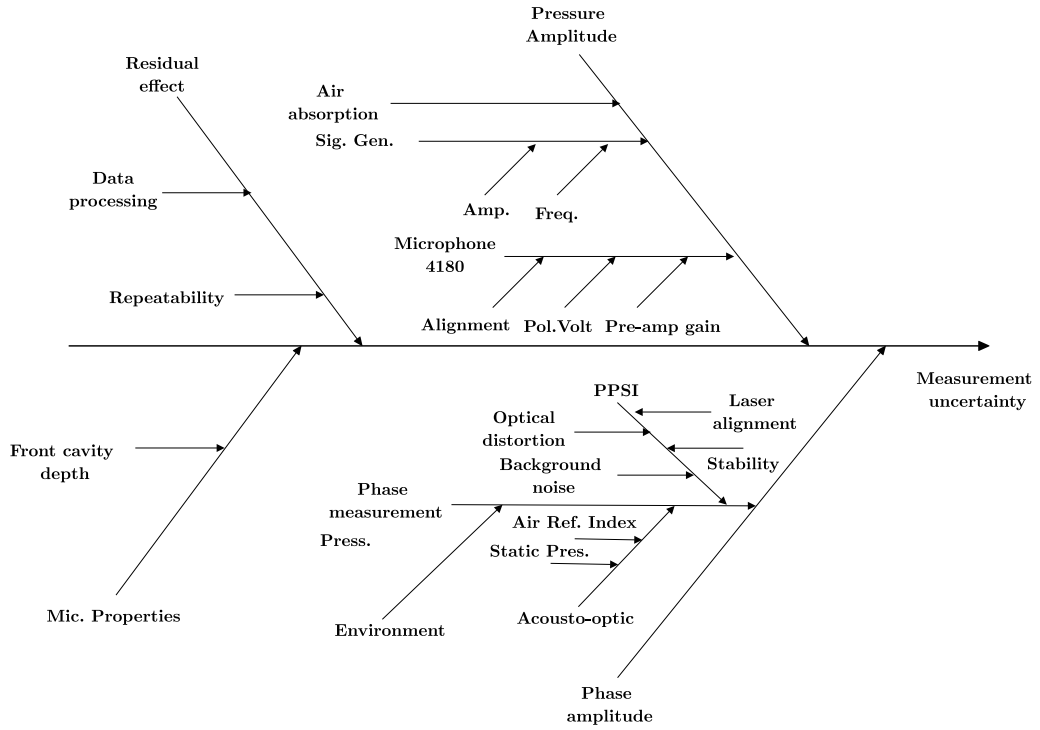

Figure 6.19: Ishikawa diagram of the proposed acoustic center estimation method.

Pressure amplitude

The proposed method estimated the acoustic center from the measurement of the sound field. Hence, the generated sound pressure has an important effect on the estimation error. Several things affect the generation of sound pressure produced, namely the signal generator, the sound absorption factor by air, which will affect the resulting sound field, and the microphone as a sound producer. A signal generator's influencing factor in a measurement system is the stability of the voltage amplitude and the resulting frequency. The stability of the sound pressure amplitude is also influenced by the microphone as the main component of the sound source. The factors that affect the stability of the sound pressure generated by the microphone are the polarization voltage, the amplification of the signal by the amplifier, and the microphone's position, as indicated by previous experimental results.

Microphone properties

The property of a microphone that affects the estimation result is front cavity depth. The value is used in the final calculation after estimating the point source position from the measurement data. As has been explained before that the value of the front cavity depth of each microphone is different. In measuring the value of the front cavity depth, it also contains a measurement error. Hence, the error in the front cavity depth measurement will affect the acoustic center estimation result.

Residual effect

Another source of uncertainty that affects the acoustic center estimation results is repeated measurements and errors caused by the data processing. The data processing from the interferogram file until the phase map results are obtained through several processes such as the phase extraction using the HEFS algorithm and phase-unwrapping. Each of these processes contains an error, which contributes to the phase map error.

6.8 Conclusion

Acoustic center is the position of an equivalent point source of a microphone act as a transmitter. It is used in the calculation of acoustical transfer impedance of microphone reciprocity calibration method. The current method to determine the acoustic center is the transfer function method. Three microphones are required for the implementation of the transfer function method. The acoustic center is estimated from the measurement electrical transfer function of the microphones.

In this study, a method to estimate the acoustic center's position has been realized using the measurement of sound field using PPSI instrument. The estimation performance was evaluated using a numerical simulation. The estimation method worked well in the noisy data with the estimation error is less than 0.1 mm for noise level between 10 % to 50 %. The estimation accuracy is increasing as the frequency increases with the estimation error is less than 0.001 mm. Experimental determination of the acoustic center of microphone type B&K 4180 was carried out in the frequency range of 10000 Hz to 50000 Hz.

It was found that the sound pressure level generated by the microphone at a frequency of 10000 Hz is lower than other measurement frequencies with the same applied input voltage. The average sound pressure level at a distance 0 cm from the PPSI measurement area was about 87 dB in the frequency range of 20000 Hz to 50000 Hz, while at 10000 Hz, the generated sound pressure level by the microphone was only 67.75 dB. As the distance from PPSI measurement area was moved from 0 cm to 2 cm, the pressure level dropped 9 dB. But, when the distance was doubled from 2 cm to 4 cm, the decrease of pressure level was only about 4 dB. This non-linear relation between the distance and the drop of pressure level was probably affected by the microphone alignment.

A reliable acoustic center estimation result was obtained from measurement at a frequency above 20000 Hz with the maximum standard deviation of 3 mm. The standard deviation of the estimation at the frequency of 10000 Hz was large caused by the low signal to noise ratio of the sound field measurement by the PPSI instrument. Hence, the estimation at the frequency of 10000 Hz is not reliable. The best overall estimation result was achieved when the microphone was positioned at a distance of 0 cm from the PPSI measurement area. In the frequency range of 20000 Hz to 50000 Hz, the minimum difference of the estimation result with the nominal value was 0.6 mm.

The uncertainty sources for the proposed acoustic center estimation method

has been identified and visualized using Ishikawa diaphragm. The main causes of acoustic center estimation error are coming from phase-amplitude measurement, pressure amplitude measurement, microphone properties, and residual effects.

For future works, it is necessary to determine each uncertainty component's value and its relation with the estimation error. This value can be determined through a further experimental process or other available resources. When each source of uncertainty's contribution value has been determined, the next process is to calculate the uncertainty of the proposed acoustic center estimation method.

Chapter 7

Conclusions

7.1 Summary

Measurement is important in our daily life. The development in measurement science is inline the technological development. Mechanical-based measurement methods developed at a time when mechanic-based technology developed. Currently, optical technology has developed rapidly. Optical-based measurement technology is developed for a wide variety of applications. Mechanical-based measurement technology has a limitation on dimension and geometry that can be solved using optical-based measurement technology.

Microphone is an acoustic transducer that converts sound pressure into voltage. The microphone's conversion ability is represented by the microphone sensitivity, which can be determined using calibration. Currently, available calibration methods are developed based on the geometry of conventional microphones. Hence, the methods cannot be applied to new types of microphones such as MEMS microphones. The MEMS microphone has the same working principle as the conventional microphone but different in shape and geometry from the traditional microphone.

This thesis addressed the geometry dependencies in microphone calibration methods by proposing direct sound field measurement using the optical method. In Chapter 3, I have demonstrated the realization of the acousto-optic based sound field measurement concept. A scanning tomography technique using a laser Doppler vibrometer has been successfully implemented to obtain the sound field's projection and reconstructed using the filtered back-projection technique. The sound pressure result was in good agreement with the microphone result.

Parallel scanning to obtain sound projection can be obtained simultaneously using the PPSI instrument. Before it is used to get the projection of the sound field, it is necessary to know the PPSI instrument's characteristics. Chapter 4 presents the investigation of the acoustical background noise and optical distortion of the PPSI instrument. It was found from power spectral density analysis that the system's acoustical background noise occurred at a frequency of around 3000 Hz when the PPSI's camera fan was turned on. The noise disappeared when the camera fan was turned off during the recording process by the PPSI. A calibration plate was employed to determine the optical distortion of the PPSI system. It revealed

that the optical distortion existed in the PPSI system with the type of pincushion distortion.

The proposed calibration method for MEMS microphones was described in Chapter 5. The calibration procedures consist of the initialization step, phase-measurement-step, and data processing. I demonstrated a calibration of a commercial MEMS microphone Knowles SPU0414HR5H-SB by utilizing a PPSI instrument. Validation of the sensitivity result was performed by the implementation of the substitution calibration method. The maximum discrepancy between the proposed method and substitution method was 0.62 dBV/Pa. The proposed calibration method's reliability was proven by the maximum standard deviation of the sensitivity result of 0.29 dBV/Pa.

A new approach for the determination of microphone acoustic center was described in Chapter 6. The acoustic center is the position of the equivalent point source of a microphone act as a transmitter unit. The conventional method for determining the acoustic center uses the transfer function method. The acoustic center is determined from the measurement of the electrical transfer function of three microphones in reciprocity configuration. In my approach, the acoustic center is determined from the projection of the sound field generated by the microphone based on the point source propagation model. Experimental acoustic center determination of laboratory standard microphone type B&K 4180 has successfully been implemented by utilizing the PPSI instrument. Validation of the results using the nominal acoustic center value described in IEC-61094-3 proved that this method could be used to find the acoustic center microphone value at frequencies above 10000 Hz.

7.2 Limitations and remaining issues

The result of measurement needs to be accompanied by an uncertainty value to express the measurement's quality. This study has focused more on proving a measurement concept without being accompanied by a stated uncertainty value, which is the limitation in this study. For that purpose, sources of uncertainty in the proposed calibration method have been identified and reported in the thesis.

In this study, the calibration was performed only to one MEMS microphone under test. Meanwhile, the developed calibration method's reliability needs to be tested further by calibrating various types of microphones from different manufacturers.

The experiments in this thesis were carried out in a room that was not dedicated to calibration. Hence, room conditions are not controlled. There is a possibility that environmental conditions influence the measurement results. The influence of environmental conditions on the measurement result has not been covered in this thesis.

Reconstruction is the main part of getting the sound field from the projection. Meanwhile, in this study, the only filtered back-projection technique was implemented for the sound field reconstruction process. To increase the precision of the reconstruction, the exact reconstruction technique can be applied [127–129].

7.3 Impact on metrology field

Optical-based measurement technology has a wide range of applications because the optical method can be used to solve measurement problems that cannot be accomplished by the mechanical or electrical based measurement system. The optical measurement precision is higher than the mechanical method, making it suitable for calibration applications.

Optical-based measurement technology has been used for the calibration of vibration sensors for a long time. Nevertheless, the optical method has not been adopted yet for the calibration of acoustic device calibration systems.

This study introduces the application of the optical method in the field of microphone calibration. Current microphone calibration methods determine the microphone's sensitivity under test from the reference microphone sensitivity and are not obtained directly from a pressure measurement. Hence, the method cannot be applied to microphones of a different size than the reference microphone. It is shown in this study that direct sound pressure measurement can be realized using an optical method. Therefore, the reference microphone is not required for calibration and can be applied to any microphone regardless of the size and dimension.

The impact of applying the optical method for microphone calibration is to shorten the traceability path of the microphone sensitivity unit to the SI unit. The acoustical unit's current traceability to the SI is shown in Fig. 7.1. From the figure, acoustic quantities are traced to the SI unit via a microphone artifact regarded as the reference standard. The quantity of this reference standard is determined by

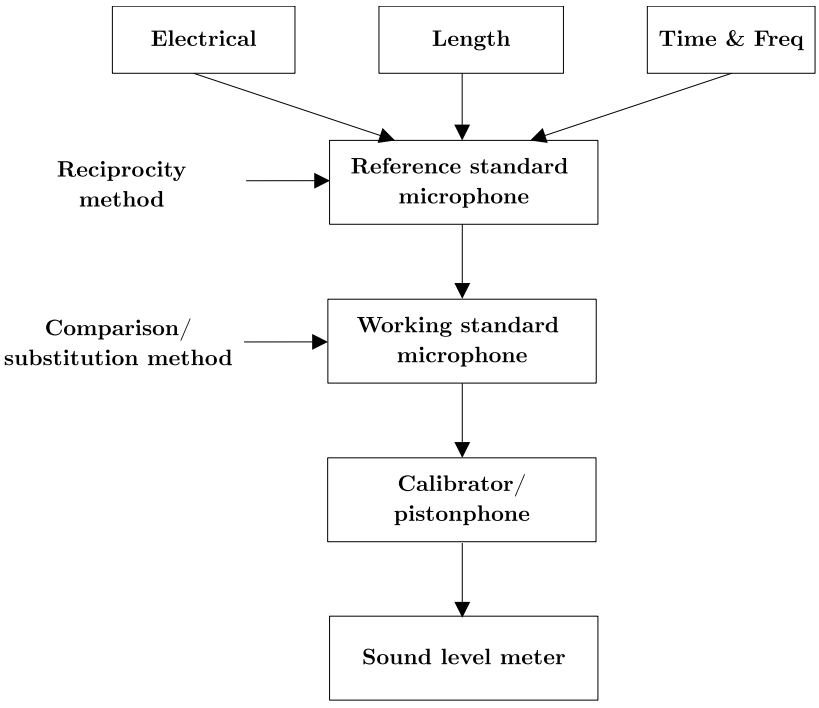

Figure 7.1: Current traceability chain of the acoustical unit to the SI.

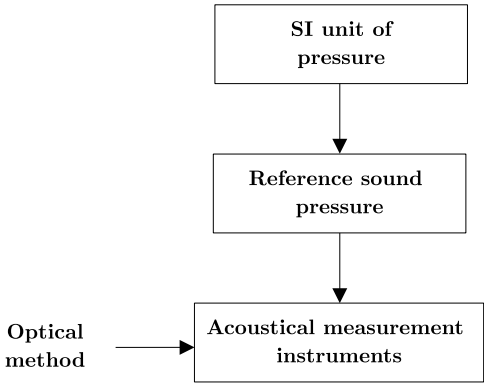

Figure 7.2: Acoustical unit traceability by the application of the optical method.

using the reciprocity calibration method. The reciprocity method is realized by measuring electrical transfer impedance and calculating acoustical transfer impedance derived from microphone geometry. Thus, the reciprocity calibration method has traceability to the SI units of voltage, time/frequency, and dimensions.

The reference artifact is then used to calibrate the working standard microphone by the implementation of the comparison/substitution calibration method. Furthermore, the working standard microphone is used to calibrate the acoustic calibrator. Finally, the acoustic calibrator is used for in-field calibration of the acoustical measurement instrument. Meanwhile, the longer the traceability chain, the less accurate the calibration results.

By the implementation of the optical method, the traceability chain of the acoustical unit can be reduced. The new traceability chain is shown in Fig. 7.2 The optical method has the ability to measure sound pressure directly. A reference pressure can be obtained directly from the definition of the SI unit of pressure. Furthermore, this reference pressure is used to calibrate acoustical measurement instruments using the optical method. Due to the short traceability path, the error caused by the calibration method will decrease, thereby increasing the accuracy of the calibration results.

7.4 Contribution to intermedia art and sciences

Knowledge about a quantity can be obtained through the measurement. This principle also applies to art. Knowledge about artworks can be obtained through a process of measurement. The knowledge gained from this measurement can then be processed to be assessed or further developed.

To take measurements, a transducer is needed to transform from one quantity to another. The microphone is the key device for the measurement of artworks related to sound. With conventional microphone technology, the number of measuring points is limited because of the microphone's size. Nevertheless, with the invention of the MEMS microphone, microphone dimensions size is no longer a limitation. The MEMS microphone can reach the smallest corners that previously could not be reached using conventional microphones. The more measuring points, the more

information will be obtained.

The correctness of the measurement using a microphone is determined by the correctness of the sensitivity value of the microphone. Currently, there is no standard calibration method for MEMS microphones. My proposed MEMS microphone calibration method can be used as an alternative approach to determine the MEMS microphone's actual sensitivity.

7.5 Future works

A proof of concept is part of a calibration method development. To make it intact as a calibration method, it must be equipped with an estimate of the uncertainty of the calibration results. One of the main components in the calibration process's uncertainty is the standard deviation of repeated measurements. In this study, proof of concept has been complemented by repeated measurement results.

Nevertheless, there are still other sources of uncertainty that have been identified, but the value of their contribution has not been determined in the calibration process. Determining the value of the contribution of sources of uncertainty in the proposed calibration method becomes the future works.

Bibliography

[1] BIPM, "The international vocabulary of metrology—basic and general concepts and associated terms (vim)," JCGM **200**, 2012 (2012).

[2] P. Howarth, F. Redgrave, P. Germany, S. Madsen, and S. Grafisk, "Metrology–in short 3rd edition," EURAMET project **1011** (2008).

[3] J. Terrien, "News from the bureau international des poids et mesures," Metrologia **8**(1), 32–36 (1972).

[4] B. Taylor, "International system of units (si)(rev., 2008 ed.)," NIST special publication. DIANE Publishing Company (2009).

[5] D. T. Martin, *Design, fabrication, and characterization of a MEMS dual-backplate capacitive microphone*, Vol. 69 (2007).

[6] P. R. Scheeper, B. Nordstrand, J. O. Gullv, Bin Liu, T. Clausen, L. Midjord, and T. Storgaard-Larsen, "A new measurement microphone based on mems technology," Journal of Microelectromechanical Systems **12**(6), 880–891 (2003).

[7] G. S. Wood, A. Torin, A. K. Al-mashaal, L. S. Smith, E. Mastropaolo, M. J. Newton, and R. Cheung, "Design and characterization of a micro-fabricated graphene-based mems microphone," IEEE Sensors Journal **19**(17), 7234–7242 (2019).

[8] B. A. Ganji and B. Y. Majlis, "Design and fabrication of a new mems capacitive microphone using a perforated aluminum diaphragm," Sensors and Actuators A: Physical **149**(1), 29–37 (2009).

[9] S. Mallik, D. Chowdhury, and M. Chttopadhyay, "Development and performance analysis of a low-cost mems microphone-based hearing aid with three different audio amplifiers," Innovations in Systems and Software Engineering **15**(1), 17–25 (2019).

[10] K. Taylor, "Absolute measurement of acoustic particle velocity," The Journal of the Acoustical Society of America **59**(3), 691–694 (1976).

[11] H.-E. De Bree *et al.*, "The microflown: An acoustic particle velocity sensor," Acoustics Australia **31**(3), 91–94 (2003).

[12] J. Sharpe and C. Greated, "A stochastic model for photon correlation measurements in sound fields," Journal of Physics D: Applied Physics **22**(10), 1429 (1989).

[13] D. Hann and C. Greated, "Acoustic measurements in flows using photon correlation spectroscopy," Measurement Science and Technology **5**(2), 157 (1994).

[14] J. Sharpe, T. Koukoulas, B. Piper, N. Sungar, and J. Tompkins, "Impact of tracer particle size on optical measurement of sound fields," Applied acoustics **120**, 54–58 (2017).

[15] V. I. Balakshy and J. Hassan, "Polarization effects in acousto-optic interaction," Optical Engineering **32**(4), 746–752 (1993).

[16] K. Nakamura, "Sound field measurement through the acousto-optic effect of air by using laser doppler velocimeter," in *Technical Digest. CLEO/Pacific Rim 2001. 4th Pacific Rim Conference on Lasers and Electro-Optics (Cat. No.01TH8557)* (2001), Vol. 1, pp. I–I.

[17] J. Buick, J. Cosgrove, P.-A. Douissard, C. Greated, and B. Gilabert, "Application of the acousto-optic effect to pressure measurements in ultrasound fields in water using a laser vibrometer," Review of scientific instruments **75**(10), 3203–3207 (2004).

[18] Y. Oikawa, M. Goto, Y. Ikeda, T. Takizawa, and Y. Yamasaki, "Sound field measurements based on reconstruction from laser projections," in *Proceedings.(ICASSP'05). IEEE International Conference on Acoustics, Speech, and Signal Processing, 2005.*, IEEE (2005), Vol. 4, pp. iv–661.

[19] K. Ishikawa, K. Yatabe, Y. Ikeda, Y. Oikawa, T. Onuma, H. Niwa, and M. Yoshii, "Optical sensing of sound fields: Non-contact, quantitative, and single-shot imaging of sound using high-speed polarization camera," in *Proceedings of Meetings on Acoustics 172ASA*, Acoustical Society of America (2016), Vol. 29, p. 030005.

[20] A. Torras-Rosell, S. Barrera-Figueroa, and F. Jacobsen, "Sound field reconstruction using acousto-optic tomography," The Journal of the Acoustical Society of America **131**(5), 3786–3793 (2012).

[21] D. Hermawanto, K. Ishikawa, K. Yatabe, and Y. Oikawa, "Measurement of sound pressure inside tube using optical interferometry," in *INTER-NOISE and NOISE-CON Congress and Conference Proceedings*, Institute of Noise Control Engineering (2018), Vol. 258, pp. 2646–2656.

[22] J. M. Eargle, *Handbook of recording engineering* (Springer Science & Business Media, 2012).

[23] Brüel&Kjær, "Microphone handbook," (1996).

[24] RØDE, "Product data: Nt45-c datasheet," (2020).

[25] IEC, "Iec 61094-1: Measurement microphones - part 1: Specifications for laboratory standard microphones," (2000).

[26] S. Gade, T. Schack, H. Herlufsen, and O. Thorhauge, "Transducer response equalisation," in *Proceedings IMAC XXVI Conference* (2008).

[27] G. E. Moore, "Cramming more components onto integrated circuits," Proceedings of the IEEE **86**(1), 82–85 (1998).

[28] C. Livermore, A. R. Forte, T. Lyszczarz, S. D. Umans, A. A. Ayon, and J. H. Lang, "A high-power mems electric induction motor," Journal of microelectromechanical systems **13**(3), 465–471 (2004).

[29] F. Karpat, S. Ekwaro-Osire, and M. P. Khandaker, "Probabilistic analysis of mems asymmetric gear tooth," Journal of Mechanical Design **130**(4) (2008).

[30] D. Nguyen, E. Halvorsen, G. Jensen, and A. Vogl, "Fabrication and characterization of a wideband mems energy harvester utilizing nonlinear springs," Journal of Micromechanics and Microengineering **20**(12), 125009 (2010).

[31] S. Tadigadapa and K. Mateti, "Piezoelectric MEMS sensors: state-of-the-art and perspectives," Measurement Science and Technology **20**(9), 092001 (2009).

[32] W. R. Ali and M. Prasad, "Piezoelectric mems based acoustic sensors: A review," Sensors and Actuators A: Physical **301**, 111756 (2020).

[33] S. A. Zawawi, A. A. Hamzah, B. Y. Majlis, and F. Mohd-Yasin, "A review of mems capacitive microphones," Micromachines **11**(5), 484 (2020).

[34] G. Nicollini and D. Devecchi, "Mems capacitive microphones: acoustical, electrical, and hidden thermal-related issues," IEEE Sensors Journal **18**(13), 5386–5394 (2018).

[35] Knowles, *MEMS Microphone* (2012).

[36] R. K. Cook, "Absolute pressure calibration of microphones," The Journal of the Acoustical Society of America **12**(3), 415–420 (1941).

[37] J. Rayleigh, "Treatise on sound vol ii," (1878).

[38] S. Ballantine, "Technique of microphone calibration," The Journal of the Acoustical Society of America **3**(3), 319–360 (1932).

[39] G. S. Wong, "Microphones and their calibration," in *Springer Handbook of Acoustics* (Springer, 2014), pp. 1061–1091.

[40] X. Yan, M. J. Crocker, and L. J. Zeng, "Measured capacitance of a condenser microphone as a function of diaphragm displacement," The Journal of the Acoustical Society of America **108**(5), 2134–2144 (2000).

[41] P. Hariharan, *Basics of interferometry* (Elsevier, 2010).

[42] P. Hariharan, "Chapter 21 interferometers," Michael Bass (editor in chief),"Handbook of Optics II","Device, measurements and properties", McGRAW-Hill INC (1995).

[43] S. Rothberg, M. Allen, P. Castellini, D. D. Maio], J. Dirckx, D. Ewins, B. Halkon, P. Muyshondt, N. Paone, T. Ryan, H. Steger, E. Tomasini, S. Vanlanduit, and J. Vignola, "An international review of laser doppler vibrometry: Making light work of vibration measurement," Optics and Lasers in Engineering **99**, 11 – 22 (2017), laser Doppler vibrometry.

[44] P. Castellini, M. Martarelli, and E. Tomasini, "Laser doppler vibrometry: Development of advanced solutions answering to technology's needs," Mechanical Systems and Signal Processing **20**(6), 1265 – 1285 (2006), special Issue: Laser Doppler Vibrometry.

[45] A. Donges and R. Noll, *Laser Measurement Technology* (Springer, 2016).

[46] D. Malacara, *Optical shop testing*, Vol. 59 (John Wiley & Sons, 2007).

[47] P. de Groot, "Phase shifting interferometry," in *Optical measurement of surface topography* (Springer, 2011), pp. 167–186.

[48] R. Tanigawa, K. Yatabe, and Y. Oikawa, "Experimental visualization of aerodynamic sound sources using parallel phase-shifting interferometry," Experiments in Fluids **61**(9), 1–10 (2020).

[49] K. Ishikawa, K. Yatabe, N. Chitanont, Y. Ikeda, Y. Oikawa, T. Onuma, H. Niwa, and M. Yoshii, "High-speed imaging of sound using parallel phase-shifting interferometry," Optics express **24**(12), 12922–12932 (2016).

[50] T. Onuma and Y. Otani, "A development of two-dimensional birefringence distribution measurement system with a sampling rate of 1.3 mhz," Optics communications **315**, 69–73 (2014).

[51] T. Yatagai, B. J. Jackin, A. Ono, K. Kiyohara, M. Noguchi, M. Yoshii, M. Kiyohara, H. Niwa, K. Ikuo, and T. Onuma, "Instantaneous phase-shifting fizeau interferometry with high-speed pixelated phase-mask camera," in *SPECKLE 2015: VI International Conference on Speckle Metrology*, International Society for Optics and Photonics (2015), Vol. 9660, p. 966018.

[52] H. G. Gale, "On the relation between density and index of refraction of air," Physical Review (Series I) **14**(1), 1 (1902).

[53] J. H. Gladstone and T. P. Dale, "Xiv. researches on the refraction, dispersion, and sensitiveness of liquids," Philosophical Transactions of the Royal Society of London (153), 317–343 (1863).

[54] K. Ishikawa, K. Yatabe, Y. Ikeda, and Y. Oikawa, "Numerical analysis of acousto-optic effect caused by audible sound based on geometrical optics," in *12th Western Pacific Acoustics Conference*, Research publishing (2015), pp. 165–169.

[55] C. J. Dasch, "One-dimensional tomography: a comparison of abel, onion-peeling, and filtered backprojection methods," Applied optics **31**(8), 1146–1152 (1992).

[56] A. Katsevich, "Theoretically exact filtered backprojection-type inversion algorithm for spiral ct," SIAM Journal on Applied Mathematics **62**(6), 2012–2026 (2002).

[57] Y. Oikawa, T. Hasegawa, Y. Ouchi, Y. Yamasaki, and Y. Ikeda, "Visualization of sound field and sound source vibration using laser measurement method," Proc. Int. Congr. Acoust.(ICA'10) 898 (2010).

[58] E. Fernandez-Grande, A. Torras-Rosell, and F. Jacobsen, "Holographic reconstruction of sound fields based on the acousto-optic effect," in *INTER-NOISE and NOISE-CON Congress and Conference Proceedings*, Institute of Noise Control Engineering (2013), Vol. 247, pp. 3181–3190.

[59] R. Tanigawa, K. Ishikawa, K. Yatabe, Y. Oikawa, T. Onuma, and H. Niwa, "Extracting sound from flow measured by parallel phase-shifting interferometry using spatio-temporal filter," in *Three-Dimensional Imaging, Visualization, and Display 2019*, International Society for Optics and Photonics (2019), Vol. 10997, p. 109970R.

[60] K. Ishikawa, K. Yatabe, and Y. Oikawa, "Seeing the sound of castanets: Acoustic resonances between shells captured by high-speed optical visualization with 1-mm resolution," The Journal of the Acoustical Society of America **148**(5), 3171–3180 (2020).

[61] A. C. Kak, M. Slaney, and G. Wang, "Principles of computerized tomographic imaging," (2002).

[62] J. Hsieh, *Computed tomography: principles, design, artifacts, and recent advances*, Vol. 114 (SPIE press, 2003).

[63] G. L. Zeng, "Revisit of the ramp filter," in *2014 IEEE Nuclear Science Symposium and Medical Imaging Conference (NSS/MIC)*, IEEE (2014), pp. 1–6.

[64] C. R. Crawford, "Ct filtration aliasing artifacts," IEEE transactions on medical imaging **10**(1), 99–102 (1991).

[65] H. P. Hiriyannaiah, "X-ray computed tomography for medical imaging," IEEE signal Processing magazine **14**(2), 42–59 (1997).

[66] M. E. Phelps, *PET: molecular imaging and its biological applications* (Springer Science & Business Media, 2004).

[67] W. Zhou, J. Weng, J. Peng, and J. Zhong, "A simple distortion calibration method for wide-angle lenses based on fringe-pattern phase analysis," arXiv preprint arXiv:1911.12141 (2019).

[68] T. Regert and P. Planquart, "Cold flow tests for flow field and deformation characteristics of the ptf membrane from the podx," in *6th European Conference for Aeronautics and Space Sciences, EUCASS* (2015).

[69] B. Gallagher, B. Stamper, and R. Youngworth, "An overview of power spectral density (psd) calculations," in *Proc. SPIE* (2005), Vol. 5869, pp. 206–216.

[70] J. Taghia, J. Taghia, N. Mohammadiha, J. Sang, V. Bouse, and R. Martin, "An evaluation of noise power spectral density estimation algorithms in adverse acoustic environments," in *2011 IEEE International Conference on Acoustics, Speech and Signal Processing (ICASSP)*, IEEE (2011), pp. 4640–4643.

[71] H. H. Toebben, G. A. Ringel, F. Kratz, and D.-R. Schmitt, "Use of power spectral density (psd) to specify optical surfaces," in *Specification, Production, and Testing of Optical Components and Systems*, International Society for Optics and Photonics (1996), Vol. 2775, pp. 240–250.

[72] B. E. Saleh and M. C. Teich, *Fundamentals of Photonics* (John Wiley & Sons, 2019).

[73] S. P. Schwartz, *Geometrical and Visual Optics* (McGraw Hill Professional, 2019).

[74] C. B. Duane, "Close-range camera calibration," Photogramm. Eng **37**(8), 855–866 (1971).

[75] A. Nowakowski and W. Skarbek, "Analysis of Brown camera distortion model," in *Photonics Applications in Astronomy, Communications, Industry, and High-Energy Physics Experiments 2013*, edited by R. S. Romaniuk, International Society for Optics and Photonics, SPIE (2013), Vol. 8903, pp. 248–257.

[76] M. V. Berry, "Much ado about nothing: optical distortion lines (phase singularities, zeros, and vortices)," in *International Conference on Singular Optics*, International Society for Optics and Photonics (1998), Vol. 3487, pp. 1–5.

[77] F. W. Sears, *Principles of physics series: Optics* (Addison-Wesley Press, 1947).

[78] M. Yasumura, "Pincushion distortion correction apparatus," (1983), uS Patent 4,409,523.

[79] P. Després, W. C. Barber, T. Funk, M. McClish, K. S. Shah, and B. H. Hasegawa, "Pincushion distortion correction in position-sensitive avalanche photodiodes," in *IEEE Nuclear Science Symposium Conference Record, 2005*, IEEE (2005), Vol. 4, pp. 2031–2034.

[80] K. Gribbon, C. Johnston, and D. G. Bailey, "A real-time fpga implementation of a barrel distortion correction algorithm with bilinear interpolation," in *Image and Vision Computing New Zealand* (2003), pp. 408–413.

[81] H. Haneishi, Y. Yagihashi, and Y. Miyake, "A new method for distortion correction of electronic endoscope images," IEEE Transactions on Medical Imaging **14**(3), 548–555 (1995).

[82] M. Langford, *Langford's basic photography: the guide for serious photographers* (Taylor & Francis, 2010).

[83] "Distortion — edmund optics," (Accessed on 09/01/2020).

[84] G. S. Wong, T. F. Embleton, and S. L. Ehrlich, "Aip handbook of condenser microphones (theory, calibration, and measurements)," ASAJ **98**(1), 20 (1995).

[85] S. Barrera-Figueroa, "Free-field reciprocity calibration of measurement microphones at frequencies up to 150 khz," The Journal of the Acoustical Society of America **144**(4), 2575–2583 (2018).

[86] H. Takahashi and R. Horiuchi, "Uncertainty analysis on free-field reciprocity calibration of measurement microphones for airborne ultrasound," The Journal of the Acoustical Society of America **144**(4), 2584–2597 (2018).

[87] G. S. Wong and L. Wu, "Interchange microphone method for calibration by comparison," in *INTER-NOISE and NOISE-CON Congress and Conference Proceedings*, Institute of Noise Control Engineering (1998), Vol. 1998, pp. 51–54.

[88] F. Su and C. Joslin, "Acoustic imaging using a 64-node microphone array and beamformer system," in *2015 IEEE International Symposium on Signal Processing and Information Technology (ISSPIT)* (2015), pp. 168–173.

[89] C. Vanwynsberghe, R. Marchiano, F. Ollivier, P. Challande, H. Moingeon, and J. Marchal, "Design and implementation of a multi-octave-band audio camera for realtime diagnosis," Applied Acoustics **89**, 281 – 287 (2015).

[90] C. Mydlarz, J. Salamon, and J. P. Bello, "The implementation of low-cost urban acoustic monitoring devices," Applied Acoustics **117**, 207 – 218 (2017).

[91] S. B. Horowitz, M. Sheplak, L. N. Cattafesta, and T. Nishida, "A MEMS acoustic energy harvester," Journal of Micromechanics and Microengineering **16**(9), S174–S181 (2006).

[92] M. Pedersen, "Acoustic performance of mems microphones. past, present, and future," The Journal of the Acoustical Society of America **141**(5), 3676–3676 (2017).

[93] H.-C. Her, T.-L. Wu, and J. H. Huang, "Acoustic analysis and fabrication of microelectromechanical system capacitive microphones," Journal of Applied Physics **104**(8), 084509 (2008).

[94] J. Czarny, "Conception, fabrication et caractérisation d'un microphone mems," Ph.D. thesis, Lyon, INSA, 2015.

[95] R. P. Wagner and S. E. Fick, "Pressure reciprocity calibration of a mems microphone," The Journal of the Acoustical Society of America **142**(3), EL251–EL257 (2017).

[96] A. Prato, N. Montali, C. Guglielmone, and A. Schiavi, "Pressure calibration of a digital microelectromechanical system microphone by comparison," The Journal of the Acoustical Society of America **144**(4), EL297–EL303 (2018).

[97] M. Dobosz, T. Usuda, and T. Kurosawa, "Methods for the calibration of vibration pick-ups by laser interferometry: Ii. experimental verification," Measurement Science and Technology **9**(2), 240 (1998).

[98] J.-G. Suh, W.-H. Cho, H.-Y. Kim, Z. Cui, and Y. Suzuki, "Sensitivity measurement of a laboratory standard microphone by measuring the diaphragm vibration," Applied Acoustics **143**, 38–47 (2019).

[99] K. Taylor, "Absolute calibration of microphones by a laser-doppler technique," The Journal of the Acoustical Society of America **70**(4), 939–945 (1981).

[100] T. Koukoulas, B. Piper, and P. Theobald, "Gated photon correlation spectroscopy for acoustical particle velocity measurements in free-field conditions," The Journal of the Acoustical Society of America **133**(3), EL156–EL161 (2013).

[101] T. Koukoulas and B. Piper, "Towards direct realisation of the si unit of sound pressure in the audible hearing range based on optical free-field acoustic particle measurements," Applied Physics Letters **106**(16), 164101 (2015).

[102] B. Piper, T. Koukoulas, R. Barham, and R. Jackett, "Measuring mems microphone freefield performance using photon correlation spectroscopy," in *The 22nd International Congress on Sound and Vibration* (2015), pp. 12–16.

[103] K. Yatabe, K. Ishikawa, and Y. Oikawa, "Hyper ellipse fitting in subspace method for phase-shifting interferometry: practical implementation with automatic pixel selection," Opt. Express **25**(23), 29401–29416 (2017).

[104] K. Yatabe, K. Ishikawa, and Y. Oikawa, "Simple, flexible, and accurate phase retrieval method for generalized phase-shifting interferometry," J. Opt. Soc. Am. A **34**(1), 87–96 (2017).

[105] A. Patil and P. Rastogi, "Subspace-based method for phase retrieval in interferometry," Opt. Express **13**(4), 1240–1248 (2005).

[106] K. Yatabe, R. Tanigawa, K. Ishikawa, and Y. Oikawa, "Time-directional filtering of wrapped phase for observing transient phenomena with parallel phase-shifting interferometry," Opt. Express **26**(11), 13705–13720 (2018).

[107] P. E. Ciddor, "Refractive index of air: new equations for the visible and near infrared," Applied optics **35**(9), 1566–1573 (1996).

[108] J. Weigold, T. Brosnihan, J. Bergeron, and X. Zhang, "A mems condenser microphone for consumer applications," in *19th IEEE International Conference on Micro Electro Mechanical Systems*, IEEE (2006), pp. 86–89.

[109] L. Liliana, "A new model of ishikawa diagram for quality assessment," in *IOP Conference Series: Materials Science and Engineering*, IOP Publishing (2016), Vol. 161, p. 012099.

[110] M. Coccia, "The fishbone diagram to identify, systematize and analyze the sources of general purpose technologies," Journal of Social and Administrative Sciences **4**(4), 291–303 (2018).

[111] E. Frederiksen, "Acoustic metrology–an overview of calibration methods and their uncertainties," International Journal of Metrology and Quality Engineering **4**(2), 97–107 (2013).

[112] IEC, "Iec 61094-4: Measurement microphones part 4: Specifications for working standard microphones," (1995).

[113] Bruel & Kjaer, *Laboratory Standard Microphone Catridge Types 4160 and 4180* (2019).

[114] P. Juhl, "A numerical investigation of standard condenser microphones," Journal of Sound and Vibration **177**(4), 433 – 446 (1994).

[115] IEC, "Iec 61094-3: Electroacoustics—measurement microphones—part 3: Primary method for free-field calibration of laboratory standard microphones by the reciprocity technique," (2016).

[116] J. W. Strutt, "Vi. on the application of the principle of reciprocity to acoustics," Proceedings of the Royal Society of London **25**(171-178), 118–122 (1877).

[117] F. J. Fahy, "Some applications of the reciprocity principle in experimental vibroacoustics," Acoustical Physics **49**(2), 217–229 (2003).

[118] J. R. Cox, "Physical limitations on free-field microphone calibration," Ph.D. thesis, Massachusetts Institute of Technology, 1954.

[119] R. P. Wagner and V. Nedzelnitsky, "Determination of acoustic center correction values for type ls2ap microphones at normal incidence," The Journal of the Acoustical Society of America **104**(1), 192–203 (1998).

[120] W. J. Trott, "Effective acoustic center redefined," The Journal of the Acoustical Society of America **62**(2), 468–469 (1977).

[121] K. Rasmussen, *Acoustic centre of condenser microphones* (Acoustics Laboratory, Technical University of Denmark, 1973).

[122] F. Jacobsen, S. Barrera Figueroa, and K. Rasmussen, "A note on the concept of acoustic center," The Journal of the Acoustical Society of America **115**(4), 1468–1473 (2004).

[123] D. Rodrigues, J.-N. Durocher, M. Bruneau, and A.-M. Bruneau, "A new method for the determination of the acoustic center of acoustic transducers," Acta Acustica united with Acustica **96**(2), 300–305 (2010).

[124] M. Lindner, "Reader class for photron .mraw-files," (Accessed on 22/07/2020).

[125] V. Nedzelnitsky and R. P. Wagner, "Non-contact methods for measuring front cavity depths of laboratory standard microphones using a depth-measuring microscope," Journal of research of the National Institute of Standards and Technology **113**(2), 97 (2008).

[126] C. C. Putri and D. Hermawanto, "Microphone front cavity depth measurement using non-contact method at national measurement standards-national standardization agency of indonesia," Jurnal Standardisasi **21**(2), 143–148 (2019).

[127] Y. Xu, D. Feng, and L. V. Wang, "Exact frequency-domain reconstruction for thermoacoustic tomography. i. planar geometry," IEEE transactions on medical imaging **21**(7), 823–828 (2002).

[128] M. Brühl and M. Hanke, "Numerical implementation of two noniterative methods for locating inclusions by impedance tomography," Inverse Problems **16**(4), 1029 (2000).

[129] J. Qi and R. M. Leahy, "Iterative reconstruction techniques in emission computed tomography," Physics in Medicine & Biology **51**(15), R541 (2006).

Publications

Journal

○ D. Hermawanto, K. Ishikawa, K. Yatabe, and Y. Oikawa, "Determination of frequency response of mems microphone from sound field measurements using optical phase-shifting interferometry method," Applied Acoustics 170, 107523 (2020).

Proceeding of International Conference

○ D. Hermawanto, K. Ishikawa, K. Yatabe, and Y. Oikawa, "Measurement of sound pressure inside tube using optical interferometry," in INTER-NOISE and NOISE-CON Congress and Conference Proceedings, Institute of Noise Control Engineering, Vol. 258, pp. 2646–2656 (2018).

Proceeding of Domestic Conference

D. Hermawanto, K. Ishikawa, K. Yatabe, and Y. Oikawa, "MEMS microphone sensitivity characterization using parallel phase-shifting interferometry," in 2019 Autumn Meeting Proceedings, Acoustical Society of Japan, pp. 1217–1218 (2019).

D. Hermawanto, K. Ishikawa, K. Yatabe, and Y. Oikawa, "Very near field sound pressure visualization of mems microphone by optical interferometer," in 2017 Autumn Meeting Proceedings, Acoustical Society of Japan, pp. 633–634 (2017).